The Dissertation Committee for Jongwon Lee Certifies that this is the approved version of the following dissertation:

NONLINEAR AND WAVELENGTH-TUNABLE PLASMONIC METASURFACES AND DEVICES

Committee:

Mikhail A. Belkin, Supervisor

Ray T. Chen

Andrea Alù

Zheng Wang

Gennady Shvets

NONLINEAR AND WAVELENGTH-TUNABLE PLASMONIC METASURFACES AND DEVICES

by

Jongwon Lee, B.S.E.E.;M.S.E.

Dissertation

Presented to the Faculty of the Graduate School of

The University of Texas at Austin

in Partial Fulfillment

of the Requirements

for the Degree of

Doctor of Philosophy

The University of Texas at Austin

December, 2014

Dedication

To My Family

Acknowledgements

First of all, I would like to express my gratitude to my advisor Dr. Mikhail A. Belkin for all his support and guidance during over the past five years, leading to the successful completion of this dissertation.

I also would like to thank Dr. Ray T. Chen, Dr. Andrea Alu, Dr. Zheng Wang and Dr. Gennady Shvets for serving on both my qualifying examination committee and my dissertation committee.

Thanks also go to our group members for their helpful discussions and collaborations, in the past and present: Min Jang, Seungyong Jung, Feng Lu, Karun Vijayraghavan, Aiting Jiang, Yifan Jiang, Mingzhou Jin, Jaehyun Kim, and Nishant Nookala.

I would finally like to acknowledge my friends in the Microelectronics Research Center, Beomsuk Lee, Seyoung Kim, Jiwon Chang, Keun Woo Park, Jongho Lee, Youngkyu Lee, Seonpil Jang, Bongjun Kim, Jaehyun Ann, Donghui Koh, Kayoung Lee, Kyunghwan Kim, Kwangsub Byun, Seohee Kim, Sangeun Park, and Junsoak Kim.

Jongwon Lee
University of Texas at Austin
December 2014

Nonlinear and Wavelength-Tunable Plasmonic Metasurfaces and Devices

Jongwon Lee, Ph. D.
The University of Texas at Austin, 2014

Supervisor: Mikhail A. Belkin

Wavelength-tunable optical response from solid-state optoelectronic devices is a desired feature for a variety of applications such as spectroscopy, laser emission tuning, and telecommunications. Nonlinear optical response, on the other hand, has an important role in modern photonic functionalities, including efficient frequency conversions, all-optical signal processing, and ultrafast switching. This study presents the development of optical devices with wavelength tunable or nonlinear optical functionality based on plasmonic effects.

For the first part of this study, widely wavelength tunable optical bandpass filters based on the unique properties of long-range surface plasmon polaritons (LR SPP) are presented. Planar metal stripe waveguides surrounded by two different cladding layers that have dissimilar refractive index dispersions were used to develop a wide wavelength tuning. The concept was demonstrated using a set of index-matching fluids and over 200nm of wavelength tuning was achieved with only 0.004 of index variation. For practical application of the proposed concept, a thermo-optic polymer was used to develop a widely tunable thermo-optic bandpass filter and over 220 nm of wavelength tuning was achieved with only 8 ºC of temperature variation.

Another novel approach to produce a widely wavelength tunable optical response for free-space optical applications involves integrating plasmonic metasurfaces with quantum-electronic engineered semiconductor layers for giant electro-optic effect, which is proposed and experimentally demonstrated in the second part of this study. Coupling of surface plasmon modes formed by plasmonic nanoresonators with Stark tunable intersubband transitions in multi-quantum well structures induced by applying bias voltages through the semiconductor layer was used to develop tunable spectral responses in the mid-infrared range. Experimentally, over 310 nm of spectral peak tuning around 7 μm of wavelength with 10 ns response time was achieved.

As the final part of this study, highly nonlinear metasurfaces based on coupling of electromagnetically engineered plasmonic nanoresonators with quantum-engineered intersubband nonlinearities are proposed and experimentally demonstrated. In the proof-of-concept demonstration, an effective nonlinear susceptibility over 50 nm/V was measured and, after further optimization, over 480 nm/V was measured for second harmonic generation under normal incidence. The proposed concept shows that it is possible to engineer virtually any element of the nonlinear susceptibility tensor of the nonlinear metasurface.

Table of Contents

List of Tables

List of Figures

Chapter 1

Introduction

1.1OVERVIEW

In recent years, we have seen a widespread interest in the fundamental research and development of surface-plasmon-based structures and devices. Surface plasmon polaritons (SPPs) are coherent electron oscillations that are evanescently confined at the interface between metal and dielectric. These electromagnetic surface waves are excited via the coupling of incident electromagnetic fields that induce oscillations of the electron plasma of the metal. They can take various forms, ranging from freely propagating electron density waves along metal surfaces to localized electron oscillations on metal nanoparticles. Their unique properties enable a wide range of practical applications, including light guiding and manipulation at the nanoscale, biodetection at the single molecule level, enhanced optical transmission through subwavelength apertures, and high resolution optical imaging below the diffraction limit [1-5].

Plasmonic metamaterials are metamaterials that exploit surface plasmons. They are tailor made composites – combinations of metallic and dielectric materials designed to achieve optical properties not seen in nature. The properties originate from the unique structure of the composites, with features smaller than the wavelength of light separated by subwavelength distances. In recent years, research in plasmonic metamaterials has yielded unusual electromagnetic properties such as artificial magnetism at optical frequencies, negative index of refraction, and optical cloaking [6-11].

1.2 OUTLINE

This dissertation describes experimental explorations to develop novel optical devices based on unique properties of SPPs and metamaterials. Theoretical background and physical expressions used for developments are discussed in Chapter 2. An initial work on developing widely-wavelength tunable optical bandpass filters is presented in Chapter 3. In this work, unusual properties of planar plasmonic waveguide surrounded by two different cladding layers that have different refractive index dispersions were used to develop devices with a wide wavelength tuning range. The tuning mechanism has been demonstrated by using index matching fluids and thermally tunable devices have been demonstrated by using a thermo-optic polymer. Another novel approach to produce wide wavelength tuning by introducing plasmonic metamaterials integrated with quantum-electronic engineered semiconductor layers is presented in Chapter 4. The coupling of electromagnetic modes in plasmonic nanoresonators and voltage-tunable intersubband transitions in semiconductor heterostructures was used to develop metasurfaces with voltage-tunable spectral responses. This coupling concept can further be applied to generate nonlinear response from metamaterials. A first step to build nonlinear metamaterials based on the combination of electromagnetic engineering of a metamaterial and quantum-electronic engineering of a nonlinear medium is described in Chapter 5. In this work, the metamaterial and the nonlinear medium were designed to generate a second harmonic signal. Finally, a summary is given and several future plans are suggested in Chapter 6.

Chapter 2

Theoretical Background

2.1 LONG-RANGE SURFACE PLASMON POLARITONS

Surface plasmon polariton (SPP) is an electromagnetic surface wave that is guided along the metal-dielectric interface as shown in Fig. 2.1 (a). SPPs are evanescently confined in the metal/dielectric interface and only exist for Transverse Magnetic (TM) polarization. SPP waves can be excited via the coupling of the incident electromagnetic fields to induce oscillations of the electron plasma of the metal. The surface excitations are determined in terms of the SPP dispersion relation given by [12];

$$k_{SPP} = \frac{\omega}{c}\sqrt{\frac{\varepsilon_d \varepsilon_m}{\varepsilon_d + \varepsilon_m}} \,. \qquad (2.1)$$

where, ε_d and ε_m are dielectric constant of dielectric and metal, c is the speed of light, ω is angular frequency. The necessary condition for an SPP to exist can be obtained from Eq. (2.1) to have a positive real part, leading to $\mathrm{Re}\left(\varepsilon_m(\omega)\right) < -\varepsilon_d$. For most metals and dielectrics, this condition is satisfied in the long-wavelength part of the visible and in the infrared. Figure 2.1 (b) shows plots for light and SPP dispersion for an air ($\varepsilon_2 = 1$) anda fused silica ($\varepsilon_2 = 2.25$) interface on a metal using the loss-less Drude model ($\varepsilon_m(\omega) = 1 - (\omega_p / \omega)^2$). One can see that the SPP wavelength approaches zero at the high-frequency limit of the SPP dispersion when $\omega \to \omega_p / \sqrt{1+\varepsilon_d}$. The corresponding limiting frequency of SPPs is the frequency of electrostatic surface waves, called surface plasmons (SPs).

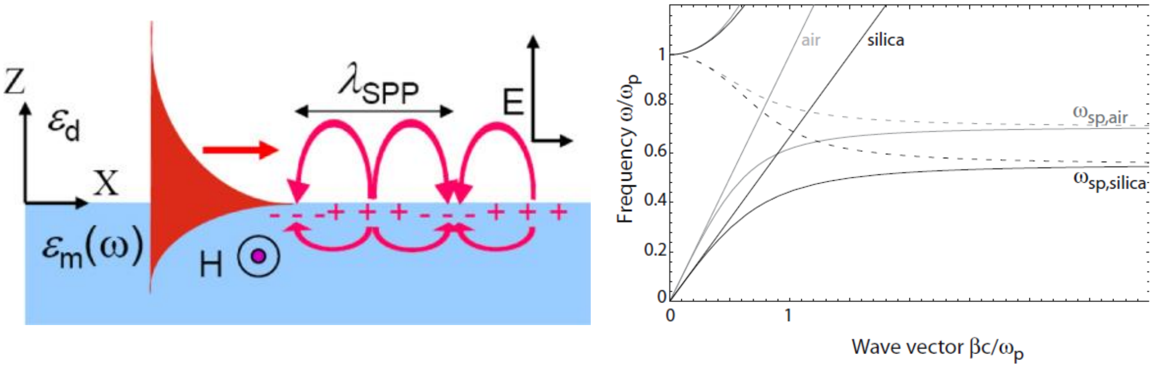

Figure 2.1: (a) Schematic representation of an intensity distribution of the magnetic field (H_y) and electric field (E_z) components of a SPP supported by a metal-dielectric interface. (b) Dispersion relation of SPP at the interface between metal-air and metal-fused silica.

The long-range surface plasmon-polaritons (LR SPP) is a symmetric TM-polarized optical mode that exists in thin metal films embedded in dielectrics with similar refractive indices above and below the metal [13-15]. Physically, LR SPP originates from coupling of the two SPP waves at the metal/top dielectric and metal/bottom dielectric interfaces to form a low-loss symmetric mode [13-15]. The dispersion relation of the coupled SPP waves can be derived by considering a insulator/metal/insulator (IMI) system in which a thin metal layer (I) is sandwiched between two thick dielectric claddings (II, III), (see Fig.2.2). A general description of TM modes that are non-oscillatory in the z-direction normal to interfaces for z > a can be expressed in these forms [12]

$$H_y(z) = Ae^{i\beta x}e^{-k_3 z} \tag{2.2}$$

$$E_x(z) = iA\frac{1}{\omega\varepsilon_0\varepsilon_3}k_3 e^{i\beta x}e^{-k_3 z} \tag{2.3}$$

$$E_z(z) = -A\frac{\beta}{\omega\varepsilon_0\varepsilon_3}e^{i\beta x}e^{-k_3 z} \tag{2.4}$$

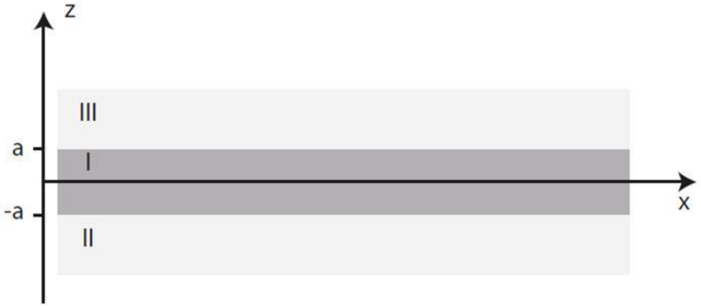

Figure 2.2: Schematic cross section of an insulator/metal/insulator (IMI) structure [12].

while for z < -a we get

$$H_y(z) = Be^{i\beta x}e^{-k_2 z} \tag{2.5}$$

$$E_x(z) = -iB\frac{1}{\omega\varepsilon_0\varepsilon_2}k_2 e^{i\beta x}e^{k_2 z} \tag{2.6}$$

$$E_z(z) = -B\frac{\beta}{\omega\varepsilon_0\varepsilon_2}e^{i\beta x}e^{k_2 z} \tag{2.7}$$

and for –a < z < a

$$H_y(z) = Ce^{i\beta x}e^{k_1 z} + De^{i\beta x}e^{-k_1 z} \tag{2.8}$$

$$E_x(z) = -iC\frac{1}{\omega\varepsilon_0\varepsilon_1}k_1 e^{i\beta x}e^{k_1 z} + iD\frac{1}{\omega\varepsilon_0\varepsilon_1}k_1 e^{i\beta x}e^{-k_1 z} \tag{2.9}$$

$$E_z(z) = C\frac{\beta}{\omega\varepsilon_0\varepsilon_1}e^{i\beta x}e^{k_1 z} + D\frac{\beta}{\omega\varepsilon_0\varepsilon_1}e^{i\beta x}e^{-k_1 z} \tag{2.10}$$

We can get an expression for the dispersion relation linking β and ω by applying continuity boundary conditions ($H_z, E_x, \varepsilon_i E_z$) at $z = \pm a$ and solving this system of linear equations [12].

$$e^{-4k_1 a} = \frac{k_1/\varepsilon_1 + k_2/\varepsilon_2}{k_1/\varepsilon_1 - k_2/\varepsilon_2}\frac{k_1/\varepsilon_1 + k_3/\varepsilon_3}{k_1/\varepsilon_1 - k_3/\varepsilon_3} \tag{2.11}$$

In the case when $\varepsilon_2 = \varepsilon_3$ and thus $k_2 = k_3$, the dispersion relation (2.11) can be split into a pair of equations, namely

$$\tanh k_1 a = -\frac{k_2 \varepsilon_1}{k_1 \varepsilon_2} \qquad (2.12)$$

$$\tanh k_1 a = -\frac{k_1 \varepsilon_2}{k_2 \varepsilon_1} \qquad (2.13)$$

It can be shown that equation (2.12) describes symmetric bound modes for $E_z(z)$ ($E_x(z)$ is odd, $H_y(z)$ and $E_z(z)$ is even functions), while (2.13) describes asymmetric bound modes for $E_z(z)$ ($E_x(z)$ is even, $H_y(z)$ and $E_z(z)$ is odd functions). Symmetric bound modes (s_b) have the interesting property that upon decreasing metal film thickness, the confinement of the coupled SPP to the metal film decreases as the mode evolves into a plane wave supported by the homogeneous dielectric environment. For real, absorptive metals described via a complex $\varepsilon(\omega)$, this implies a drastically increased SPP propagation length [13,14]. This mode is called long-range surface plasmon polaritons (LR SPP). Asymmetric bound modes (a_b) exhibit the opposite behavior their confinement to the metal increases with decreasing metal film thickness, resulting in a reduction in propagation length.

In a symmetric structure with lossless dielectrics, the attenuation and effective index of the s_b mode decrease smoothly as metal thickness is reduced, with its mode fields increasingly expelled from the metal film and penetrating more deeply into the dielectrics. The a_b mode exhibits increasing confinement and penetration into the metal with decreasing metal thickness and, consequently, increasing attenuation. For large metal thickness, the a_b and s_b modes are degenerate with the single-interface SPPs supported by the uncoupled top and bottom metal-dielectric interfaces. The trends are similar in an asymmetric slab except that the s_b mode cuts off below a certain thickness that depends on the permittivities and operating wavelength, and with increasing metal

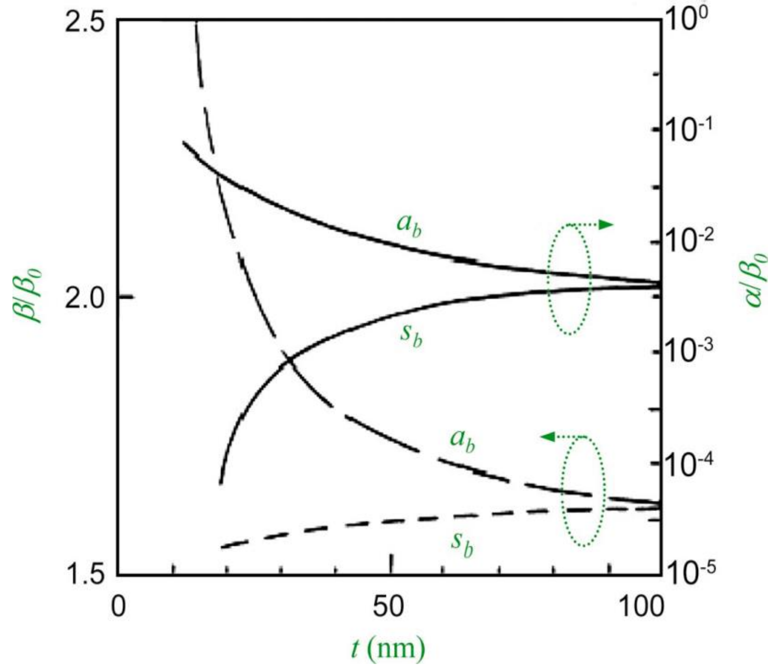

Figure 2.3: Normalized phase and attenuation constant of the odd (anti-symmetric, bound mode, a_b), even (symmetric, bound mode, s_b) modes supported by an asymmetric metal slab at $\lambda_0 = 632.8nm$, assuming Ag for the metal with $\varepsilon_2 = 1.5^2$ and $\varepsilon_3 = 1.55^2$ [16].

thickness, the a_b mode evolves into the SPP supported by the metal interface with the high-index cladding, while the s_b mode evolves into the SPP at the interface with the low-index dielectric.

As an example, Fig. 2.3 shows the effective index (β/β_0) and normalized attenuation (α/β_0) of the a_b and s_b modes in an asymmetric slab at $\lambda_0 = 632.8nm$ assuming Ag for the metal and claddings of relative permittivity $\varepsilon_2 = 1.5^2$ and $\varepsilon_3 = 1.55^2$ [16]. In this figure, α and β are the attenuation and phase constant, respectively. The normalized propagation constant is $\gamma_{eff} = \gamma/\beta_0 = \alpha/\beta_0 + j\beta/\beta_0 = k_{eff} + jn_{eff}$, where $\beta_0 = 2\pi/\lambda_0 = \omega/c_0$ is the phase constant of plane waves in free space, λ_0 the wavelength in free space, and c_0 the speed of light in free space. The complex effective index of a mode N_{eff} is then given by $N_{eff} = -j\gamma_{eff} = n_{eff} - jk_{eff}$, where n_{eff} is the effective index and k_{eff} the normalized attenuation. The mode power attenuation (MPA) in decibels per meter is given by $MPA = \alpha 20\log_{10} e$. The propagation length L_e is the distance from the launch point where the mode power decays by a factor of 1/e and is given by $L_e = 1/(2\alpha)$.

2.2INTERSUBBAND TRANSITIONS IN N-DOPED SEMICONDUCTOR HETEROSTRUCTURE OF III-V MATERIAL SYSTEMS

Intersubband transitions (IST) in n-doped multi-quantum-well semiconductor heterostructures are transitions that occur between electron conduction band states (electron subbands) created by quantum confinement in ultra-thin layers of semiconductor [17,18]. Depending on the relative band offsets of the two semiconductor materials, electrons can be confined in one-direction in the conduction band (for p-doped case, holes are confined in the valence band) and the allowed energy levels are quantized along the growth direction. The energy levels can be tuned by changing the depth and width of the quantum well. In this configuration, optical transitions can take place between electron conduction band states (electron subbands) and the transitions between quantized levels within the conduction band (or valence band) are called ‘intersubband transitions'. Intersubband transitions have unique physical properties, such as quantum-engineered absorption (or emission) wavelengths, atomic-like density of states (i.e. sharp absorption or emission linewidth), and ultrafast carrier dynamics. Owing to well-established III-V semiconductor technology, engineering intersubband transitions has been an

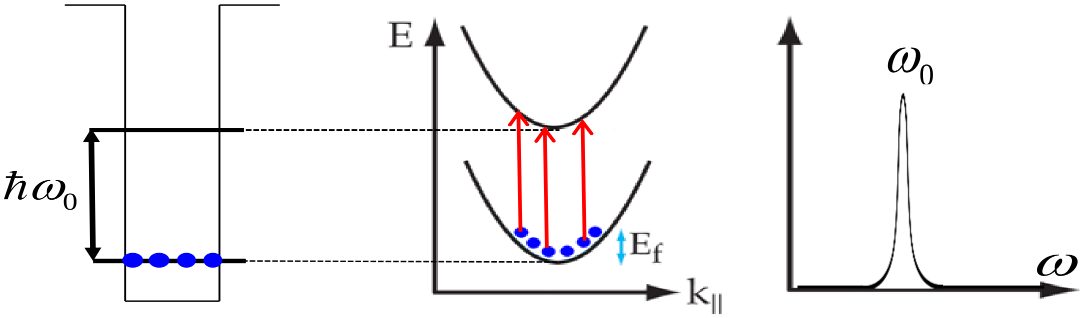

Figure 2.4: Mechanism and properties of intersubband transitions.

attractive building block for mid-infrared and terahertz optoelectronics. So far, modulators, detectors, and lasers have all been demonstrated using technology based on quantum-engineered intersubband transitions, and such devices are becoming mainstream for sensing and telecommunication applications [17,18].

2.2.1 Dielectric Function from Intersubband Transitions

Figure 2.4 shows mechanism and properties of intersubband transitions. In one-dimensional quantum wells composed of a multi-layered semiconductor heterostructure with different band offset, electrons are bound and have quantized energy levels. From the 1D-Schrödinger equation following effective-mass theory, the total energy eigenvalue of the bound electron in quantum well is given as [18]

$$E_n\left(k_{||}\right) = E_n + \frac{\hbar k_{||}^2}{2m_0^*} \tag{2.14}$$

where $k_{||}$ is the in-plane wavevector and m_0^* is taken to be the effective electron mass in the well material and the electron subband energies E_n depend on the shape of $V(z)$. Since the initial and final state have the same in-plane energy dispersion (if one neglects the nonparabolicity, see middle of Fig. 2.4), the joint density of states for the intersubband transition is very sharp and the bound electrons give rise to an atomic-like strong absorption line. This sharp absorption allows for a large change in permittivity in the growth direction, through the Kramers-Kronig relation, for transverse magnetic (TM) polarization, and is given as [18]

$$\varepsilon_{\perp} = \varepsilon_{\infty} - \frac{\varepsilon_{\infty} f_{12} \omega_p^2}{\omega^2 - \omega_{21}^2 + 2i\omega\gamma} \tag{2.15}$$

where γ is the HWHM of the intersubband absorption, τ is a in-plane scattering time, and ω_p is the two-dimensional effective plasma frequency, given by $\omega_p = \sqrt{\left(N_e e^2 / \varepsilon_{\infty}\varepsilon_0 m^*\right)}$. Here f_{12} is the dimensionless oscillator strength between state 1 and 2, given by [18]

$$f_{12} = \frac{2m^* \omega_{21}}{\hbar} \left|\langle 1|z|2\rangle\right|^2 = \frac{2m^* \omega_{21}}{\hbar} z_{12}^2 \tag{2.16}$$

where m^* is effective mass and z_{12} is transition dipole moment. The permittivity of the in-plane component is given as [18]

$$\varepsilon_{\parallel} = \varepsilon_{\infty} - \frac{\varepsilon_{\infty} \omega_p^2}{\omega^2 + i\omega / \tau} . \tag{2.17}$$

For the case when the frequency of the incident beam (ω) is close to the intersubband transition frequency (ω_{21}), an approximation of the denominator of Eq. (2.15) $\left(\omega_{21} - \omega\right)\left(\omega_{21} + \omega\right) \approx 2\omega\left(\omega_{21} - \omega\right)$ can be applied, from which we obtain

$$\varepsilon_{\perp} \approx \varepsilon_{\infty} - \frac{N_e (e z_{12})^2}{\varepsilon_0 \hbar \left(\left(\omega_{12} - \omega\right) - i\gamma_{12}\right)} . \tag{2.18}$$

2.2.2 Nonlinear Susceptibility from Intersubband Transitions

In the case of conventional linear optics, the induced polarization depends on the strength of E-field given as

$$\vec{P}(t) = \varepsilon_0 \chi^{(1)} \vec{E}(t)\,. \tag{2.19}$$

where the constant of proportionality $\chi^{(1)}$ is known as the linear susceptibility and ε_0 is the permittivity of free space. In reality, $\vec{P}$, of course, does not need to be linearly proportional to the external E-field, and the induced polarization can be described by generalizing Eq. (2.19) by expressing the polarization $\vec{P}$ as a power series in the field strength $\vec{E}(t)$ as [19]

$$\begin{aligned} \vec{P} &= \varepsilon_0 \left[\vec{\chi}^{(1)} \vec{E} + \vec{\chi}^{(2)} : \vec{E}\vec{E} + \vec{\chi}^{(3)} : \vec{E}\vec{E}\vec{E} + \cdots \right] \\ &= \vec{P}^{(1)} + \vec{P}^{(2)} + \vec{P}^{(3)} + \cdots. \end{aligned} \tag{2.20}$$

where $\vec{\chi}^{(2)}$ and $\vec{\chi}^{(3)}$ are known as the second- and third-order nonlinear optical susceptibilities, respectively. The linear susceptibility $\vec{\chi}^{(1)}$ is a second-rank tensor (a 3×3 matrix) and each element of the linear polarization is given as $P_i^{(1)} = \varepsilon_0 \chi_{ij}^{(1)} E_j$. Similarly, the second-order nonlinear susceptibility $\vec{\chi}^{(2)}$ is a third-rank tensor (a 3×3×3 matrix) and each element of the linear polarization is given as $P_i^{(2)} = \varepsilon_0 \chi_{ijk}^{(2)} E_j E_k$, etc.

It is known since the late 1980s that n-doped coupled MQWs may be designed to have second-order nonlinear susceptibilities up to 4-5 orders of magnitude larger and third-order nonlinear susceptibilities up to 6-7 orders of magnitude larger than in traditional bulk nonlinear materials [20]. These properties were demonstrated for a variety of nonlinear optical processes, including second harmonic generation (SHG) [21-24], optical rectification [25], sum-[26] and difference-frequency generation (SFG and DFG) [27], Raman amplification [28,29], optical phase conjugation [30], two-photon absorption [31], and other four-wave mixing process [32-34]. The basic design approach is based on tailoring the composition and widths of wells and barriers in MQW structures to engineer electron subbands so as to maximize the quantum mechanical expressions for $\chi^{(2)}$ or $\chi^{(3)}$ for a particular nonlinear process by tailoring transition dipole moments and energy level positions. Optical transitions between electron subbands in MQWs are intrinsically polarized along the surface normal to the MQW layers (z-axis). As a result, giant nonlinear response only exists for input E-fields polarized normal to MQW layers in which the $\chi^{(2)}_{zzz}$ and $\chi^{(3)}_{zzzz}$ terms are giant.

In a resonant three-level system, the full quantum mechanical expressions for the second and third order nonlinear susceptibility terms are simplified when the pump frequencies are close to intersubband resonances and the resonant term is dominant. For SHG, we obtain [18]

$$\chi^{(2)}_{zzz}(\omega \to 2\omega) \approx N_e \frac{e^3}{\hbar^2 \varepsilon_0} \frac{z_{12} z_{23} z_{31}}{(\omega_{31} - 2\omega - i\gamma_{31})(\omega_{21} - \omega - i\gamma_{21})} \tag{2.21}$$

where ω is the pump frequency, e is the electron charge, N_e is the average bulk doping density, $\hbar\omega_{ij}$, $\hbar\gamma_{ij}$, and ez_{ij} are the energy, linewidth, and dipole moment, respectively, for a transition between states i and j. For DFG case, we obtain [18,27]

$$\chi^{(2)}_{zzz}(\omega_1 - \omega_2 \to \omega_{DFG}) \approx N_e \frac{e^3}{\hbar^2 \varepsilon_0} \frac{z_{12} z_{23} z_{31}}{(\omega_{23} - \omega_{DFG} - i\gamma_{32})} \left(\frac{1}{(\omega_{31} - \omega_1 - i\gamma_{31})} + \frac{1}{(\omega_{21} - \omega_2 - i\gamma_{21})} \right) \tag{2.22}$$

For phase conjugation using resonant two-level system, we obtain [17,32]

$$\chi^{(3)}_{zzzz}(\omega + \omega - \omega \to \omega) \approx N_e \frac{e^4}{4\hbar^3 \varepsilon_0} \frac{(z_{12})^4}{(-i\gamma_{22})(\omega - \omega_{21} - i\gamma_{21})} \left(\frac{1}{(-\omega - \omega_{12} + i\gamma_{12})} + \frac{1}{(\omega - \omega_{21} + i\gamma_{21})} \right). \tag{2.23}$$

Chapter 3

Widely Tunable Optical Bandpass Filters Based on Long-Range Surface Plasmon Polaritons[1,2]

3.1 INTRODUCTION

Wavelength-tunable filters are important components of many photonic devices such as tunable semiconductor laser systems, multi-spectral imagers, and other plasmonic components with tunable optical response. The operating principle of compact monolithic photonic filters, such as Mach-Zehnder interferometers, Bragg reflectors, microresonator filters, and distributed feedback lasers, relies on light reflection and interference phenomena [35,36]. The tuning range ($\delta\lambda$) of compact monolithic filters depends on a change in the dielectric constant of the filters medium, and as a result, the tuning range is severely limited by the value of possible variation of the refractive index of filter medium according to the equation

$$\delta\lambda/\lambda=\delta n/n \tag{3.1}$$

where λ is the filter operation wavelength, n is the refractive index of the filter medium, and δn is its possible variation. Since the relative refractive index variation in transparent dielectrics is limited to ≤1% for thermo-optic and electro-optic materials and ≤15% for liquid crystals, the tuning range of these devices is limited. Optical systems with broader tuning ranges are required for many applications, in particular for various spectroscopic and imaging systems. As a result, a number of approaches to produce optical elements with widely tunable response have been developed using mechanical and

---

[1] J. Lee *et al.*, Broadly wavelength tunable bandpass filters based on long-range surface plasmon polaritons. *Opt. Lett.*, **36**, 3744-3746, (2011).

[2] J. Lee *et al.*, Widely tunable thermo-optic plasmonic bandpass filters. *Appl. Phys. Lett.*, **103**, 181115, (2013).

micromechanical elements [36,37], acousto-optic modulation [38], and employing coupled cavities or multisection filters [39-41]. However, these devices are complex and are difficult to miniaturize. In this work, we propose and experimentally demonstrate a new kind of broadly-tunable optical filters based on unique properties of long-range surface plasmon-polaritons (LR SPP). This filter may be used to produce simple monolithic optical components in which a given variation of the refractive index of the dielectric filter medium may be translated into any desired filter tuning range. The filters are extremely simple in fabrication and have no moving parts. The tuning mechanism reported in this work may be used to create monolithic bandpass filters with tuning ranges spanning over more than an optical octave, compact and widely tunable diode and quantum cascade laser systems, multi-spectral imagers, and other plasmonic components with broadly tunable optical response.

The LR SPP is a special kind of TM-polarized plasmon modes that can exist in thin metal films (10-30nm) embedded in dielectrics with similar refractive indices above and below the metal film [13,14,41,42]. Physically, LR SPPs are associated with coupling of two surface plasmon polaritons (SPP) at the upper and lower interfaces between metal and dielectric. LR SPP waveguides may have optical losses of only a few dB/cm at λ=1.55μm [43] and even lower at longer wavelength due to improved optical properties of metals. We note that a LR SPP mode is the only mode supported by this waveguide structure. LR SPP modes are well-confined and well-matched with optical modes in fibers, leading to very low insertion loss of LR SPP waveguides in fiber-optic systems [13,14,43-48]. The optical losses in LR SPP waveguides will increase dramatically, however, if the refractive indices of the materials above and below the metal film are even slightly mismatched [44,46-49].

Our filter is based on integration of a thin metal film between two dielectrics with dissimilar refractive index dispersion. In this configuration, the LR SPP waveguide only have low insertion loss at a wavelength for which the refractive indices of the top (n_t) and bottom (n_b) dielectrics are the same, leading to a bandpass filter.

3.2 SIMULATIONS AND CALCULATIONS OF LR SPP MODE

Mode profile of LR SPP is very sensitive to the indices of the surrounding dielectric layers. Figure 3.1 shows LR SPP waveguide cross-sectional structure used for device simulations. The waveguide structure consists of a thin metal stripe and top and bottom dielectric layers with refractive indices n_t and n_b, respectively. In order to simulate the mode profiles of LR SPP excited in the thin metal stripe, a commercial finite-element package (COMSOL 3.5a and 4.3) was used. In the COMSOL program, the structure was modeled using 2-dimensional RF module with Hybrid-Mode Waves calculator and PEC and PMC boundary conditions were properly defined for TM-polarized field excitation. In this simulation, 4μm-wide and 20nm-thick gold stripe and n_b=1.5 and n_t=1.5+δn at λ=1.55μm wavelength were used. 20μm-thick top and bottom dielectric layers (total 40μm-thick) were defined. Proper refractive index data of gold at λ=1.55μm ($n = 0.55 + 11.5i$) was obtained from Ref. [50].

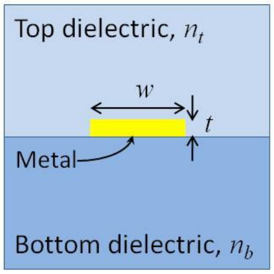

Figure 3.1: Cross-sectional view of LR SPP waveguide structure. The metal stripe is positioned between top and bottom dielectric layers with refractive indices n_t and n_b, respectively.

Figure 3.2 shows the calculated intensity profile of a LR SPP mode at λ=1.55μm supported by a 20nm-thick and 4μm-wide gold stripe embedded between loss-less dielectrics with identical refractive indices and with slightly mismatched refractive indices. For the case when the two indices of dielectric layers are matched, the LR SPP mode is well-confined and well-matched to modes in optical fibers and ridge waveguides. However, as soon as the refractive indices of the dielectric layers are even slightly mismatched (here $\delta n = 0.0014$), the LR SPP mode becomes severely distorted spreading out to the side of dielectric with higher refractive index (see Fig. 3.2 (c) and (d)). And when the refractive indices are mismatched further, then the LR SPP mode bounded to the gold stripe ceases to exist and the LR SPP mode becomes leaky, i.e. radiation mode [13,44,46-49,51]. In this case, the LR SPP mode is not well matched to optical fiber and ridge waveguide mode and as a result, the coupling loss to an optical fiber mode becomes high.

Beyond the cutoff, the LR SPP mode is no longer purely bound but becomes leaky, radiating into the higher-index dielectric as it propagates. It is therefore important to know where the cutoff and the onset of leaky mode occur if index asymmetry is expected. Finding the cutoff points involves varying the index of one of the dielectrics until the effective index becomes approximately equal to the larger of the indices of the dielectrics. It is particularly important for the structure to be modeled as open since the mode expands as it tends towards the cutoff, eventually infinitely extending into one of the dielectrics at the cutoff.

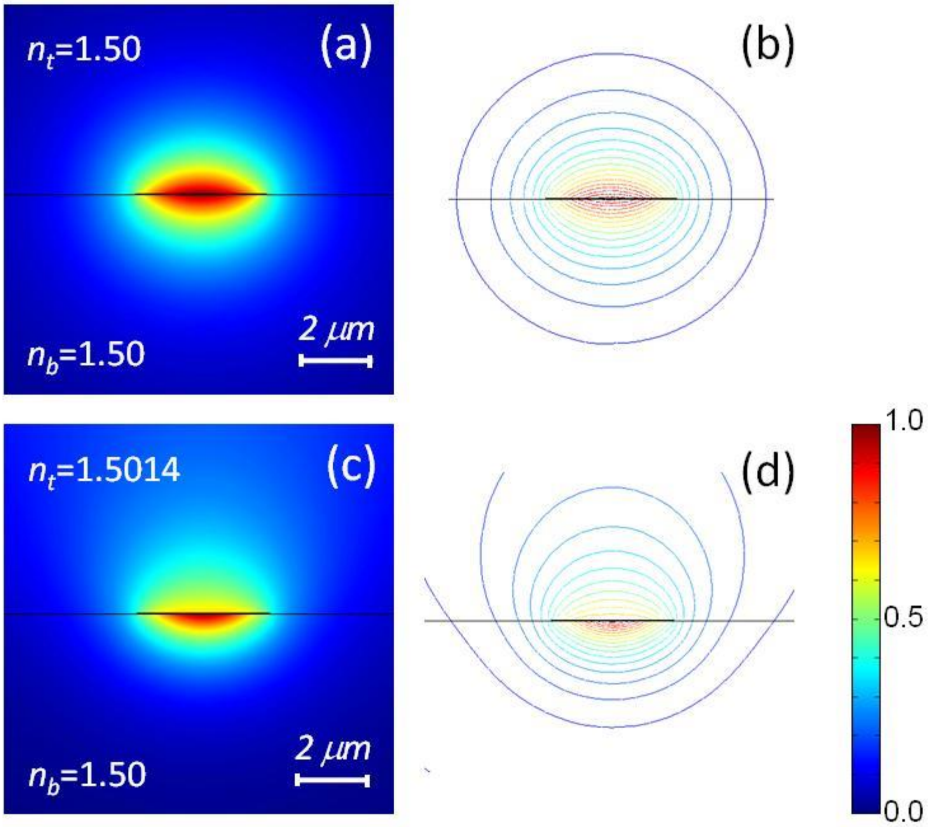

Figure 3.2: (a, b) Simulated intensity profile of a LR SPP mode at λ=1.55μm supported by a 20nm-thick and 4μm-wide gold stripe embedded between loss-less dielectrics with identical refractive indices. (c, d) Calculated LR SPP mode profile of the same structure with slightly mismatched n_t and n_b.

The top panel of Fig. 3.3 shows the mode power attenuation (MPA) and cutoff curves of the LR SPP mode at $\lambda = 1.55\mu m$ for straight waveguides having various Au stripes. The curves were computed as a function of refractive index mismatch (δn). In this calculation, three different dimensions of Au stripes were used: 4μm-wide and 20nm-thick, 3μm-wide and 20nm-thick, and 3μm-wide and 18nm-thick. The bottom panel of Fig. 3.3 shows effective index (n_{eff}) of LR SPP mode as a function of δn for LR SPP waveguides with different values of width (*W*) and thickness (*t*) of the metal stripe. Dashed lines in the figure show the value of the largest of the two cladding indices, n_t or

n_b. The LR SPP mode becomes leaky when n_{eff} is smaller than the largest of n_t or n_b. We assumed λ=1.55µm, $n_b=1.5$, and $n_t=1.5+\delta n$ for the calculations. It is of note that the cutoff occurs for an effective index that is slightly smaller than the larger of the cladding indices rather than for values that are exactly equal. This is due to the small attenuation constant of the mode engendered by the loss in the metal.

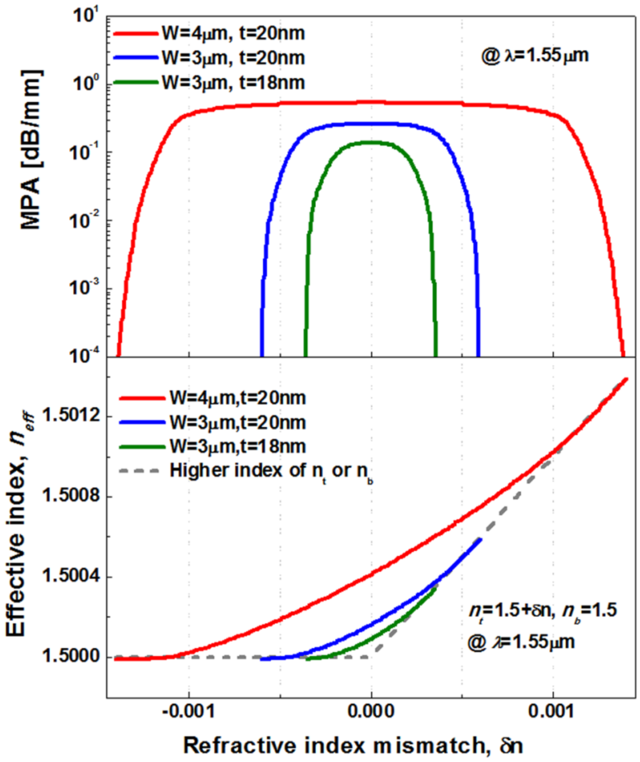

Figure 3.3: Top panel: calculation of the mode power attenuation (MPA, solid line) as a function of $\delta n=n_t-n_b$ for a LR SPP waveguides with different width (W) and thickness (t) of the gold stripe. Bottom panel: effective refractive index (n_{eff}) of LR SPP mode for as a function δn for LR SPP waveguides with different values of W and t (green, blue, and red solid lines). Dashed lines in the figure show the value of the largest of the two cladding indices, n_t or n_b. LR SPP mode becomes leaky when n_{eff} is smaller than the largest of n_t or n_b. We assumed λ=1.55µm, $n_b=1.5$, and $n_t=1.5+\delta n$ for the calculations [49].

On the other hand, LR SPP mode coupling to an input fiber mode or to an output fiber mode is another critical factor to a total insertion loss (overall loss from input source to output detector) calculation. In the calculation of the coupling loss, an overlap factor C for two modes of different shape and size butt-coupled to each other is given by [16]

$$C = \frac{\iint_{A_\infty} E_{y_1} E_{y_2}^* \, dA}{\left(\iint_{A_\infty} E_{y_1} E_{y_1}^* \, dA \right) \left(\iint_{A_\infty} E_{y_2} E_{y_2}^* \, dA \right)} . \qquad (3.2)$$

The integral above is taken over the entire computational domain A_∞ at the transverse plane where the modes meet and are evaluated numerically. The E_y field component of the respective modes is used since it dominates in the LR SPP mode for the waveguide geometries considered herein ($W >> t$).

The coupling efficiency is given by $|C|^2$ in the case where there is no material discontinuity and is usually expressed as a percentage. The coupling loss expressed in decibels is then given by [16]

$$CL_{dB} = -20 \log_{10} |C| . \qquad (3.3)$$

Figure 3.4 shows calculated coupling loss between the LR SPP mode of Au stripe with single-mode optical fibers (SMF-28) at λ=1.55µm. In this calculation, three different geometries of Au stripes, which are the same as in the previous section, were used. As indicated in Fig. 3.4, the coupling loss between the single-mode fiber and LR SPP mode increases sharply as the refractive index mismatch increases. Further, metal stripes with smaller dimensions become more sensitive to the surrounding dielectrics' refractive index mismatch.

Total insertion loss can be calculated by including a propagation loss (MPA times length of the device) and coupling loss at the input and output facets. Figure 3.5 shows the total insertion loss from input fiber to output fiber, which includes the propagation loss for 5mm long device and the input and output facet mode coupling losses. We note from this figure that the total insertion loss also increases sharply as the refractive index mismatch increases, and that coupling loss dominates the total insertion loss from the input fiber to output fiber. Thus, this characteristic of LR SPP mode that is extremely sensitive to refractive index mismatch may be used to build a widely tunable bandpass filter when integrated with dielectrics with dissimilar refractive index wavelength dispersion as the top and bottom cladding.

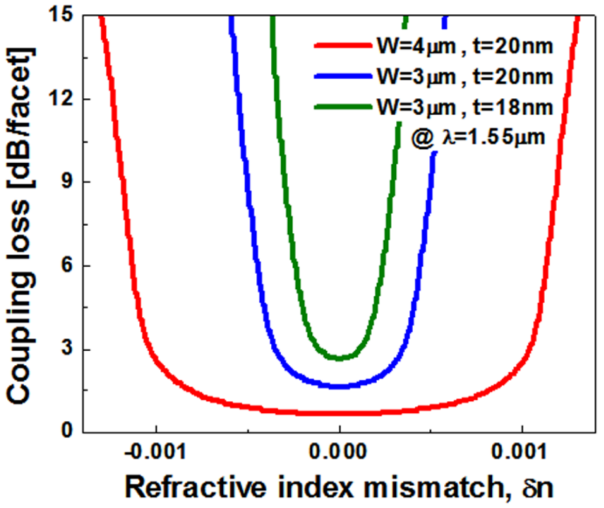

Figure 3.4: Calculation of the coupling loss (per facet) as a function of $\delta n=n_t-n_b$ for a LR SPP waveguides with different width (W) and thickness (t) of the gold stripe [49].

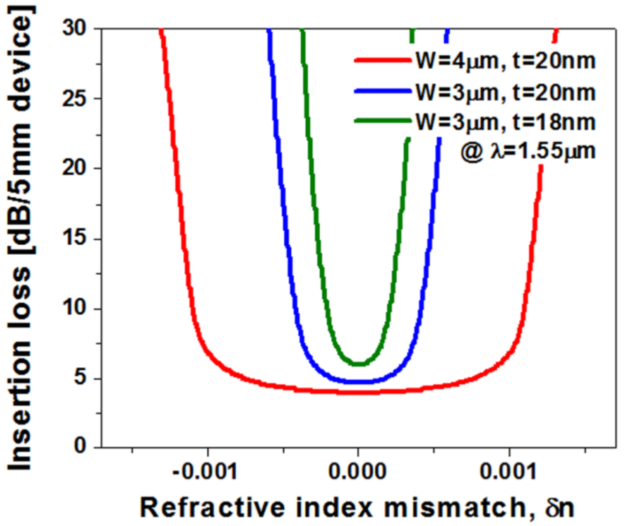

Figure 3.5: Calculation of the insertion loss including a propagation loss (MPA times length of the Au stripe) and coupling loss for the input and output facet as a function of $\delta n=n_t-n_b$ for a LR SPP waveguides with different width (W) and thickness (t) of the gold stripe [49].

3.3 OPERATION PRINCIPLE OF BANDPASS FILTERS BASED ON LR SPP

As shown in Fig. 3.5, the insertion loss is extremely sensitive to δn. To build a widely wavelength-tunable bandpass filter out of a LR SPP waveguide, we propose to use dielectrics with *dissimilar* refractive index wavelength dispersion as the top and bottom cladding dielectric layers. In this configuration, the maximum transmission will be given when the refractive indices of the top and bottom dielectrics are matched, and as δn increases, the transmission will drop due to the increase of the total insertion loss. Effectively, this device will work as a bandpass filter. An schematic of the filter operation is shown in Fig. 3.6. Due to the extreme sensitivity of LR SPP loss to δn, the LR SPP mode is only supported at wavelength λ for which $n_t(\lambda)\approx n_b(\lambda)$. A small change in the refractive index of the top dielectric (δn_t) may now be translated into the large shift in the LR SPP filter bandpass ($\delta\lambda$) according to the equation [49,52]:

$$\delta\lambda = \frac{\delta n_t}{\left(\frac{dn_t}{d\lambda} - \frac{dn_b}{d\lambda}\right)} , \qquad (3.4)$$

where $dn_t/d\lambda$ and $dn_b/d\lambda$ are the refractive index dispersion of n_t and n_b. Since the value of $(dn_t/d\lambda - dn_b/d\lambda)$ may be controlled by a proper choice of materials (or a combination of materials for composite cladding layers), we can control the tuning range of the filter ($\delta\lambda$) for a given value of δn_t. The bandpass width of the LR SPP filter is determined by the sensitivity of the coupling/propagation loss in the LR SPP waveguides to $\delta n=n_t-n_b$, (see Fig. 3.4 and 3.5) and the difference in the refractive index dispersions of the top and bottom dielectrics (see Fig. 3.6).

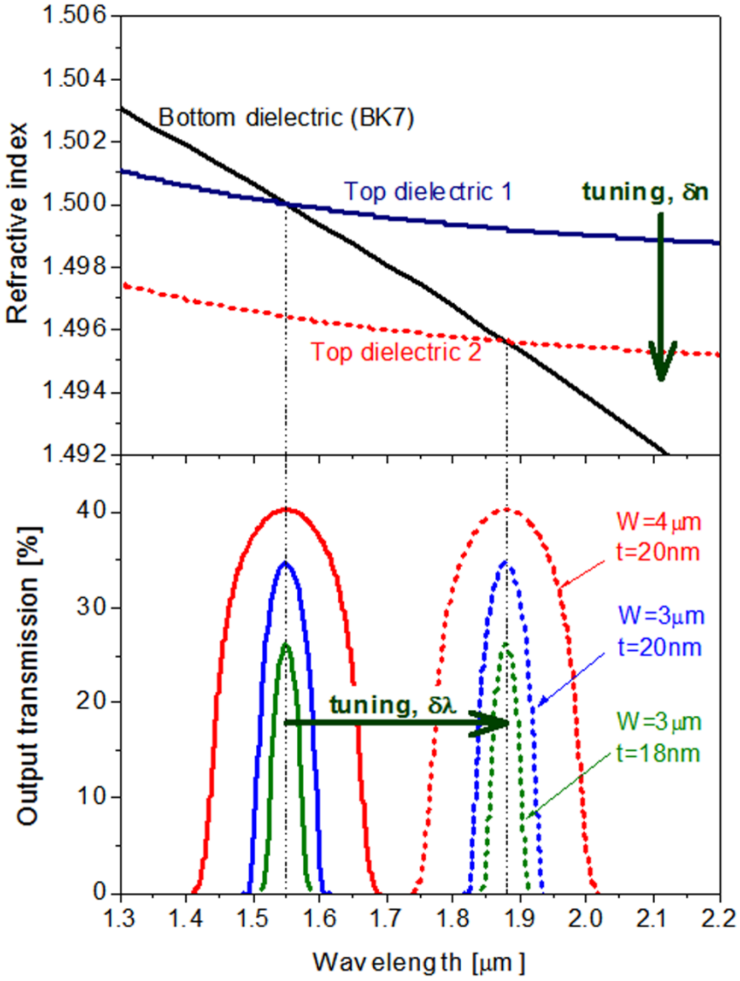

Figure 3.6: Schematic of the LR SPP filter operation. Top panel: refractive index dispersion curves of the bottom dielectric (black line; assumed to be BK7 glass) and the refractive-index-tunable top dielectric (blue solid line and red dashed line). Bottom panel: calculated optical throughput of the single-mode fiber system with 5-mm-long LR SPP filter inserted. Calculations are done for LR SPP filters with different values of *W* and *t*. Filter transmission is calculated for the two refractive index dispersion curves of the top dielectric (blue line and red dashed line in the top panel). Filter transmission is maximal at the index matching point of the top and bottom dielectrics and drops rapidly as wavelength goes away from the matching point [49].

3.4 EXPERIMENT

3.4.1 Proof-of-Principle Demonstration with Index-Matching Fluids

To demonstrate the proposed bandpass filtering and wavelength-tuning mechanism experimentally, we operated at near-infrared wavelengths (λ=1.2-1.8μm) and used a set of five refractive-index-matching fluids (Cargille Labs, Series A and AA) as the top dielectric and thermally grown 11μm-thick SiO_2 layer as the bottom dielectric.

The device was fabricated on an 11-μm-thick layer of thermally-grown SiO_2 on a silicon substrate (Silicon Quest Inc.). For making patterns, a standard image reversal process with AZ5214E photoresist (PR) was used. First, AZ5214E PR was coated on the substrate with 4000rpm for 1 minute, and then the sample was placed on a hot plate at 90 ^0C for 5 minutes. Then, mask patterns were exposed on the sample for 3seconds (light intensity~7mW/cm^2) using a MJB4 mask aligner, and the sample was placed on the hot plate at 115 ^0C for 90 seconds and subsequently exposed for flood exposure (for 100 seconds) to make a reversed pattern image. Next, the sample was developed in AZ726 MIF developer for 1 minute, and a 20nm-thick gold layer was coated using an e-beam evaporator (CHA1) with less than 0.5Å/sec deposition rate, followed by lift off in acetone gently (see Fig.3.7). Finally, the sample was cleaved to 3~5mm-long waveguide sections. A schematic image of the finished device and end-fire coupling method with input and output fiber is illustrated in Fig. 3.8.

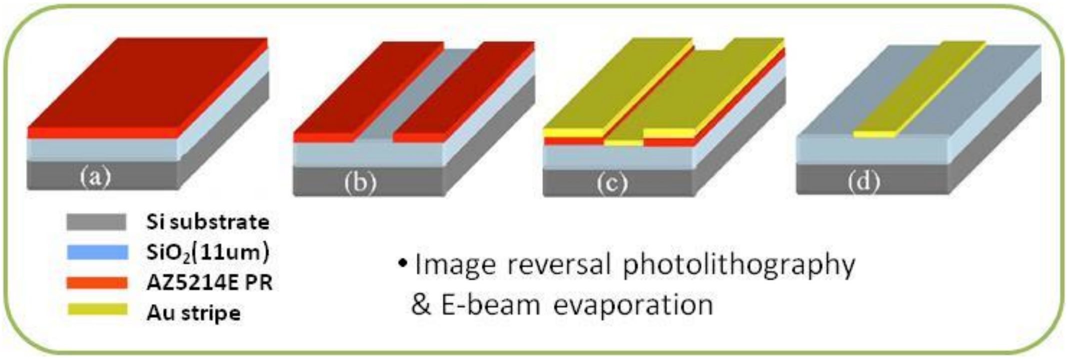

Figure 3.7: Device fabrication steps. (a) AZ5214E photoresist was coated on the substrate. (b) Pattern was made by using standard image reversal process. (c) E-beam evaporation of 20nm-thick gold and (d) lift-off was done subsequently.

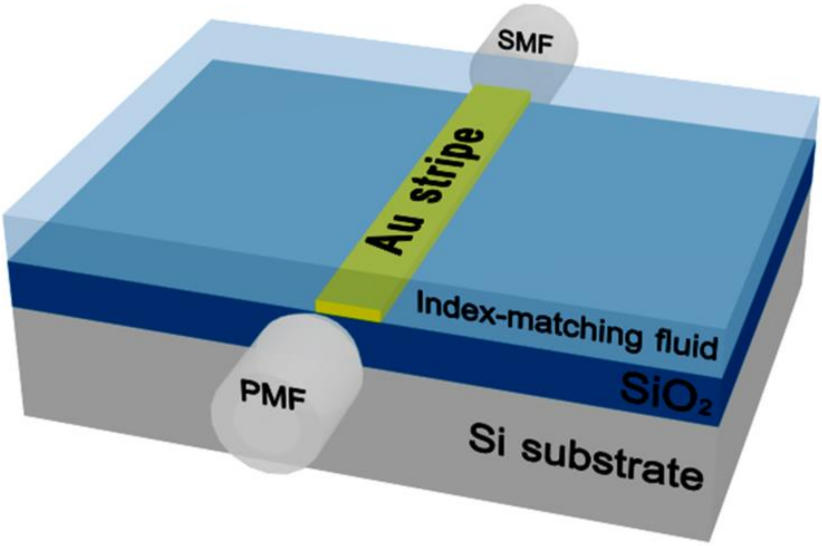

Figure 3.8: The LR SPP waveguide structure and the experimental configuration. The waveguide was made of 4-µm-wide and 20-nm-thick stripe of gold on top of an 11-µm-thick layer of thermally-grown SiO_2 on a silicon substrate. Five types of the refractive index matching fluids were used at the top dielectric. The TM-polarized input light source coupled to a polarization-maintaining fiber (PMF) was end-fire coupled to the LR SPP waveguide; the output light was collected via single mode fiber (SMF) [49].

For the experimental demonstration of LR SPP optical filter, the sample was mounted and covered by refractive index matching fluids (Cargille Labs Mod. Series A and AA). A tunable laser (Santec Mod. MLS-2000, λ=1482nm-1592nm) and a broadband supercontinuum source (Koheras Mod. SuperK versa, λ=400nm-2000nm) coupled to a polarization-maintaining (PM) fiber (Oz optics Mod. PMJ-3S3S-1550-8/125-3-1-1) were used to excite the LR SPP mode via end-fire coupling of light. The output light was collected by single-mode fiber (Corning Mod. SMF-28) coupled to an optical power meter (Newport Mod. 1830-C) or optical spectrum analyzer (Ando Mod. AQ6317B). Both fibers were mounted on three-axis auto-alignment system. The positions of the input and output fiber were adjusted to maximize the transmitted output power. The transmitted broadband output power was recorded and properly normalized with the input power.

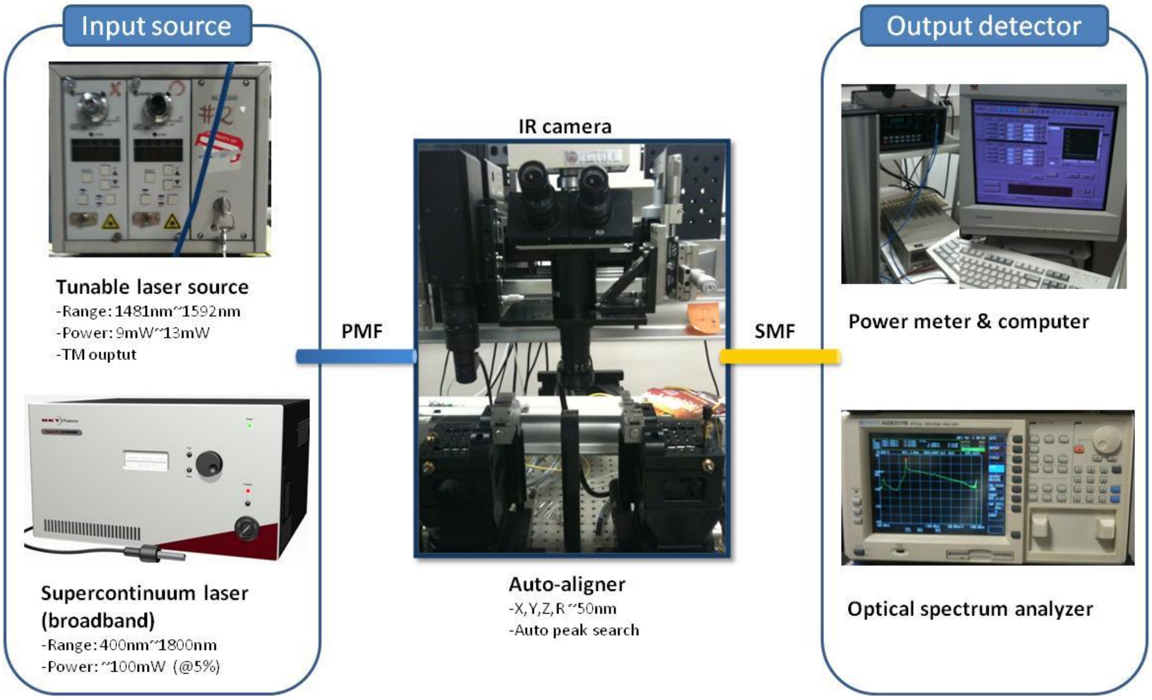

Figure 3.9: Experimental setup for the proof-of-principle demonstration.

The refractive index dispersion curves for SiO_2 and 5 different refractive-index-matching fluids are shown in Fig. 3.10 (a). There are five refractive index matching points with SiO_2, thus we can expect that five different transmission curves corresponding to each refractive index matching points. Fig. 3.10 (b) shows simulated and experimental power transmission spectra through the 3.1-mm-long LR SPP filter. Simulated transmission spectra were calculated using the refractive index dispersion data in Fig. 3.10 (a) and assuming the LR SPP mode is coupled and out-coupled to a single-mode optical fiber (SMF-28). As expected, the filter peak transmission occurs at wavelengths for which $n_t(\lambda)= n_b(\lambda)$; the experimental data of the transmission bandwidth is in good agreement with the theoretical curves. However, the experimental output transmission maximum values of each peak are lower than the calculated output due to possible defects on the Au stripe and the quality of the cutting edge . Experimentally, a 0.004 variation in the refractive index of the cladding dielectric translates into 210 nm of bandpass tuning at telecom wavelengths.

Figure 3.11 (a-f) show measured horizontal and vertical mode profiles in the LR SPP waveguide for different width of Au stripes using different wavelengths of light. In this experiment, type 5 refractive index matching fluid was used as the top cladding dielectric and a diode laser tunable in the range 1482-1592 nm was used as the light source in the end-fire geometry. As expected, the vertical profiles of the LR SPP mode become more distorted as the light wavelength moves away from the spectral point at which $n_t=n_b$, as expected from the simulations (see Fig. 3.2). At the same time, the horizontal LR SPP mode profiles become slightly broader, maintaining their symmetric shape. And as also expected, Au stripes with larger widths are less sensitive to change of refractive index of the index matching fluid (top dielectric).

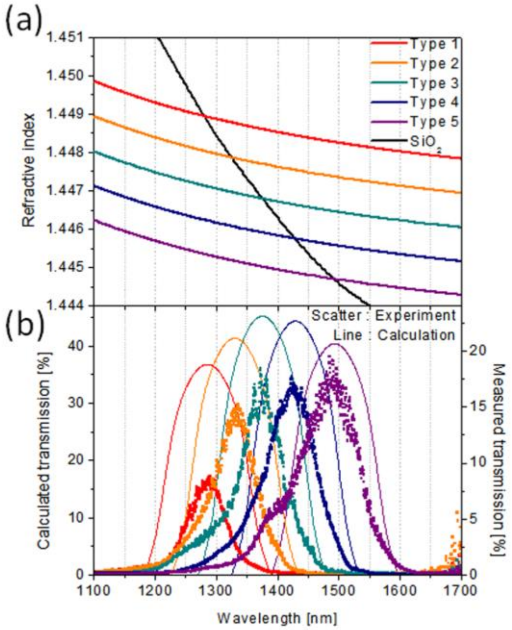

Figure 3.10: Experimental demonstration of the LR SPP optical filter. (a) Refractive index dispersion curves for SiO_2 (black line) and five different refractive index matching fluids (type 1-5) used in experiments. (b) Calculation and experimental results of the filter transmission for the five different types of index matching fluids. A 0.004 variation in the refractive index of the top filter dielectric translates into 210 nm of bandpass tuning range [49].

To make practical solid-state filters, one can use thermo-optic materials, electro-optic crystals, or liquid crystal films as the dielectric with tunable refractive index. The bandpass width of the filters may be controlled by changing the design parameters of the LR SPP waveguides to make them more or less sensitive to δn, see Fig. 3.6. We note that the cutoff point in LR SPP waveguides may be set at an arbitrarily small value of δn by reducing the width and/or thickness of the gold stripe [53]. The bandpass may be narrowed (at the expense of tuning range) by choosing top and bottom dielectric cladding materials with a larger difference in refractive index dispersions, see Eq. (3.4). We note LR SPP filters are expected to operate equally well in mid-infrared spectral range (λ=3-15μm), which is very important of chemical sensing and spectroscopy.

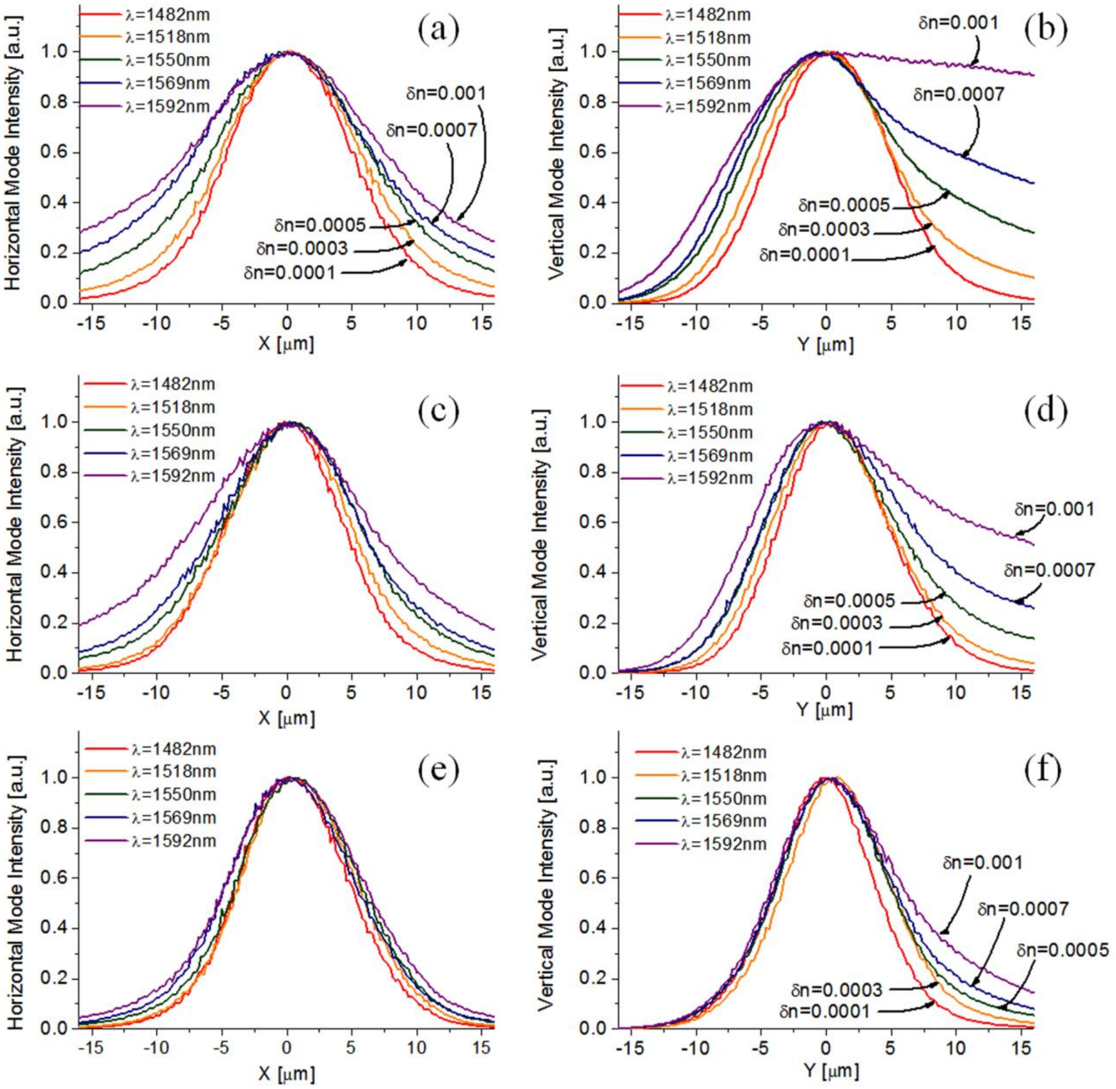

Figure 3.11: Experimental measurement of the horizontal and vertical mode profiles in the LR SPP filter with type 5 refractive index matching fluid at different wavelengths. (a) Horizontal mode profile for 4μm-wide and 20nm-thick Au stripe. (b) Vertical mode profile for 4μm-wide and 20nm-thick Au stripe. (c) Horizontal mode profile for 5μm-wide and 20nm-thick Au stripe. (d) Vertical mode profile for 5μm-wide and 20nm-thick Au stripe. (e) Horizontal mode profile for 6μm-wide and 20nm-thick Au stripe. (f) Vertical mode profile for 6μm-wide and 20nm-thick Au stripe. LR SPP mode becomes distorted as light wavelength (λ) moves away from the spectral point at which $n_t=n_b$; the values of $\delta n=n_t(\lambda)-n_b(\lambda)$ are specified in the figures for each λ.

3.4.2 Thermally Tunable Filters with Thermo-Optic Polymer

A new concept of device based on LR SPP waveguide to create compact and widely-wavelength tunable filters has been successfully demonstrated by using a set of index-matching fluids as top dielectrics [49]. This approach however is not suitable for integration into compact optical systems.

In this work, we demonstrate a thermally-tunable solid-state LR SPP filter that uses a thermo-optic polymer as top dielectric layer. The filter design is based on integration of a thin metal film between two dielectrics with dissimilar refractive index dispersion and dissimilar thermo-optic coefficient. In this configuration, the LR SPP waveguide will only have low insertion loss at a wavelength for which the refractive indices of the top (n_t) and bottom (n_b) dielectrics are the same, leading to a bandpass filter. The filter operation and calculated losses are shown in Fig. 3.12 (a) and (b). The tuning range ($\delta\lambda$) of such a filter is given as $\delta\lambda=\delta n_t/(dn_t/d\lambda-dn_b/d\lambda)$, where $dn_t/d\lambda$ and $dn_b/d\lambda$ are the refractive index dispersions of the top and bottom dielectrics, respectively, and δn_t is the refractive index variation in the top dielectric 49. These solid-state filters are extremely simple to fabricate, have no moving parts, and can provide continuous tuning over potentially more than one optical octave using small variation of the refractive index of the filter medium.

The structure of the LR SPP filter and its cross-section used in our experiments is depicted in Fig. 3.12 (a) and (b). The device is fabricated on a Si wafer with a 15µm-thick layer of thermally-grown SiO_2. The metal stripe is made of gold and is 20nm-thick and 2.7µm-wide. A 34um-thick layer of UV curable thermo-optic polymer (ZPU-1446) as a top dielectric cladding is spin-coated and then cured in an UV light irradiation chamber for 10min. End-fire coupling/out-coupling was used to connect the LR SPP filter to a light source and detector as seen in Fig. 3.12 (b). A broadband source (λ=400-

2000nm) coupled to a single-mode fiber (SMF-28e) were used as a light source. The output light was collected by a SMF and sent to an optical spectrum analyzer. Both input and output fibers were mounted on three-axis auto-alignment system. A 4mm-long LR SPP filter was used in our experiments and the filter was mounted on a temperature-controllable thermo-electric plate.

Top panel of Fig. 3.14 shows the refractive index dispersion curves for SiO_2 ($dn_b/dT=1\times10^{-5}$) at the two different temperatures and ZPU polymer($dn_t/dT=-1.864\times10^{-4}$) at the five different temperatures. The ZPU polymer has a much larger thermo-optic coefficient than SiO_2 and changes its refractive index with temperature significantly, while the refractive index of SiO_2 stays virtually constant. For each temperature, the refractive index dispersion curve of the ZPU polymer intersects that of SiO_2 at a different wavelength.

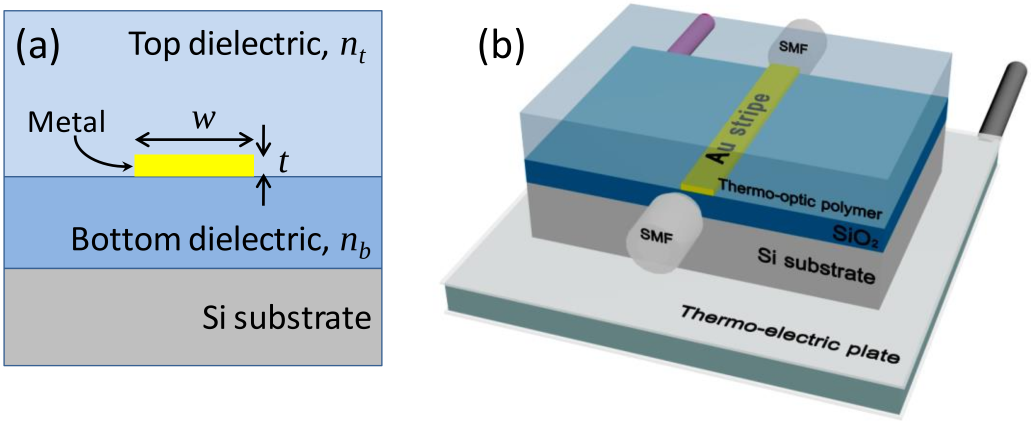

Figure 3.12: (a) Cross section of the LR SPP waveguide used for simulation and experiment. The thin metal stripe is positioned between the top and bottom dielectric layer with its refractive index n_t and n_b. (b) The LR SPP waveguide structure and the experimental configuration [52].

The filter transmission is maximal at wavelengths for which the indices of the top and bottom dielectrics are perfectly matched and drops as off away from the matching point. The calculation and experimental results are presented in the bottom panel of Fig. 3.14. A temperature variation of 8°C translates into a wavelength tuning range of $\delta\lambda \approx 222$nm ($\lambda$=1428~1650nm) with a 28nm/°C of temperature sensitivity. Transmission

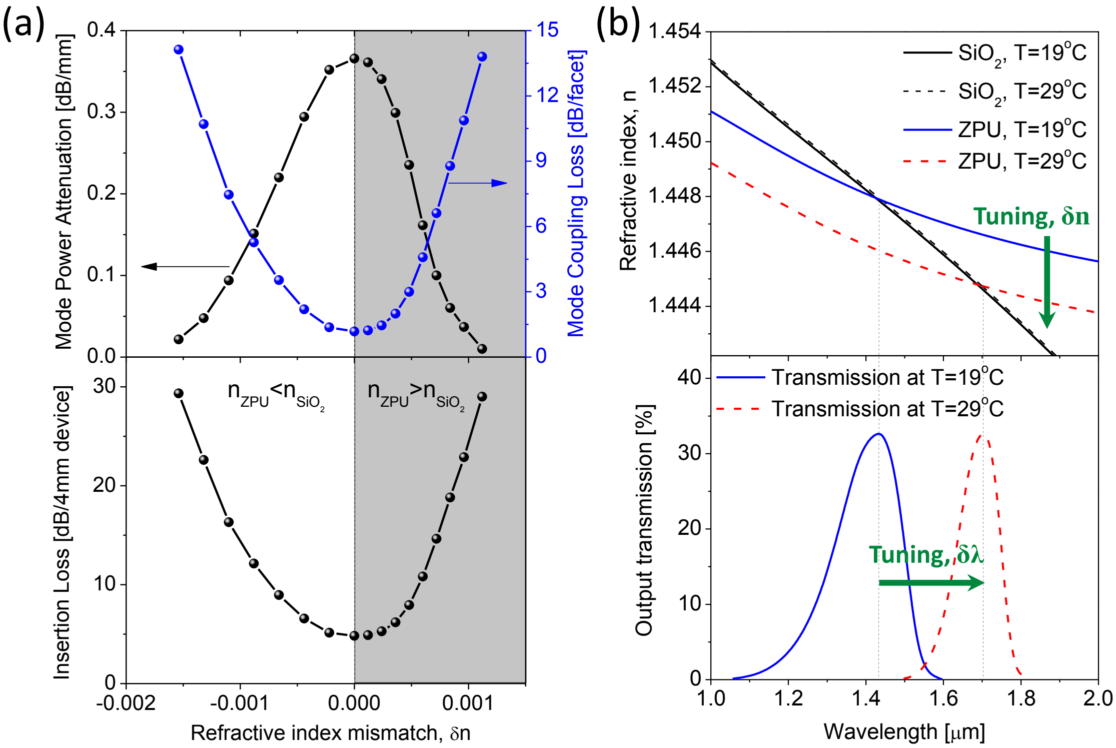

Figure 3.13: (a) Schematic of the LR SPP filter operation. Top: refractive index dispersion curves for SiO_2 and ZPU polymer at 19 °C and 29 °C. Bottom: calculated optical throughput of the 4mm-long LR SPP filter. (b) Calculated mode power attenuation and coupling loss (Top panel) and total insertion loss (Bottom panel) [52].

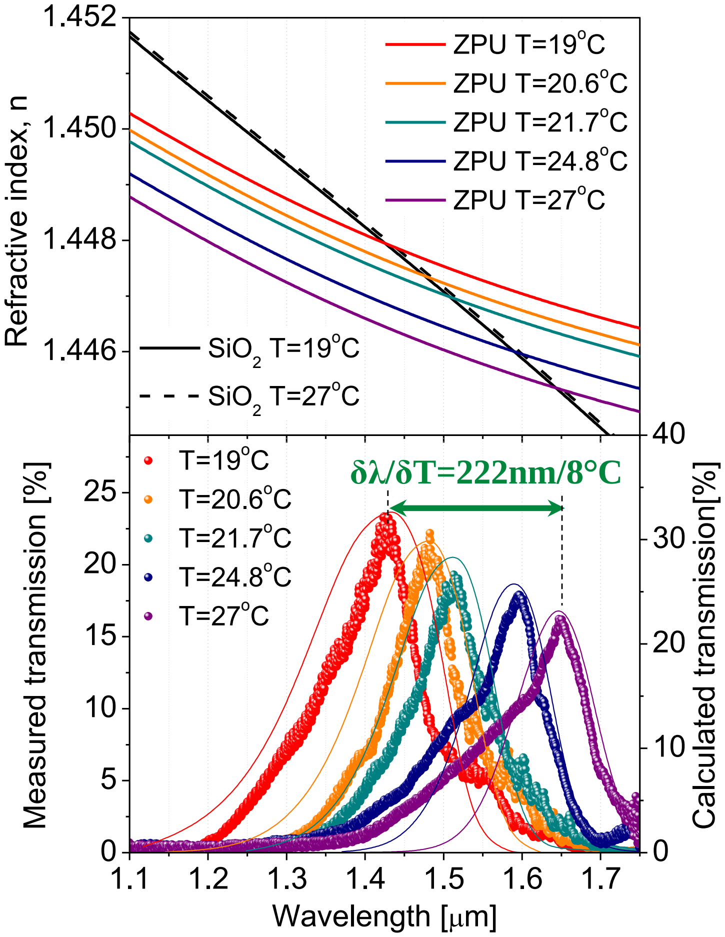

Figure 3.14: Top: refractive index dispersion curves for SiO2 and ZPU polymer at the five different temperatures. Bottom: calculation and experimental results of the filter transmission for the five different temperatures [52].

bandwidth can be reduced by using dielectrics with higher mismatch in optical dispersion, $dn_t/d\lambda - dn_b/d\lambda$ (in this case bandwidth is reduced at the expense of filter tuning range), using longer LR SPP waveguides or stacking multiple LR SPP filters, and by tweaking the filter design to make LR SPP mode more sensitive to the refractive index mismatch between the top and bottom dielectrics.

3.6 CONCLUSION

In this work, we have demonstrated a new kind of widely wavelength-tunable bandpass filter based on LR SPP. The proposed concept was successfully demonstrated using a set of index-matching fluids. In this proof-of-principle demonstration, we achieved over 200nm wavelength tuning with only 0.004 of index variation of the top dielectric layer. To demonstrate a more practical solid-state device, we created a thermally-tunable optical bandpass filter with tuning range of $\delta\lambda \approx 222$nm around 1550nm wavelength based on LR SPP waveguide that uses a thermo-optic polymer as the top dielectric. The filter design allows one to translate a small refractive index tuning range of the top dielectric into a large filter bandpass tuning range. The filters are simple in fabrication and may be integrated with fiber-optic and semiconductor laser systems to create optical components with widely tunable spectral response. The broad tuning range of these devices is appealing, in particular, for tunable laser systems, spectroscopic applications, and imaging.

Chapter 4

Ultrafast Electrically Tunable Polaritonic Metasurfaces[3]

4.1 INTRODUCTION

Plasmonic metasurfaces have recently raised widespread interest due to their ability to control the optical response over a broad spectral range and at deeply sub-wavelength scales by properly tailoring size and shape of metallic nanoinclusions. Frequency selective surfaces [54-56] may be considered the predecessors of metasurfaces, consisting of uniform arrays of inclusions with size on the order of the wavelength, and are capable of tailoring the spectral response to a large degree. Introducing plasmonic materials allows drastic squeezing of the dimensions of each inclusion and confining light in sub-diffractive volumes, with advantages in terms of spatial resolution and enhanced light control. Recently, the concept of gradient metasurfaces has also emerged, in which metallic nanoinclusions are individually tailored to scatter light with the desired phase and amplitude spatial profile. Gradient metasurfaces provide a much richer control of the wavefront in both local amplitude and phase of the emerging transmitted and reflected beams [57-60]. Such structures enable flat optical components for beam focusing, polarization control and phase correction, to name a few examples [57-62].

The next challenge and exciting perspective for this technology consists in enabling real-time reconfigurability of the metasurface platform with a fast response time, which may produce flat optical components for rapid wavefront modulation, phase tuning and beam steering [60]. A number of methods to tune the spectral response of

---

[3] J. Lee *et al.*, Ultrafast Electrically Tunable Polaritonic Metasurfaces. *Adv. Opt. Matt.*, DOI:10.1002/adom.201400185, (2014).

plasmonic nanoresonators have been reported in the recent past, based on thermal, mechanical, optical, and electrical control, as summarized in Ref. [63]. Electrical tuning techniques are of particular interest, since they open a route to on-chip integration of metasurfaces with electronics, potentially enabling GHz-level switching speeds. The most common electrical tuning mechanisms reported so far are based on phase-change media [64-66], the use of liquid crystals [67,68], and carrier concentration control on a semiconductor substrate [69,70] or grapheme [71-74]. Approaches based on phase-change media and liquid crystals rely on intrinsically slow physical processes and thus cannot produce metasurfaces with nanosecond switching time. Carrier-concentration control produces metasurfaces with much faster switching speeds with the best results in terms of tuning range and switching speeds achieved with hybrid metal−graphene structures, demonstrating spectral tuning with switching speeds up to 30 MHz [75], limited by the RC time constant of the biasing circuit.

It has recently been suggested and experimentally demonstrated by our team [76,77] as well as by Brener's group in Sandia Labs [78-80] that metasurfaces made of plasmonic nanoresonators polaritonically-coupled [81-84] to intersubband transitions in multi-quantum-well (MQW) semiconductor heterostructures engineered for large quantum confined Stark effect [85-87] may display voltage-tunable optical response. Here we demonstrate that these polaritonic metasurfaces may provide one of the fastest electrical switching of optical response demonstrated in metasurfaces to date. Our structures utilize well-established InGaAs/AlInAs MQW semiconductor technology and demonstrate comparable absorption modulation speed compared to hybrid metal−graphene structures while using lower bias modulation voltage [75]. Potential applications of these devices may span across multiple disciplines, including actively controllable fast optical switches, beam steering devices, and ultrafast spatial optical modulators.

In the context of modulation speed, we note that the speed of devices based on carrier-concentration modulation is ultimately limited by the carrier injection/removal time (although the time scales of these processes are in the picosecond range, much smaller than the RC time constants of devices demonstrated to date). In contrast, similar to other modulators based on classical electro-optic effect [88], the time response of our devices is limited only by the RC time constant of the biasing circuit which may ultimately offer an advantage for achieving very high modulation speeds.

4.2 METASURFACE DESIGN AND SIMULATIONS

Quantum engineering of intersubband transitions in n-doped MQW heterostructures provides the possibility to produce optical materials with one of the largest known electro-optic coefficients for TM-polarized light, associated with the quantum confined Stark effect [85-87]. For optical frequencies ω close to the intersubband transition frequency, the dielectric constant for E-field polarization perpendicular to the heterostructure layers can be written as [89]

$$\varepsilon_{\perp}(\omega) \approx \varepsilon_{core}(\omega) + \frac{N_e (e z_{12})^2}{\varepsilon_0 \hbar \left((\omega_{12} - \omega) - i\gamma_{12} \right)} \tag{4.1}$$

where $\varepsilon_{core}(\omega)$ is the dielectric constant of an undoped semiconductor structure, *e* is the electron charge, N_e is the average bulk doping density in the MQW structure, and z_{12}, ω_{12}, and γ_{12} are the transition dipole moment, frequency, and linewidth broadening factor, respectively, for a transition between electron states 1 and 2, see Fig. 4.1 (a,b).

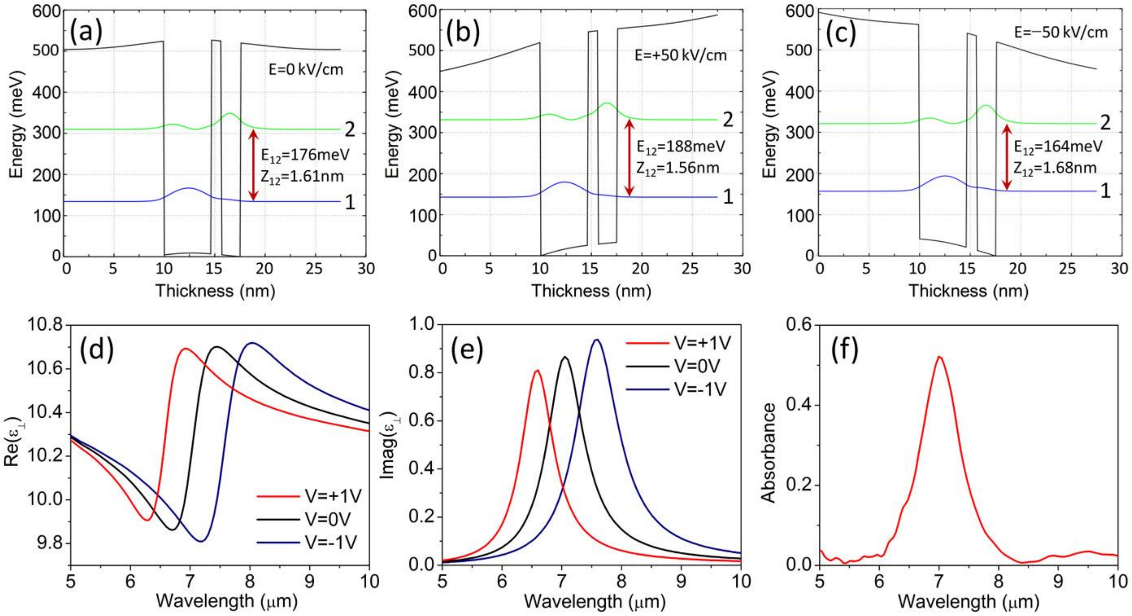

Figure 4.1: Semiconductor heterostructure design. (a-c) Conduction band diagram of one period of an $In_{0.53}Ga_{0.47}As/Al_{0.52}In_{0.48}As$ coupled MQW structure under zero, +50 kV/cm (+1 V across 200 nm), and −50 kV/cm (-1 V across 200 nm) bias fields. Shown in (a-c) are calculated transition dipole moment z_{12} and transition energy E_{12} between the first two electron subbands. (d, e) Calculated real (d) and imaginary (e) parts of the dielectric constant normal to MQW layers $\varepsilon_{\perp}(\omega)$ under applied bias voltages of 0 and +/-1V. (f) Measured absorption spectrum of the MQW structure for zero bias at room temperature [90].

MQW structures can be designed to display giant quantum confined Stark effect by tailoring the wavefunctions for states 1 and 2 to be spatially separated (see Figure 4.1 (a) as an example)[85-87]. In this case, the transition energy ω_{12} can be tuned by bias voltage applied across the structure and this leads to a change in $\varepsilon_{\perp}(\omega)$, cf. Equation 4.1. Owing to intrinsic TM-polarization of intersubband transitions between electron states, the value of the dielectric constant for electric field parallel to the MQW layers, $\varepsilon_{//}(\omega)$, stays unchanged. Our structure is designed using a self-consistent Poisson-Schrodinger solver. It is composed of 7 repetitions of a double-quantum-well unit that consist of 4.7 nm and 1.9 nm $In_{53}Ga_{47}As$ quantum wells, separated by a 1 nm thick $Al_{48}In_{52}As$ barrier. The units are separated with 20 nm thick $Al_{48}In_{52}As$ barriers, doped to 3.44×10^{17} cm^{-3} in the central 14 nm portion. Compared to Ref. 80, much thicker barriers between adjacent coupled-quantum-well units used in our structures resulted in over 2 orders of magnitude reduction of leakage current density (20 A/cm^2 vs 2600 A/cm^2 in Ref. 80) under operational bias voltage which dramatically reduces ohmic heating in our structures. Figure 4.1 (a-e) shows the bandstructure as well as calculated real and imaginary parts of $\varepsilon_\perp$ for the MQW structure used in this work for bias voltages of 0 and +/- 1V applied across approximately 200-nm-thick MQW layer. The calculations assume doping density $N_e=3.44\times10^{17}$ cm^{-3} and transition linewidth $2\hbar\gamma_{12}\approx19\,meV$ obtained from measured intersubband absorption in the MQW structure at zero bias shown in Fig. 4.1 (f). We note that the absorption peak at $\hbar\omega_{12}\approx177\,meV$ in Fig. 4.1 (f) is in excellent agreement with the theoretical calculations shown in Fig. 4.1 (a).

The MQW layer is then sandwiched between a bottom metal ground plane and a top metal layer patterned with an array of complementary nanocrosses. The unit cell of the metasurface is shown in Fig. 4.2 (a). The bottom ground plane is implemented to ensure that the plasmonic nanoresonators support TM-polarized modes in the MQW layer, and it may, at the same time, be used as bottom electrode for electrical biasing of the MQW structure. The complimentary cross design for the top surface pattern is chosen to produce a continuous top metal electrode for biasing.

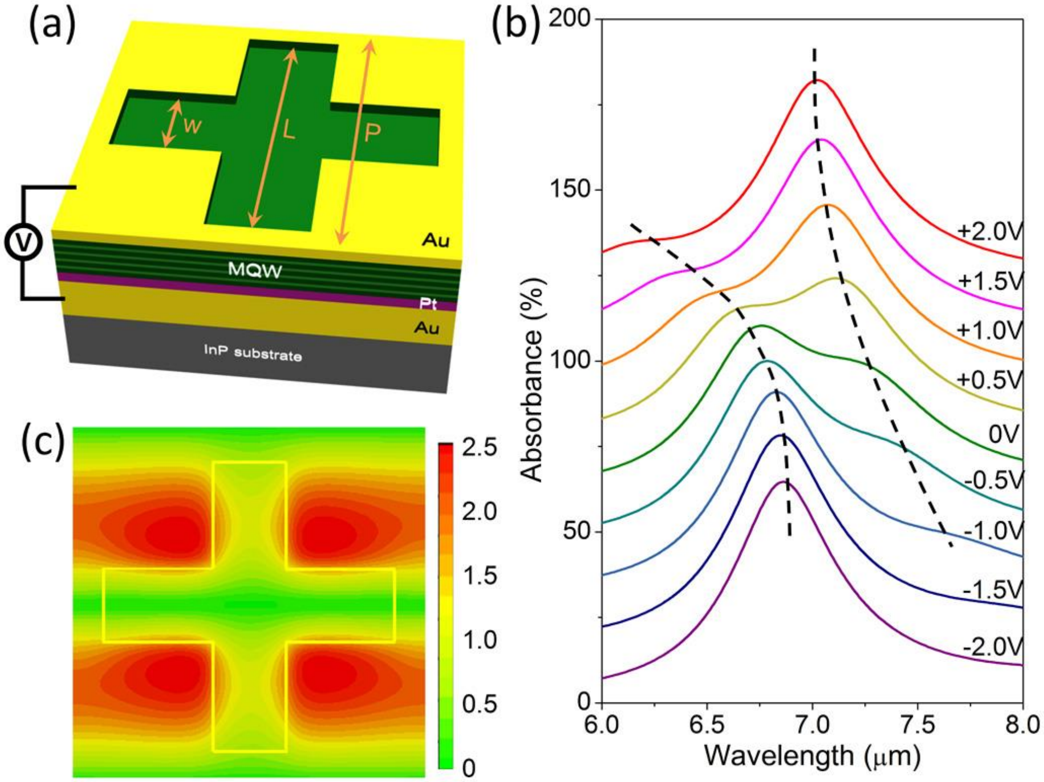

Figure 4.2: Metasurface design. (a) One unit cell of the periodic metasurface (w=0.38 μm, L=1.48 μm, P=1.73 μm). The semiconductor layer is sandwiched between a top complementary nanocross array and a bottom metal ground plane. Bias voltage is applied across the semiconductor layer with top and bottom metal films acting as electrodes. (b) Simulated metasurface absorption at different bias voltages. Black dash lines trace the positions of the two polaritonic peaks at different DC bias voltages and polaritonic splitting of the absorption peak is clearly visible. For clarity, the absorption curves at different bias voltages are offset from each other vertically by 15%. (c) Simulated distribution of normal electric field component and its enhancement relative to the incident field magnitude in the semiconductor layer 100 nm below the complementary nanocross array. Simulations are performed at λ=6.75 μm and zero bias voltage [90].

In the simulation, commercial Maxwell's equations solver (CST studio) based on the finite-integration method in frequency domain was used to compute the reflectance and E-field distribution in the MQW layer. Periodic boundary conditions were placed around the unit cell and open boundary conditions were placed in the perpendicular direction of the top device surface. Because of the ground plane, the transmittance of the metasurface was zero and the absorbance A was calculated as $A=1-R$, where R is the power reflectance of the metasurface.

As follows from Equation 4.1 and as shown in Fig. 4.1 (d), the refractive index change is particularly strong for frequencies close to the intersubband transition frequency ω_{12}. Consequently, in order to achieve the maximum tuning range, the complimentary cross nanostructures were designed to have a resonance close to intersubband transition frequency ω_{12} for zero bias. In this case, the electromagnetic modes in metallic nanostructures are polaritonically coupled to the intersubband transition 1-2 in the MQW layer. The polaritonic absorption peak splitting can be seen in the simulated absorption spectra of the metasurface at normal incidence shown in Fig. 4.2 (b). The vacuum Rabi energy splitting is calculated to be $2\hbar\Omega_R = 16.7\,meV$, in good agreement with simulation results [81-82]. Figure 4.2 (b) also shows how the metasurface absorption is expected to change as the transition frequency between electron subbands 1 and 2 is tuned by the bias voltage. Figure 4.2 (c) shows the distribution of surface normal component of E-field induced in the MQW layer by input light at normal incidence. We note that, due to the symmetry of complimentary nanoscross structures, the same response is achieved for any light polarization at normal incidence.

4.3 DEVICE FABRICATION

Experimentally, a 400 μm by 400 μm two-dimensional array of nanoresonators, as shown in Fig. 4.2 (a), was patterned on top of the MQW layer metal-bonded to a semiconductor substrate. Figure 4.3 shows the fabrication steps of the metasurface. MQW structures were grown by the molecular beam epitaxy on a semi-insulating InP substrate. The growth started with a 300-nm-thick etch-stop layer of $In_{0.53}Ga_{0.47}As$, followed by a 100-nm-thick etch-stop layer of InP, followed by the MQW structure. A 10-nm-thick layer of titanium, a 50-nm-thick layer of platinum, and a 500-nm-thick layer of gold were subsequently evaporated on top of the MQW layer. The wafer was then thermo-compressively bonded epi-side down to a semi-insulating InP wafer coated with the same metal layers. The InP substrate on the MQW wafer was then removed via mechanical polishing and selective wet-etching, followed by the removal of the etch-stop layers via selective wet-etching. A 400 μm by 400 μm array of complementary crosses was produced on the MQW layer with e-beam lithography, evaporation of a 5-nm-thick layer of titanium and 40-nm-thick layer of gold, and lift-off. A 700 μm by 700 μm of square mesa structure was then etched in the MQW layer all the way to the bottom metal contact layer with the patterned complimentary cross array in the center of the mesa. A 1.5 mm by 1.5 mm square patch made of 500-nm thick layer of SU-8 photoresist was then deposited on top of the mesa and surrounding area with a 400 μm by 400 μm of square opening on top of the nanocross array. Finally, a 1.4 mm by 1.4 mm top metal contact layer with a window across the nanocross pattern was fabricated on top of the SU-8 patch. The contact layer is made of a 10-nm-thick layer of titanium and 150-nm-thick layer of gold and it contacts the borders of the nanocross array. Finally the device was mounted on a copper block and wire-bonded to apply a bias voltage.

Figure 4.4 (a)-(c) show a top view of the scanning electron microscope image of the complete wire-bonded device (Fig. 4.4 (a)), details of the top surface pattern (Fig. 4.4 (b)), and a side view of the cleaved facet of the metasurface showing the MQW layer above the metal ground plane bonded to a substrate (Fig. 4.4 (c)). Details of the process technique and recipes of each step are described as follows:

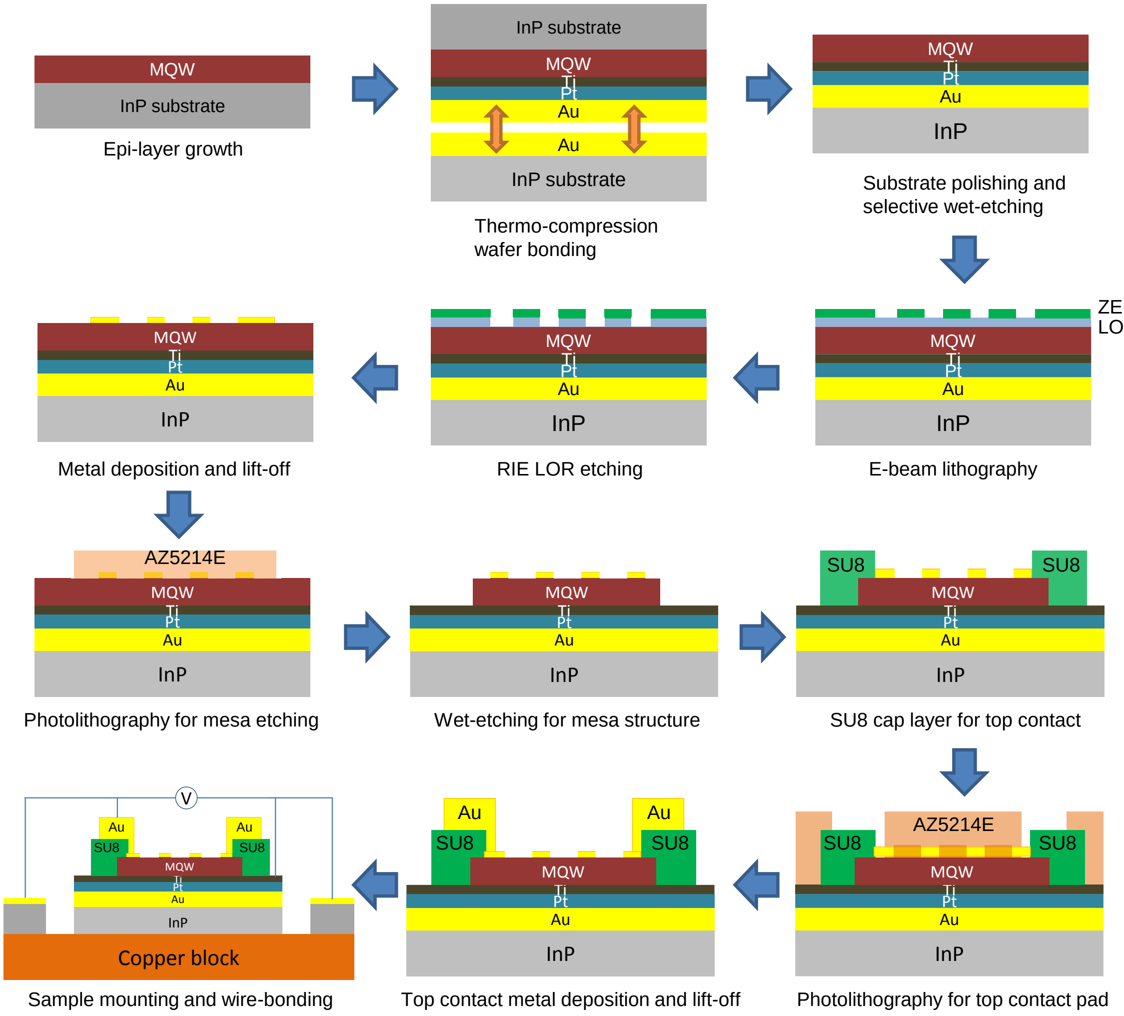

Figure 4.3: Facet-view schematic drawing of the fabrication process steps of metasurface. Arrows indicate order of fabrication steps.

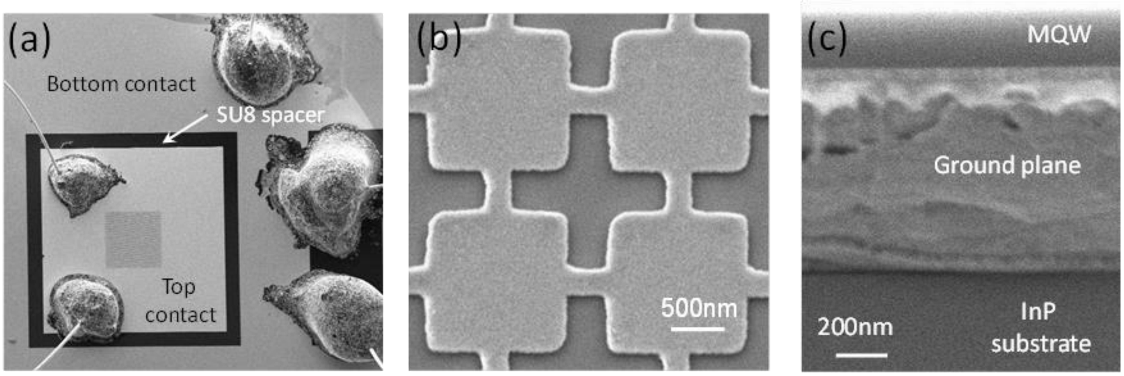

Figure 4.4: Fabricated metasurface. (a-c) Scanning electron microscope images of the wire-bonded device (a), the complementary crosses (b), and a side view of the cleaved facet with the MQW layer metal-bonded to InP substrate (c) [90].

Epi-layer design and growth

The coupled quantum well structure for electrically tunable optical response was designed using a self-consistent Poisson-Schrodinger solver. In this work, we used a particular composition of two materials, $In_{0.53}Ga_{0.47}As/In_{0.52}Al_{0.48}As$, in which the lattice constant of the layers is virtually identical to that of InP substrate. The growth parameters of layers are shown in Table 4.1. The multi-quantum well layers of our structure were grown by Molecular-Beam Epitaxy (MBE).

Matrix Layers				
Layer	Material	[nm]	Ratio	Doping (cm-3)
1	InGaAs	300	In53Ga47As	
2	InP	100		
3	InGaAs	5	In53Ga47As	1.00E+18
4	AlInAs	3	Al48In52As	
5	AlInAs	7	Al48In52As	1.00E+18
Start of 7 repeat periods				
6S1	AlInAs	7	Al48In52As	1.00E+18
7S1	AlInAs	3	Al48In52As	
8S1	InGaAs	4.7	In53Ga47As	
9S1	AlInAs	1	Al48In52As	
10S1	InGaAs	1.9	In53Ga47As	
11S1	AlInAs	3	Al48In52As	
12S1	AlInAs	7	Al48In52As	1.00E+18
End of repeat periods				
13	AlInAs	7	Al48In52As	1.00E+18
14	AlInAs	3	Al48In52As	
15	InGaAs	5	In53Ga47As	1.00E+18

Table 4.1: Multi-quantum well growth parameters. The semiconductor layers were grown on semi-insulating InP substrate.

Wafer bonding

For MQW layer transfer onto a metal ground plane, Au-Au thermo-compression wafer bonding was used. The initial wafer was cleaned by oxygen Reactive Ion Etching (RIE) (Oxford RIE, O_2 50sccm, pressure 50mtorr, RF 75W, for 2min) and by dipping in BOE (buffered oxide etchant) for a few seconds in order to remove surface oxidation and to improve adhesion of metal layers onto the wafer. 10nm of titanium, 50nm of platinum, and 400nm of gold were evaporated on the epi-layer grown wafer and another InP bare wafer. The platinum layer is a metal diffusion blocking layer while wafer bonding. Metallization defects were checked prior to placing the wafers on a tungsten plate in AML wafer bonding machine. Then the two wafers are placed and aligned on the tungsten plate and a graphite sheet is placed above the parts. After closing the chamber, the parts were clamped with 100N before pumping. The chamber is evacuated to below 5×10^{-4} torr and was heated to 320^{o}C with a light clamping force (~200N). When the upper and lower plate reached temperature, 4.5kN of clamping force was applied for 15 minutes. After that, the upper and lower plates were cooled to below 200^{o}C with the force maintained. Finally, the bonded sample is inspected.

Substrate removal

After the wafer bonding, the InP substrate on the MQW wafer was removed via mechanical polishing and selective wet-etching. In the mechanical polishing process, a slide glass is bonded on a polishing block with crystal glue, and the bonded wafer is bonded on the slide glass with crystal glue. Initial thickness of the sample is recorded. SiC get is diluted with DI water on a polishing stage and the sample is grinded on the diluted SiC gel and 150~200μm-thick substrate is thinned down from initially 350μm-thick InP substrate. The thickness of the sample is monitored while grinding. Uniformity of the thickness should be smaller than 0.02mm for uniform wet-etching. The mechanically polished sample is detached from the polishing block and is cleaned with Acetone and IPA and then again attached to a slide glass with crystal glue. The remaining InP substrate layer is then etched by dipping in HCl : DI water = 3(300ml) : 1(100ml) (InP etch rate : ~10μm/min, etch stop at $In_{0.53}Ga_{0.47}As$ layer) solution until shiny surface is revealed and the sample is rinsed in DI water. Now the top layer of the sample is a 300nm of InGaAs and the layer is etched by dipping in H3PO4 : H2O2 : DI water = 1(50ml) : 1(50ml) : 38(1900ml) solution for about 2min 30sec ($In_{0.53}Ga_{0.47}As$ etch rate: ~2nm/sec, etch stop at InP layer) until the surface color turns uniform (The surface color is purple for the 220nm-thick MQW layer). The sample is then rinsed in DI water.

Finally, 100nm-thick InP layer is etched by dipping in HCl : DI water = 3(300ml) : 1(100ml) solution for a few seconds until the surface color turns uniform and the sample is rinsed with DI water. Finally, the MQW layer is transferred onto the metal ground plane.

Electron-Beam Lithography (EBL) and LOR layer RIE etching

To make an array of nanocrosses, electron-beam lithography was used. The MQW layer transferred onto the metal ground plane should be cleaned by oxygen RIE (Oxford RIE, O_2 50sccm, pressure 50mtorr, RF 75W, for 2min) and by dipping in BOE for a few seconds to remove surface oxidation and improve adhesion of metal layers onto the sample. Skipping this surface cleaning process will cause a failure in metal lift off. LOR 0.7A is coated on the sample with 4000rpm spinning for 1min and baked at 180°C for 1min. Then, ZEP (positive e-beam resist) is coated on the sample with 4000rpm spinning for 1min and baked at 180°C for 2min. The sample is loaded in a cassette 2A in Jeol 6000 FSE EBL machine and a 400μm by 400μm of designed nanocross array is patterned (EOS7, 100pA, area dose: 180μC/cm^2, linedose: 0.12nC/cm, shotmodule: -50). After ebeam patterning, the sample is developed in ZEP developer for 2min and rinsed in IPA. Since LOR layer is inert to electron-beam and ZEP developer, oxygen RIE is used to etch the revealed LOR layer (Oxford RIE, O_2 50sccm, pressure 50mtorr, RF 75W, for 1min 30sec). RIE etching time will vary based on machine conditions.

Metal deposition and Lift-off

For metal deposition, the CHA, a multi-crucible electron beam evaporator, was used. The system can accommodate up to four crucibles at a time to allow multiple and sequential deposition. The metal layers consist of a 5nm-thick layer of titanium (for metal adhesion) and a 40nm-thick layer of gold. After the metal deposition, the sample is placed in Remover PG at 70ºC for 1hour. Then the sample is rinsed in DI water and placed in a plastic beaker with acetone. For complete lift-off, ultra-sonication is used for only a second. In this lift-off process, the sample should not be dried; otherwise the unlifted portion of the array will be very difficult to remove and may need longer ultra-sonication.

Photolithography

In the process of the device fabrication, several photo-resist (PR) patterns by photolithography were needed. For mesa structure etching, a 700µm by 700µm of square PR pattern is made using AZ5214 (positive PR). The PR coated on the sample with 4000rpm for 1 minute and baked at 100ºC on a hot-plate for 1 minute. The sample is aligned with a photomask and exposed to UV light for 4 seconds. And the pattern is developed in 726MIF developer for 1 minute. Secondly for SU8 cap layer patterning, the photomask is cleaned in piranha solution for 8 minutes. SU8 2000.5 (negative PR) is coated on the sample with 3000rpm for 1min and the sample is baked at 100 ºC for 1 minute. And the sample is aligned with the photomask and exposed to UV light for 20 seconds. The sample is post-baked at 100 ºC on a hot-plate for 2 minutes and developed in SU8 developer for 1 minute and rinsed in IPA. Finally for a thick top metal contact layer patterning, AZ5214E is coated on the sample with 4000rpm for 1 minute and pre-baked at 90 ºC on a hot-plate for 5 minutes. The sample is aligned with the photomask and exposed to UV light for 4 seconds. Then the sample is post-baked at 115 ºC on a hot-plate for 90 seconds and exposed to UV light for 100 seconds (flood exposure for image reversal process). The sample is developed in 726MIF developer for 1 minute and rinsed in DI water.

4.4 EXPERIMENTAL RESULTS

For initial characterization, we measured the intersubband absorption spectrum from epi-grown MQW layer after background correction. The experimental intersubband absorption spectrum gives actual electron transition energy between electron subbands in the MQW structure and transition linewidth which can be extracted from Full Width Half Maximum (FWHM) of the intersubband absorption spectrum. Given the close agreement between calculated and measured transition energies and the typically high accuracy of band structure calculations, we assume that transition dipole moments for intersubband transitions between states 1 and 2 in the MQW structure are the same as simulated in Fig. 4.1 (a)-(c). In this measurement, initial wafer was polished to have facets at 45° to the surface normal and its top and bottom surfaces were gold-coated. Figure 4.5 shows schematic of optical setup used for intersubband absorption measurement.

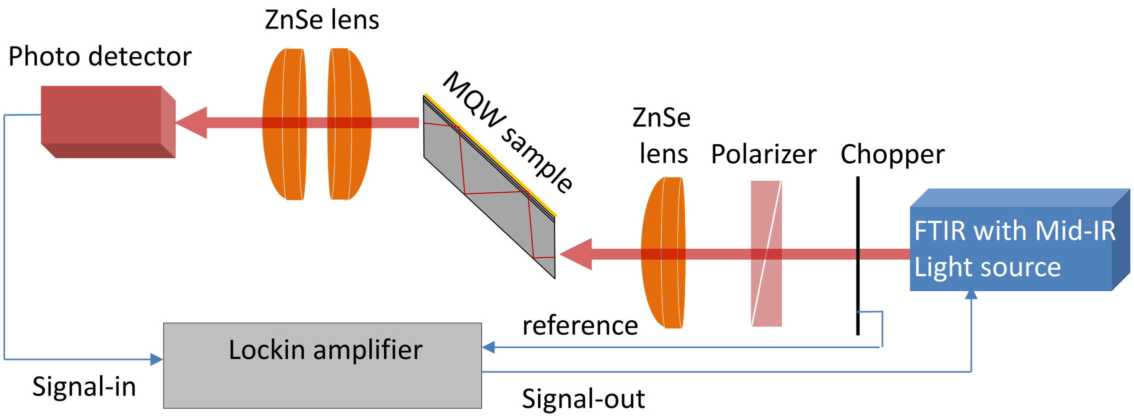

Figure 4.5: Intersubband absorption measurement setup. Unpolarized continuous Mid-IR light from Fourier Transform Infrared Spectrometer (FTIR) passes through a linear polarizer and is focused onto one facet of MQW sample. Mid-IR light passed in multipass geometry of MQW sample is then detected from a photodetector.

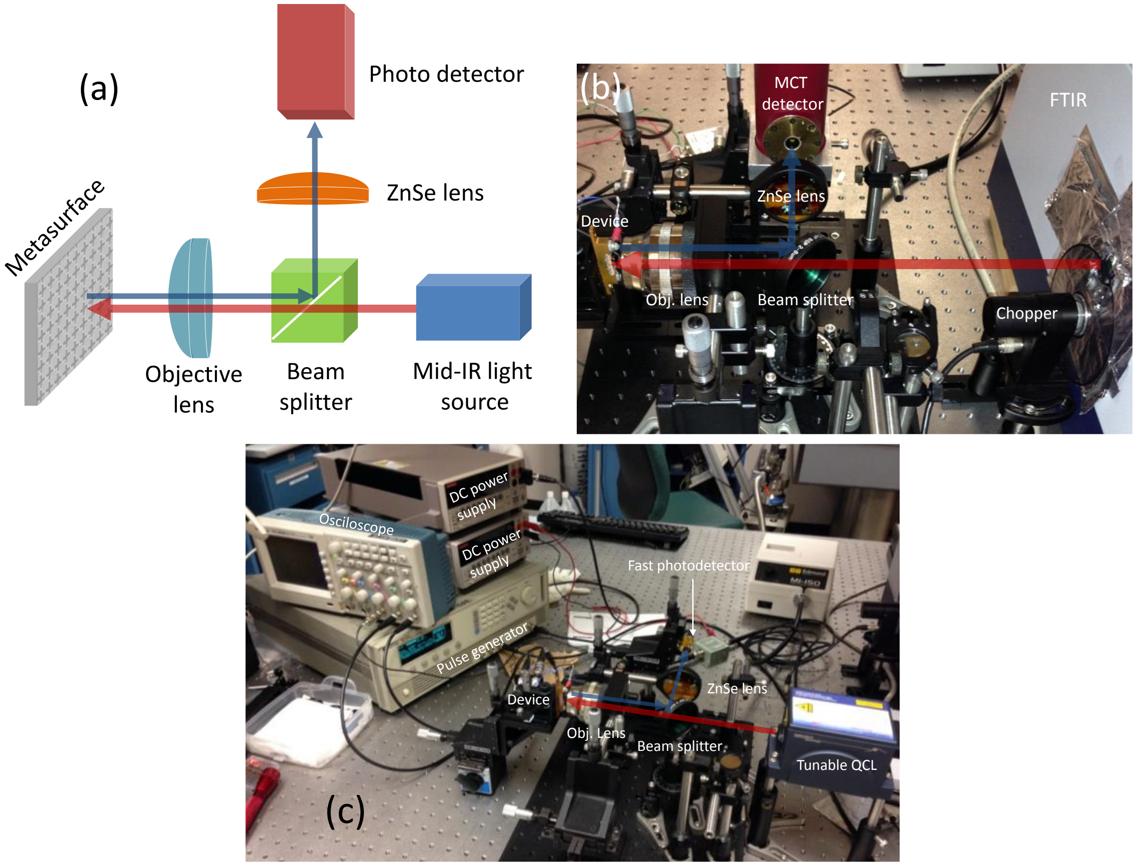

Figure 4.6: Optical setup used for metasurface characterization. (a) Schematic of optical setup. Mid-IR light source can be either a broadband thermal output from a Fourier-transform infrared spectrometer or a broadly tunable quantum cascade laser. (b) photo-image of actual optical setup for DC biased absorption measurement. (c) photo-image of actual optical setup for high speed modulation measurement.

A schematic of the optical setup for the metasurface measurement is illustrated in Fig. 4.6 (a). For initial characterization, we measured absorption spectra of the metasurface for different applied DC bias voltages from -5 V to +5 V with a 1V step. Actual setup used for this measurement is shown in Fig. 4.6 (b). A Fourier-transform infrared spectrometer (FTIR) was used for the spectral measurement of the metasurface. Broadband mid-infrared light from the FTIR thermal source passed through a chopper and a non-polarizing achromatic 50% beam splitter, and was focused on a sample at normal incidence through a numerical aperture 0.5 lens. The reflected signal was collected by the same objective lens and was directed by the beam splitter towards a liquid nitrogen cooled mercury cadmium telluride (MCT) photo-detector (Kolmar Technologies, Inc.) through another lens. The reflection spectrum from the metasurface was normalized using the reflected signal from a gold mirror as a reference. The measurement data is shown in Fig. 4.7. The intersubband transition frequency ω_{21} increases with the DC bias, consistent with Figure 1, and reflected in the variation of the absorption spectrum. The measured peak absorption shifts by over 0.3 μm from 6.78 μm to 7.09 μm with a change in bias voltage of only 2 V between +1 V and +3 V. Current-voltage measurements of the metasurface in Figure 4b reveal very low current density below 20 A/cm^2 for up to 5V bias voltage. Simulation of a temperature increase in our structures due to electrical power dissipation shows only 0.04°C temperature increase under +5 V DC biasing, which shows that our structures require no cooling system for operation.

The experimentally observed spectra in Fig. 4.7 are in good agreement with our simulations in Fig. 4.2 (b), although higher bias voltages were required to experimentally realize optical tuning. This is most likely the effect of contact resistance at the semiconductor-metal interfaces in the top and bottom electrodes. We note that, due to small thickness of the semiconductor heterostructures of our metasurfaces, we did not use heavily-doped ‘contact layers’ and our contacts are non-alloyed.

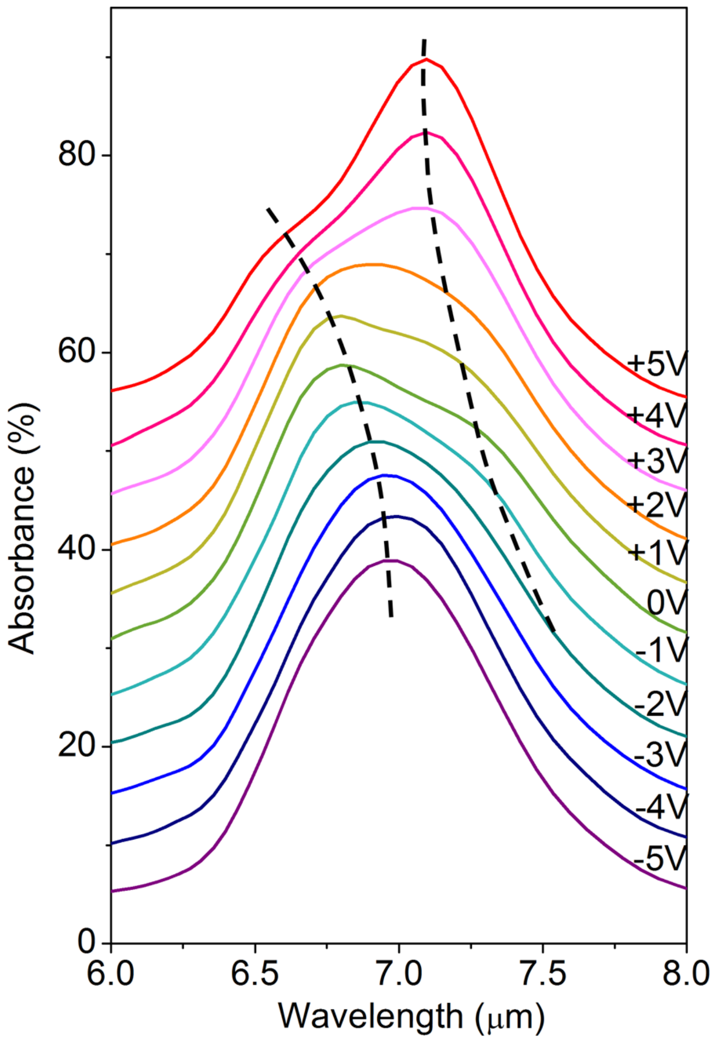

Figure 4.7: Experimental absorption spectra of the metasurface for different DC bias voltages from -5V to 5V with 1V step. For clarity, the absorption curves at different bias voltages are offset from each other vertically by 5%. Black dash lines trace the positions of the two polaritonic peaks at different DC bias voltages [90].

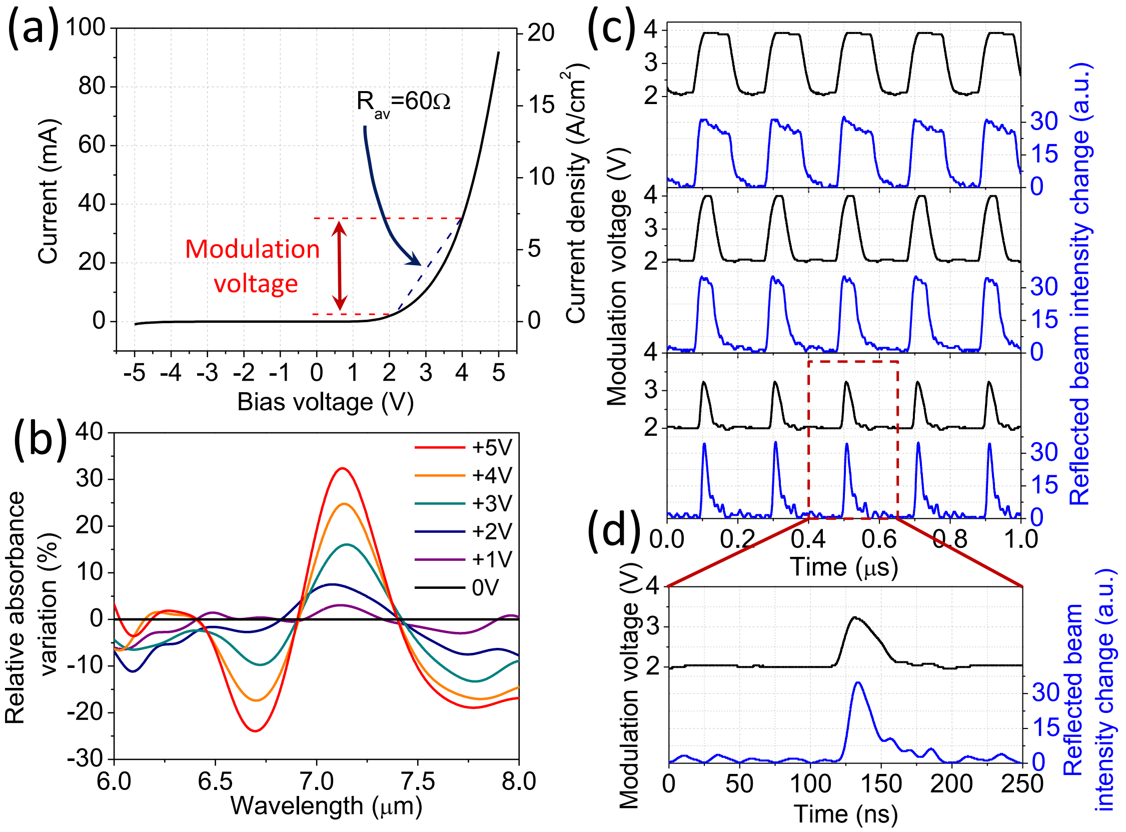

Figure 4.8: (a) Current-voltage characteristic of the metasurface. (b) Absorption amplitude modulation for positive DC bias voltages deduced from Fig. 4.7. (c) High speed modulation measurements. Oscilloscope traces of the modulation voltage on the metasurface and the corresponding light intensity modulation of the reflected beam are shown. All intensity modulation traces use the same units. We applied voltages pulses with different pulse widths: 100ns (top panel), 50ns (middle panel), and 10ns (bottom panel) at 5MHz repetition frequency. (d) Zoom-in of the data for metasurface modulation with 10ns pulses [90].

Figure 4.8 (b) shows the variation of metasurface absorbance for different DC bias voltages, defined as $(A_{V_{DC}} - A_{V_{DC}=0V}) / A_{V_{DC}=0V}$, where $A_{V_{DC}=0V}$ and $A_{V_{DC}}$ are the metasurface absorbance in percent for zero bias, and applied voltage V, respectively. Strong metasurface absorbance (or reflectivity) modulation is achieved around 6.72 μm and 7.12 μm wavelengths. In particular, over 30% of absorbance change is achieved around a wavelength of 7.12 μm by changing bias voltage from 0V to +5V. Since the tuning is achieved by electro-optic effects due to Stark shift of the intersubband transition energy and it requires no carrier transport across the MQW layer, the frequency response of the device is only determined by the RC time constant of the biasing circuit.

For high-frequency modulation measurements, a continuous-wave broadly tunable quantum cascade laser (Daylight solutions, Inc.) was used instead of an FTIR thermal source and a fast mid-IR photovoltaic mercury cadmium telluride (MCT) detector (Vigo System S.A., time constant < 1ns) was used instead of slow cryogenically cooled MCT detector in the optical setup described earlier and shown in Fig. 4.6 (a) and (c). Voltage pulses across the metasurface and the modulated signal from the MCT detector were moditored simultaneously on the multi-channel oscilloscope.

Ultrafast reflectivity switching was verified by observing intensity variation of the reflected QCL light at λ=6.75 μm, close to the strong intensity modulation region measured in Fig. 4.8 (b). The bias voltage on the structure was modulated between +2 V and +4 V as confirmed by the oscilloscope traces shown in Fig. 4.8 (c). To achieve such voltage modulation, we sent short pulses with +2 V amplitude through bias tee with +2 V DC bias. The RC time constant of our structure for such modulation is calculated to be approximately 8 ns using the average structure resistance of approximately 60 Ω in +2~4 V range obtained from the current-voltage characteristics shown in Fig. 4.8 (a) and the structure capacitance of 140 pF calculated using the structure dimensions. The total device capacitance of the structure is calculated by summing the capacitance of a 400×400 μm^2 section of nanocrosses on 220 nm MQW layer, 700×700 μm^2 of mesa section with 500-nm-thick layer of SU-8 on top of the 220nm MQW layer, less 400×400 μm^2 center section, and 1.4×1.4 mm^2 500-nm-thick layer of SU-8 on top of ground plane, less the 700×700μm^2 mesa structure. The dielectric constant of the MQW layer was taken to be $\varepsilon_{MQW} \approx 10$ from ref. 91 and that of SU-8 was taken to be $\varepsilon_{SU-8} \approx 2.5$ from the manufacturer specifications sheet (Microchem Corp.). We note that the RC time constant of our metasurface may be significantly improved by reducing the nanoresonator array and contact area sizes. A thermoelectrically-cooled mercury cadmium telluride detector with response time of 1 ns was used to detect the intensity modulation of the reflected light. Figure 4.8 (c) shows oscilloscope traces of the reflected light intensity and corresponding traces showing voltage modulation on the metasurface. Modulation voltage pulses of 100 ns, 50 ns, and 10 ns were sent to the metasurface at 5 MHz repetition frequency and the data shows that reflected beam intensity follows the shape of the voltage pulses with high accuracy. Modulation depth of the reflected light intensity stays approximately constant for all pulse durations as seen in Figure 4d. We note that the voltage pulse width of 10 ns is the minimum pulse width that was available from the pulser in our laboratory, and the measured signals indicate that much faster modulation speeds may be achieved with these polaritonic metasurfaces, since, fundamentally, the response time is only limited by the RC time constant of the associated circuitry.

4.5 CONCLUSION

Tunable polaritonic metasurfaces presented in this work represent a new class of ultra-fast reconfigurable metamaterials that achieve the desired optical properties by polaritonic coupling of quantum-engineered transitions between electronic states with electromagnetically-engineered modes of metallic nanoresonators. Our design approach allows producing metasurfaces with new functionalities, such as rapidly-tunable optical response plasmonic nanoresonators reported here, as well as large optical nonlinearities and signal amplification in electrically-pumped structures. Compared to tunable metasurfaces based on hybrid metal−graphene structures, which have attracted significant attention recently [71-75,92], the metasurfaces presented here offer the significant advantages of lower modulation voltages, robust and well-established fabrication technology, and potentially larger modulation speeds. Since tuning in our structures is achieved by an electro-optic effect that requires no electron transport in the MQW layers, the modulation speed may be pushed well within the GHz range and above. The experimental results reported here represent a proof-of-concept experimental demonstration, and we expect further improvements in speed and intensity modulation depth in future structures based on smaller-sized elements with reduced RC time constant and optimized nanoresonators designs. The metasurface geometry presented here is well-suited for integration into various voltage-reconfigurable flat optical elements for, e.g., real-time beam steering and polarization control using polarization-sensitive plasmonic nanoresonators.

Chapter 5

Second Harmonic Generation from Highly-Nonlinear Ultra-Thin Metasurfaces Coupled to Intersubband Transitions[4]

5.1 INTRODUCTION

Intersubband transitions in *n*-doped semiconductor heterostructures provide the possibility to quantum-engineer one of the largest known nonlinear optical responses in condensed matter systems, limited however to electric field polarized normal to the semiconductor layers [20,93-98]. In a different context, plasmonic metasurfaces have been proposed in various scenarios to strongly enhance light-matter interaction and realize ultrathin planarized devices with exotic wave properties [57,58,62,99]. In this work, we propose and experimentally realize metasurfaces with record-high nonlinear response based on the coupling of electromagnetic modes in plasmonic metasurfaces with quantum-engineered intersubband transitions in semiconductor heterostructures. We show that it is possible to engineer virtually any element of the nonlinear susceptibility tensor of these structures and we experimentally verify this concept by realizing a 400-nm-thick metasurface with nonlinear susceptibility of over 5×10^4 pm/V for second harmonic generation (SHG) at $\lambda\approx8$ μm under normal incidence, which is many orders of magnitude larger than any second-order nonlinear response in optical metasurfaces measured to date [100-103]. The proposed structures can act as ultrathin highly-nonlinear optical elements that enable efficient frequency mixing with relaxed phase-matching conditions, ideal to realize broadband frequency up- and down-conversions, phase conjugation and all-optical control and tunability over a surface.

---

[4] J. Lee *et al.*, Giant nonlinear response from plasmonic metasurfaces coupled to intersubband transitions. *Nature*, **511**, 65, (2014).

The field of optical metamaterials has shown exciting advances in recent years, with many demonstrated applications based on their linear interaction with light, including super-resolution imaging [104,105] and optical cloaking [106-108]. More recently, optical metamaterials with tailored nonlinear response have opened new degrees of freedom in metamaterial design, with interesting venues for super-resolution imaging [109], for performing efficient frequency conversion and optical control with greatly-relaxed phase-matching conditions [110], as well as for optical switching and memories at the nanoscale [111].

So far, nonlinearities in metamaterials have been mostly realized by exploiting the natural nonlinear response of plasmonic metals [100,101] or by enhancing the nonlinearity of optical crystals using plasmonic nanoantennas [102,103]. A different approach to realize large nonlinear optical response has been put forward by quantum-engineering intersubband transitions in *n*-doped multi-quantum-well (MQW) semiconductor heterostructures [20,93-98]. By controlling the width of wells and barriers in the MQW structures, one can tailor the transition energy and dipole moments between electron subbands, so as to maximize the quantum-mechanical expressions for a nonlinear process of choice, producing one of the largest known nonlinear responses, up to 6 orders of magnitude larger than that of traditional nonlinear optical materials [20,93-98]. Voltage may be used to modify and spectrally tune intersubband nonlinearities [20] and electrical pumping may be used to produce active intersubband structures with full loss-compensation for both second-order [94-96] and third-order [112] nonlinear processes.

Nonlinear MQW structures have been successfully integrated into waveguide-based systems to produce efficient frequency conversion [24,94-98], and have enabled the development of mass-producible room-temperature electrically-pumped sources of

THz radiation [96]. Nearly 1% of SHG power conversion efficiency at 8.6 μm fundamental frequency was achieved in waveguides with passive $In_{0.53}Ga_{0.47}As/Al_{0.48}In_{0.52}As$ MQW structures [24] and over 16% power conversion efficiency was theoretically predicted [113]. However, the integration of giant MQW nonlinearities with free-space optics is very challenging because optical transitions between electron subbands are intrinsically polarized along the surface normal to the MQW layers (taken to be the *z*-axis in this paper).

In a different context, properly patterned metallic surfaces supporting highly confined plasmonic resonances have been proposed for a variety of exciting applications, including enhanced light-matter interaction at the subwavelength scale, polarization conversion, control of optical transmission and radiation, enhanced chirality, asymmetric transmission and filtering [62]. In order to overcome the current limitations of MQW systems, and further enhance the intersubband nonlinear response, we propose to combine the MQW layered substrates with suitably designed plasmonic metasurfaces. In the following we theoretically and experimentally demonstrate that, by combining quantum-electronic engineering of intersubband nonlinearities with electromagnetic engineering of plasmonic nanoresonators, we unveil ultrathin, planarized, highly nonlinear optical metasurfaces. This approach allows us to create large-area metasurfaces in which virtually any element of the nonlinear susceptibility tensor may be ad-hoc engineered to have a giant nonlinear response. The impact of these ultrathin devices may be groundbreaking in a variety of fields, including THz generation and detection, phase conjugation, and other nonlinear processes.

5.2 PROOF-OF-CONCEPT DEMONSTRATION

5.2.1 MQW Design and Optical Properties

Figure 5.1 (a) shows the band diagram of a In$_{0.53}$Ga$_{0.47}$As/Al$_{0.52}$In$_{0.48}$As coupled quantum well structure, repeated multiple times to produce the 400-nm-thick MQW layer used in our experiments. This structure is designed using a self-consistent Poisson-

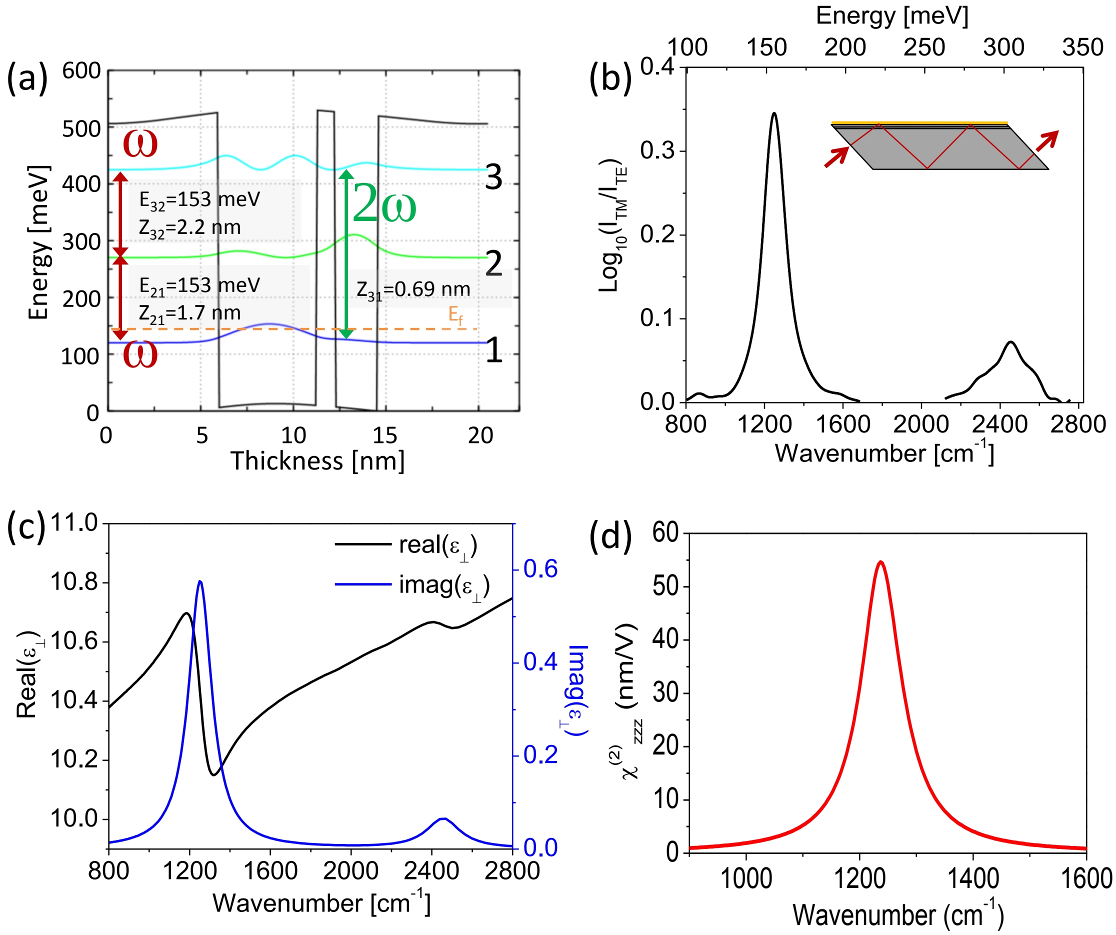

Figure 5.1: Multi-quantum well structure and optical parameters. (a) Conduction band diagram of one period of an In$_{0.53}$Ga$_{0.47}$As/Al$_{0.52}$In$_{0.48}$As coupled quantum well structure designed for giant nonlinear response for SHG. The layer sequence (in nm) is **6.0**/5.3/**1**/2.3/**6.0**, where AlInAs barriers are shown in bold, and the first 3nm of the first 6nm barrier and the last 3nm of the last 6nm barrier are n-doped to 5×10^{17}cm^{-3}. (b) Intersubband absorption spectrum of the wafer used in experiment after background correction. Inset: measurement geometry. (c) Real and imaginary part of dielectric constant for out-of-plane (ε$_\perp$). (d) Intersubband nonlinear susceptibility of the structure in (a) as a function of pump frequency for SHG.

Schrodinger solver to support a giant resonant nonlinear response for SHG at $1/\lambda \approx 1240$ cm^{-1} ($\lambda \approx 8$ μm). The layer sequence (in nanometers) is **6.0**/5.3/**1**/2.3/**6.0** where AlInAs barriers are shown in bold, and the first 3 nm of the first 6-nm-barrier and the last 3 nm of the last 6-nm-barrier are n-doped to 5×10^{17} cm^{-3}. Figure 5.1 (b) shows the experimentally-measured intersubband absorption spectrum after background correction. The spectrum is obtained in a multipass geometry using the original InP wafer with the MQW layer on top. The wafer was polished to have facets at 45 degrees to surface normal and its top and bottom surfaces were gold-coated, as shown in the inset of Fig. 5.1 (b). This measurement approach follows a standard procedure as described, e.g., in Ref. [20]. Assuming unpolarized sample illumination from the Fourier Transform Infrared Spectrometer (FTIR) thermal source and neglecting standing wave effects, the intersubband absorption coefficient α_W is given as [20]:

$$\alpha_W = -\frac{1}{L_{\text{int}}} \ln(10) Log_{10}\left(\frac{I_{TM}}{I_{TE}}\right), \tag{5.1}$$

where L_{int} is the interaction length defined as20

$$\text{L}_{\text{int}} = \frac{\text{n}_\text{p} L_{QW} N}{\cos(\theta)} \ , \tag{5.2}$$

where θ the angle of incidence with respect to the normal to the plane of the layers (45° in our case), L_{QW} is the thickness of each coupled quantum well section ($L_{QW}=20.6\ nm$ in our case), N is the total number of sections in the MQW sample ($N=28$ in our case), and n_p is the number of passes through the MQW layer. Given our sample geometry (5 mm in length and 0.33 mm in thickness), we estimate $n_p=14$. From Fig. 5.1 (b), we obtain transition $\hbar\omega_{21} \approx 155\ meV$ and $\hbar\omega_{31} \approx 306\ meV$ in excellent agreement with calculated values of 153 meV and 306 meV, respectively, as shown in Fig. 1a. The measured transition linewidths are $2\hbar\gamma_{21} \approx 15\ meV$, $2\hbar\gamma_{31} \approx 17\ meV$ and the peak absorption α_W =615 cm^{-1} and 171 cm^{-1} for 2-1 transition and 3-1 transition, respectively. Given close agreement between calculated and measured transition energies and typically high accuracy of bandstructure calculations, we assume the transition dipole moments for intersubband transitions between states 1,2, and 3 in our structure are the same as simulated in Fig. 5.1 (a). The values of intersubband absorption α_W then allows us to estimate the actual doping level N_e in our structure, which may be different from the nominal doping used during growth. To that end, we express α_W through the dielectric constant for out-of-plane ($\varepsilon_\perp$) E-field polarization as [20]

$$\alpha_W = 2\frac{\omega}{c}\operatorname{Im}\left(\sqrt{\varepsilon_\perp}\right)\sin^2(\theta), \tag{5.3}$$

where

$$\varepsilon_\perp(\omega) \approx \varepsilon_{core}(\omega) + \frac{N_e\left(eZ_{12}\right)^2}{\varepsilon_0\hbar\left(\left(\omega_{21}-\omega\right)-i\gamma_{21}\right)} + \frac{N_e\left(eZ_{31}\right)^2}{\varepsilon_0\hbar\left(\left(\omega_{31}-\omega\right)-i\gamma_{31}\right)}, \tag{5.4}$$

Plugging the experimental values of $\hbar\omega_{ij}$ and $\hbar\gamma_{ij}$, and calculated transition dipole moments z_{ij} into the expressions above we obtain $\alpha_W \approx$620 cm^{-1} at 2-1 resonance and $\alpha_W \approx$*180 cm*$^{-1}$ for 3-1 using N_e=0.75×10^{17} cm^{-3}, in close agreement with measurements. It is the value that is used for $\chi^{(2)}$ calculations. We note that the experimental value of N_e is a factor of 2 smaller than the nominal doping density. Dielectric constant for out-of-plane electric field is calculated and plotted in Fig. 5.1 (c).

The expression for the intersubband nonlinear susceptibility tensor element for SHG at pump frequencies close to intersubband resonances may be approximately written as [19]:

$$\chi_{zzz}^{(2)}(\omega\rightarrow 2\omega)\approx N_e\frac{e^3}{\hbar^2\varepsilon_0}\frac{z_{12}z_{23}z_{31}}{(\omega_{31}-2\omega-i\gamma_{31})(\omega_{21}-\omega-i\gamma_{21})}\ , \tag{5.6}$$

where ω is the pump frequency, e is the electron charge, N_e is the average bulk doping density, $\hbar\omega_{ij}$, $\hbar\gamma_{ij}$, and ez_{ij} are the energy, linewidth, and dipole moment, respectively, for a transition between states i and j. The values of $\chi_{zzz}^{(2)}$ in Fig. 5.1 (d) are calculated using the expression above, assuming calculated transition dipole moments ez_{ij} and experimentally-measured values of $\hbar\omega_{21}\approx 155\ meV$, $\hbar\omega_{21}\approx 306\ meV$, $2\hbar\gamma_{21}\approx 15\ meV$, $2\hbar\gamma_{31}\approx 17\ meV$ and $N_e\approx 0.75\times 10^{17}\ cm^{-3}$ obtained from intersubband absorption measurements as described above.

The dielectric constant in the MQW layer for the out-of-plane ($\varepsilon_\perp$) E-field polarization is given in Eq. (5.4), the dielectric constant for the in-plane ($\varepsilon_{//}$) E-field polarization is calculated as

$$\varepsilon_{//}(\omega)\approx\varepsilon_{core}(\omega)+i\frac{N_e e^2\tau}{\varepsilon_0\omega m^*\left(1-i\omega\tau_D\right)}, \tag{5.7}$$

where $\varepsilon_{core}(\omega)$ is the dielectric constant of the MQW with N_e=0 and electrons motion in plane of semiconductor layers is assumed to be free with the Drude relaxation time $\tau_D\approx 10^{-13}$ s, which is a typical value for the InGaAs/AlInAs material with low doping density.

Figure 5.1 (d) plots the absolute value of the SHG nonlinear susceptibility tensor element $\chi^{(2)}_{zzz}$ as a function of pump frequency calculated for this structure as described in Methods. The nonlinear response peaks at approximately 54 nm/V, nearly 3 orders of magnitude larger than the largest $\chi^{(2)}$ coefficient of natural optical materials [19].

5.2.2 Metasurface Design and Simulations

The MQW layer is then sandwiched between a metal ground plane and a patterned array of metallic nanostructures, as shown in Fig. 5.2 (a)-(c). This grounded metasurface can be designed to enable efficient coupling of plasmonic modes with *z*-polarized intersubband transitions, drastically enhancing light-matter interaction and converting the impinging transverse field polarization to the desired *z*-direction [83]. Even though a ground plane is used in our metasurface design, efficient coupling of intersubband transitions with resonant metallic nanostructures may also be achieved without using a ground plane, as shown recently [114], which may allow easily translating the results presented here in transmission mode.

Since our goal is to enhance SHG, the plasmonic nanostructures are designed to induce and enhance the local electric field at both fundamental frequency (FF) ω and second-harmonic frequency (SH) 2ω. The plasmonic nanostructures must also lack inversion symmetry in x-y plane, otherwise all nonlinear susceptibility tensor elements $\chi^{(2)}_{ijk}$ with *i*,*j*, and *k* being *x* or *y* would vanish by symmetry.

Our starting design strategy consists in an array of L-shaped nanostructures, whose two arms have been shown in recent papers to support two independently tunable plasmonic resonances that can be used for polarization control [115,116]. After several rounds of optimization, we converged to the nanostructure shown in Fig. 5.2 (c), consisting of an asymmetric nanocross with the two orthogonal arms connected in such a way to ensure good modal overlap between the resonances at ω and 2ω, yet a strong asymmetry to support large $\chi_{ijk}^{(2)}$. The dimensions of the nanocross optimized for SHG at $1/\lambda=1240$ cm^{-1} are shown in Fig. 5.2 (c) and the results of our full-wave electromagnetic simulations are shown in Fig. 5.3. In particular, Figures 5.3 (a)-(h) show the normalized E_z field component induced in the MQW layer for different FF and SH input light polarizations at normal incidence. The computed fields are normalized to the input (transverse) field amplitude impinging at normal incidence. Significant E_z field is induced in the MQW at both ω and 2ω, up to five times the amplitude of the transverse impinging field.

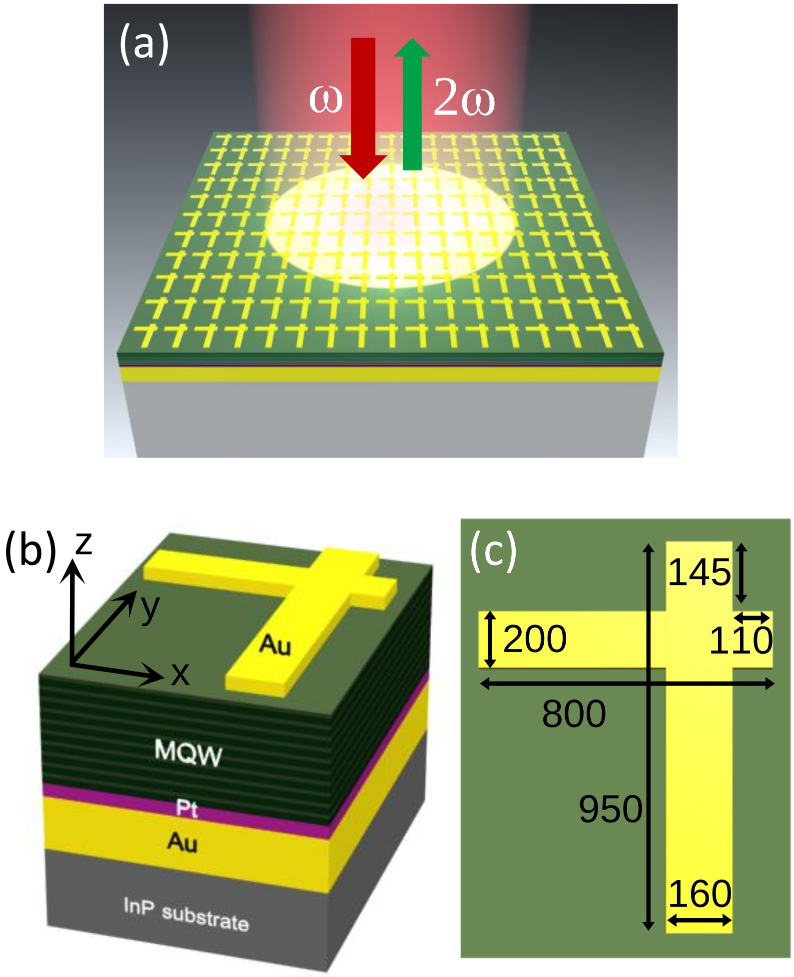

Figure 5.2: Nonlinear metasurface structure. (a) Schematic of the metasurface design and operation. Red and green arrows indicate the incident pump beam at fundamental frequency ω and the reflected second harmonic beam at frequency 2ω, respectively. (b) A 1,000nm × 1,300nm metasurface unit cell and (c) dimensions of the nanocross are given in nm [117].

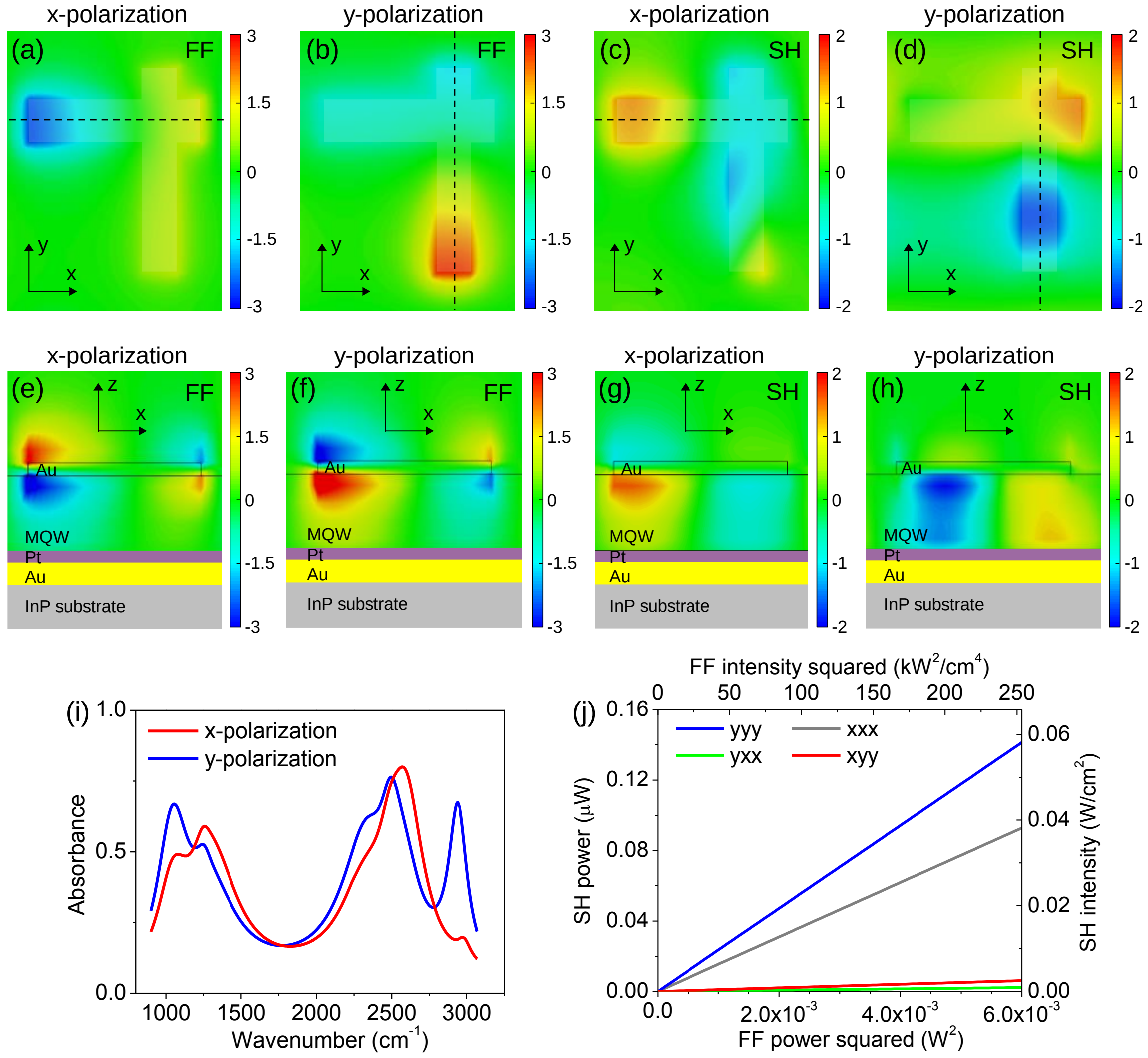

Figure 5.3: Simulations and predicted performance of the optimized metasurface geometry**.** (a)-(d), Top view cross-section of the calculated E_z field enhancement monitored in the MQW layer 100 nm below the gold plasmonic resonators at FF (a, b) and SH frequency (c, d). (e)-(h), Side view cross-section of the calculated E_z field enhancement monitored along the dashed lines shown in panels (a)-(d) at ω (e, f) and 2ω (g, h) for different incident light polarizations. The data is shown for incident light polarized along x-axis and y-axis of the structure. (i), Computed absorption spectrum of the proposed metasurface different input light polarization. (j), SHG power versus FF power for different input/output polarization combinations at FF wavenumber $1/\lambda$=1240 cm^{-1}. FF focal spot is assumed to be of a Gaussian shape with a diameter of $2w$=35 μm [117].

The effective nonlinear susceptibility tensor of the metasurface may be related to these field distributions using Lorentz reciprocity theorem [118], yielding the expression for the general *ijk* tensor element

$$\chi_{ijk}^{(2)eff} = \chi_{zzz}^{(2)} \frac{\int_V E_{z(k)}^{\omega}(x,y,z) E_{z(j)}^{\omega}(x,y,z) E_{z(i)}^{2\omega}(x,y,z) dV}{E_{k(inc)}^{\omega} E_{j(inc)}^{\omega} E_{i(inc)}^{2\omega} V}, \tag{5.8}$$

where $E_{z(i)}^{2\omega}$ is the local E_z field component in the MQW layer induced by *i*-polarized incident wave $E_{i(inc)}^{2\omega}$ at frequency 2ω, i can be x, y, or z, and the integration covers the volume (V) of the MQW layer in the unit cell.

The nonlinear response of the proposed metasurface, summarized by equation (5.8), may be evaluated using the Lorentz reciprocity theorem, under the assumption that saturation effects can be neglected. Essentially, we relate the linear optical response of the metasurface at the fundamental (pump) and second harmonic frequencies to its nonlinear interaction: the Lorentz reciprocity theorem states that if the current density $\mathbf{J}_1$ at point $\mathbf{r}_1$ produces an electric field $\mathbf{E}_1$ at point $\mathbf{r}_2$, then by switching the position of source and observation, their product remains constant, i.e.,

$$\int_V J_1 \cdot E_2 dV = \int_V E_1 \cdot J_2 dV. \tag{5.9}$$

In our case, the electric field $E_z^{\omega}(x,y,z)$ induced at the fundamental frequency in the MQW layer produces an equivalent current density distribution at the SH frequency given by

$$J^{2\omega}(x,y,z) = j2\omega P^{2\omega}(x,y,z) = j2\omega\varepsilon_0\chi^{(2)} E_z^{\omega}(x,y,z)^2. \tag{5.10}$$

We can now apply reciprocity considerations at the SH frequency to relate the field distribution $E_z^{2\omega}(x,y,z)$, induced in the metasurface volume by a plane wave impinging at normal incidence, to the radiated field $E_{FF}^{2\omega}$ sustained by the currents $J^{2\omega}(x,y,z)$. The formula yields:

$$\int_{V_{MQW}} J^{2\omega}(x,y,z)E_z^{2\omega}(x,y,z)dV = \int_{V_{FF}} E_{FF}^{2\omega} J_{FF}^{2\omega} dV \quad , \tag{5.11}$$

where $J_{FF}^{2\omega}$ is the current density necessary to sustain the impinging plane wave inducing $E_z^{2\omega}(x,y,z)$ placed in the volume V_{FF}, and V_{MQW} is the volume of the MQW substrate. After simple algebraic manipulations, one can relate the radiated fields to the field distributions in the MQW layer at FF and SH frequencies:

$$E_{FF}^{2\omega} = \frac{j\omega\chi^{(2)}}{c_0 E_{inc}^{2\omega} S_{unit}} \int_{V_{unit}} E_z^{\omega}(x,y,z)^2 E_z^{2\omega}(x,y,z)dV, \tag{5.12}$$

where S_{unit} is the surface area of the unit cell of the periodic metasurface and V_{unit} is the volume of the MQW within the same unit cell. Generalizing this formalism to the arbitrary polarization of impinging and radiated fields, we obtain Eq. (5.8) in the main text for each element of the effective nonlinear tensor $\chi_{ijk}^{(2)eff}$. The SHG conversion efficiency is then calculated from the ratio of the radiated second-harmonic power over the impinging power:

$$SHG_{eff} = \left| \frac{j\omega\chi^{(2)}}{c_0 E_{inc}^{2\omega} E_{inc}^{\omega} S_{unit}} \int_{V_{unit}} E_z^{\omega}(x,y,z)^2 E_z^{2\omega}(x,y,z)dV \right|^2 . \tag{5.13}$$

In the special case in which we can assume that the field distributions are constant inside the MQW layer at both FF and SH frequencies, the SHG efficiency simply becomes $SHG_{eff} = \frac{1}{2}\omega^2\eta_0^3\left(\varepsilon_0\chi^{(2)}\right)^2 f_{2\omega}^2 f_\omega^4 I_\omega L^2$, where η_0 is the impedance of free space, f_ω the field enhancement factor at the FF, $f_{2\omega}$ is the field enhancement at the SH, I_ω is the input intensity and L is the height of the MQW layer, as expected.

From Eq. (5.13) we can obtain the expression for SHG intensity output $I_{2\omega}$ from the metasurface

$$I_{2\omega} = \frac{(2\omega)^2}{8\varepsilon_0 c^3}\left|\hat{e}_{2\omega}\overset{\leftrightarrow}{\chi}^{(2)eff}\hat{e}_\omega\hat{e}_\omega\right|^2 \left(I_\omega\right)^2 L^2, \tag{5.14}$$

where $\hat{e}_{2\omega}$ ($\hat{e}_\omega$) and $I_{2\omega}$ (I_ω) are the polarization unit vector and intensity, respectively, of the SH (FF) beams, L is the MQW thickness and $\overset{\leftrightarrow}{\chi}^{(2)eff}$ is given by Eq. (5.8) which includes local field enhancement at both ω and 2ω. We note that this expression is consistent with the conventional formula to express the SHG in regular nonlinear crystals, assuming that the thickness L is much smaller than the coherence length [19].

Equation (5.8) is a quintessence of the proposed nonlinear metasurface concept: it shows that we can engineer essentially any component of the nonlinear susceptibility tensor of the metasurface and further increase the already giant nonlinear response from intersubband transitions using local field enhancement at ω and 2ω. It also confirms the necessity of inducing a strong modal overlap between the fundamental and SH modes in the nanostructures, for which our metasurface is optimized. This result may be readily generalized to other nonlinear processes of interest. Using Eq. (5.8) and simulated field distributions for the nanocross structure in Fig. 5.4, we obtain that the largest nonlinear susceptibility coefficient for normal light incidence at the input wavenumber 1240 cm^{-1} is $\chi_{yyy}^{(2)eff}$ = 31 nm/V followed by $\chi_{xxx}^{(2)eff}$ = 25 nm/V, $\chi_{xyy}^{(2)eff}$ = 6.5 nm/V, and $\chi_{yxx}^{(2)eff}$ = 3.9 nm/V.

Figure 5.3 (i) shows computed linear absorption spectrum of the metasurface. The calculated SHG conversion efficiency and SHG power vs. fundamental pump power for different input/output polarization combinations is shown in Fig. 5.3 (j). Results are given for *yyy*, *xxx*, *xyy*, and *yxx* polarization combinations, where the first index refers to the polarization of the SH beam, while the last two indices refer to the polarization of the FF beam.

5.2.3 Device Fabrication and Measurement Setup

For proof-of-concept demonstration, a 400-nm-thick MQW layer was transferred onto a metal ground plane and a 400 μm by 400 μm two-dimensional array of nanocrosses was fabricated on top of the MQW layer to produce the structure shown in Fig. 5.2 (a). A 577 nm-thick MQW layer composed of 28 repetitions of the structure in Fig. 5.1 (a) was grown by the molecular beam epitaxy on a semi-insulating InP substrate. The layer was then transferred to another gold-coated semi-insulating InP substrate via thermo-compression bonding and thinned down to approximately 400 nm thickness by chemical etching. A 400μm by 400μm two-dimensional array of plasmonic nanoresonators was patterned onto the top of the MQW layer via e-beam lithography, metal evaporation, and lift-off. To accommodate the uncertainty in material parameters and fabrication errors, we fabricated several arrays with nanocross dimensions slightly varying around the optimal theoretical parameters shown in Fig. 5.2 (c). The description below focuses on the measured array with highest SHG generation efficiency at 1240 cm^{-1}, but we stress that the measured nonlinear response is quite robust to small changes in the design parameters, as several of our realized metasurface samples showed a similarly large nonlinear response. Yet, we verified that metasurfaces with plasmonic resonances significantly detuned from the intersubband transition frequencies of the MQW structure produced, as expected, little or no nonlinear response. Over the course of our experimental work, we have fabricated a number of metasurfaces in which plasmonic resonances happened to occur away from the intersubband $\left|\chi_{zzz}^{(2)}\right|$ peak, and those structures produced little or no detectable SHG response. An example of such a metasurface is shown in Fig. 5.7. These measurements confirm that the giant nonlinear effects observed in our optimized structures stem from the unique combination of quantum engineering of the nonlinear response coming from the MQW intersubband transition and the electromagnetic resonance engineering of the coupled metasurface. This confirms the unique property of the proposed metasurface, combining quantum and electromagnetic engineering of its nonlinear response.

Figure 5.4 shows a scanning electron microscope (SEM) image of the nanocross array (Fig. 5.4 (a)) and a side view of the cleaved facet with MQW layer metal-bonded to InP substrate (Fig. 5.4 (b)). The absorption reflection spectra of the metasurface for *x*- and *y*-polarized input light at normal incidence are shown in Fig. 5.4 (c). The experimental peaks shapes and positions are in good agreement with the simulated spectrum in Fig. 5.3 (i).

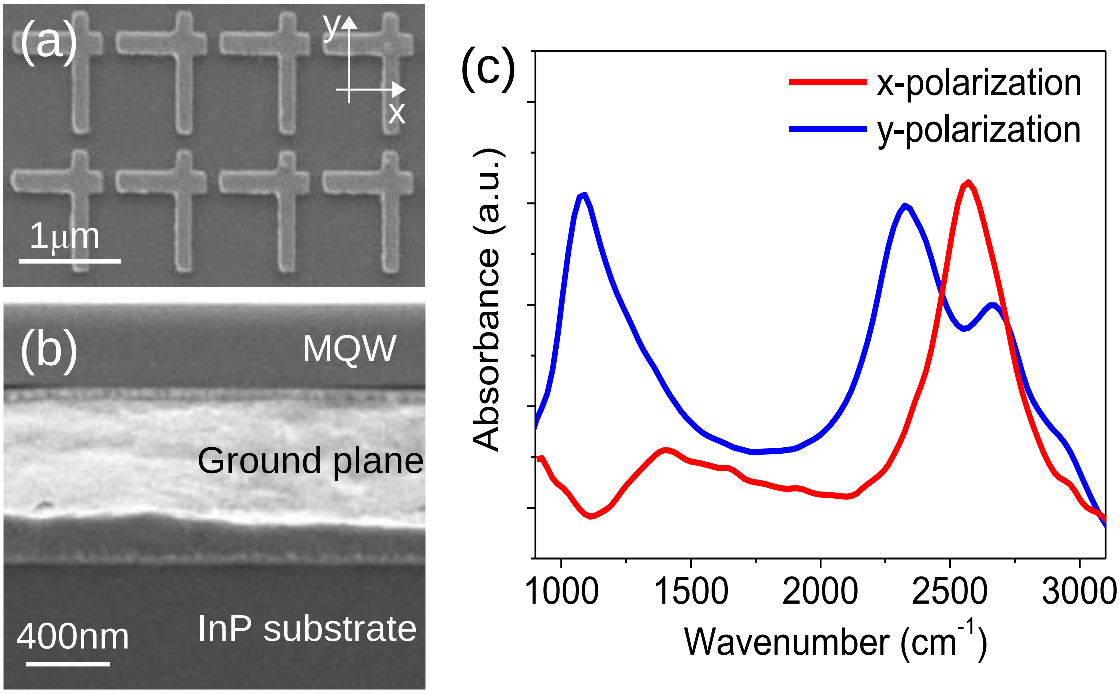

Figure 5.4: Fabricated metasurface structure and absorption spectrum. (a, b) Scanning electron microscope images of the fabricated metasurface top (a) and side (b) view. (c) Absorption reflection spectrum of the fabricated metasurface for normally-incident light polarized along x-axis and y-axis of nanocrosses as shown in (a) [117].

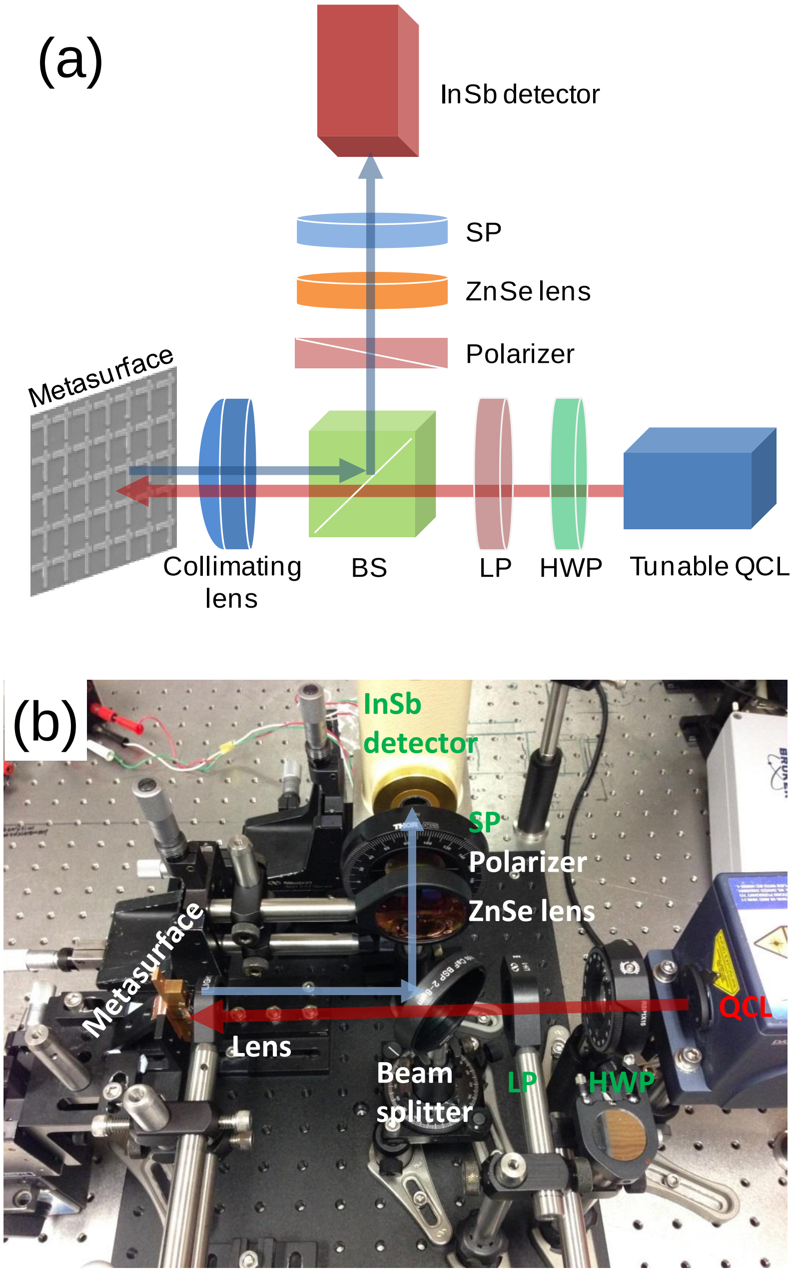

Figure 5.5: (a) Schematic of optical setup for metasurface characterization. (b) Photo-image of optical setup. Linearly-polarized light from a tunable QCL passes through achromatic half-wave plate (HWP) for polarization control, a long pass filter (LP) to remove SHG light coming from the laser, a non-polarizing achromatic 50/50 beam splitter, and a numerical aperture 0.5 collimating lens to the sample. SHG output is collected by the same lens and is directed by the beam splitter towards the detector through a polarizer, a ZnSe lens, and a short pass filter (SP) that is used to block FF.

SHG measurements of the metasurface were performed using the setup shown in Fig. 5.5 and described in the caption. Nonlinear properties of the metasurface were probed by a pulsed broadly-tunable QCL (Daylight Solutions, Inc.; tuning range 1120-1450cm^{-1} and the peak power output of 800 mW). The laser was operated with 400 ns long pulses at 250 kHz repetition frequency. We assume Gaussian beam shape on the metasurface with intensity distribution for FF given as $I_{FF}e^{-2r^2/w^2}$ and that for SH frequency as $I_{SH}e^{-4r^2/w^2}$. The FF focal spot diameter was measured by the knife-edge technique to be $2w$=35 μm. A calibrated InSb detector was used to measure SHG power output and perform spectroscopic measurements at SHG frequencies. SHG power output was corrected for the beam splitter reflectivity (47.5%) and transmission of the collimating lens (95%), the polarizer (82%), the ZnSe lens (97%), and the shortpass filter (83.5%) in the setup. A calibrated thermopile detector was used to determine the power of the fundamental beam at the sample position. The values of $\overleftrightarrow{\chi}^{(2)eff}$ tensor elements were deduced using the $I_{2\omega}$ expression, based on the experimentally-measured values of $I_{2\omega}$ and I_{ω}.

5.2.4 Experimental Results

SHG peak power as a function of the squared FF peak power and peak intensity is plotted in Fig. 5.6 (a) for different input/output polarization combinations. The highest SHG generation efficiency is achieved for *yyy* polarization combination, followed by *xxx*, *yxx*, and *xyy* polarization combinations, in agreement with the theoretical predictions shown in Fig. 5.3 (j).

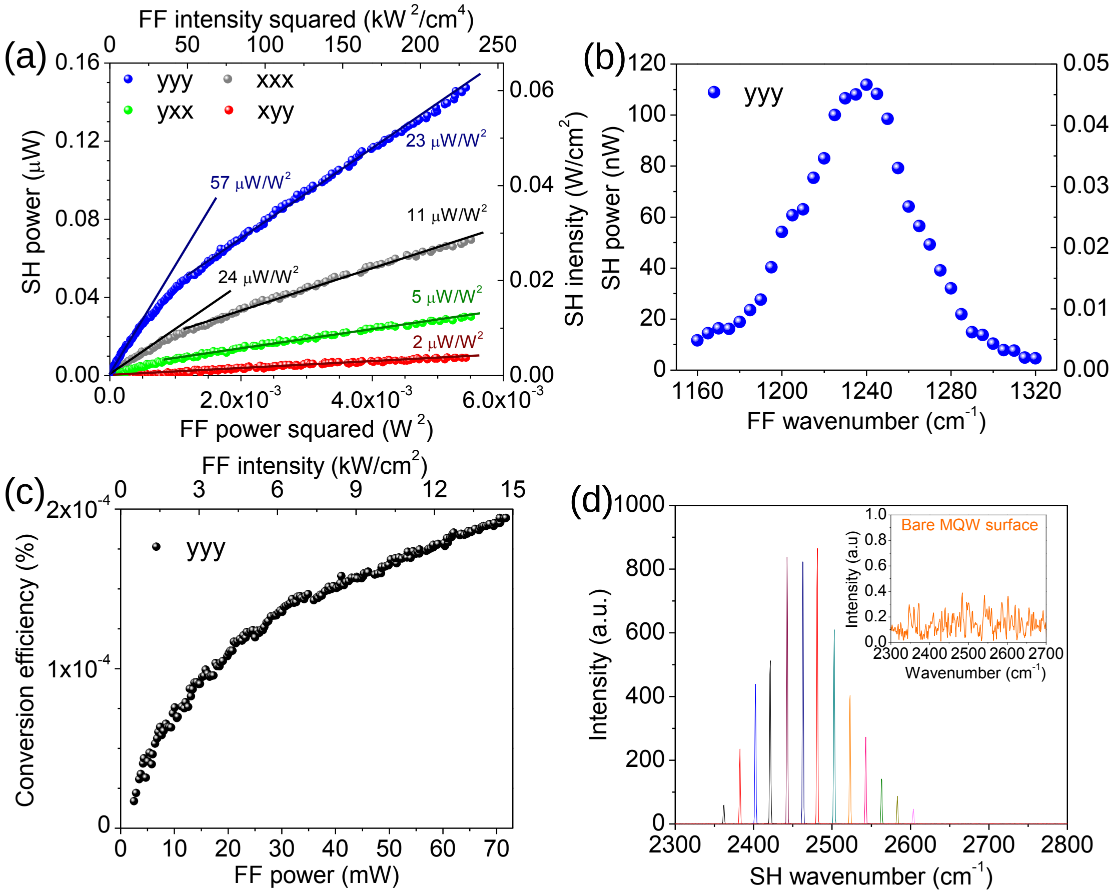

Figure 5.6: Nonlinear response from the metasurface. (a), SH peak power output as a function of FF peak power squared (bottom axis) or peak intensity squared (top axis) at FF wavenumber of 1240cm^{-1} for different input/output polarization combinations. (b), SH peak power (right axis) and peak intensity (left axis) as a function of FF wavenumber for *yyy* polarization combination. FF peak power was fixed at 30 mW for the measurements. (c), SHG power conversion efficiency as a function of FF peak power (bottom axis) or peak intensity (top axis) at FF wavenumber of 1240 cm^{-1} for *yyy* polarization combination. (d), Spectra of SH output for different pump wavenumbers. Inset: no SH emission is observable for bare MQW surface with no nanostructures on it. Measurements in a-d are performed at normal FF incidence/normal SH reflection [117].

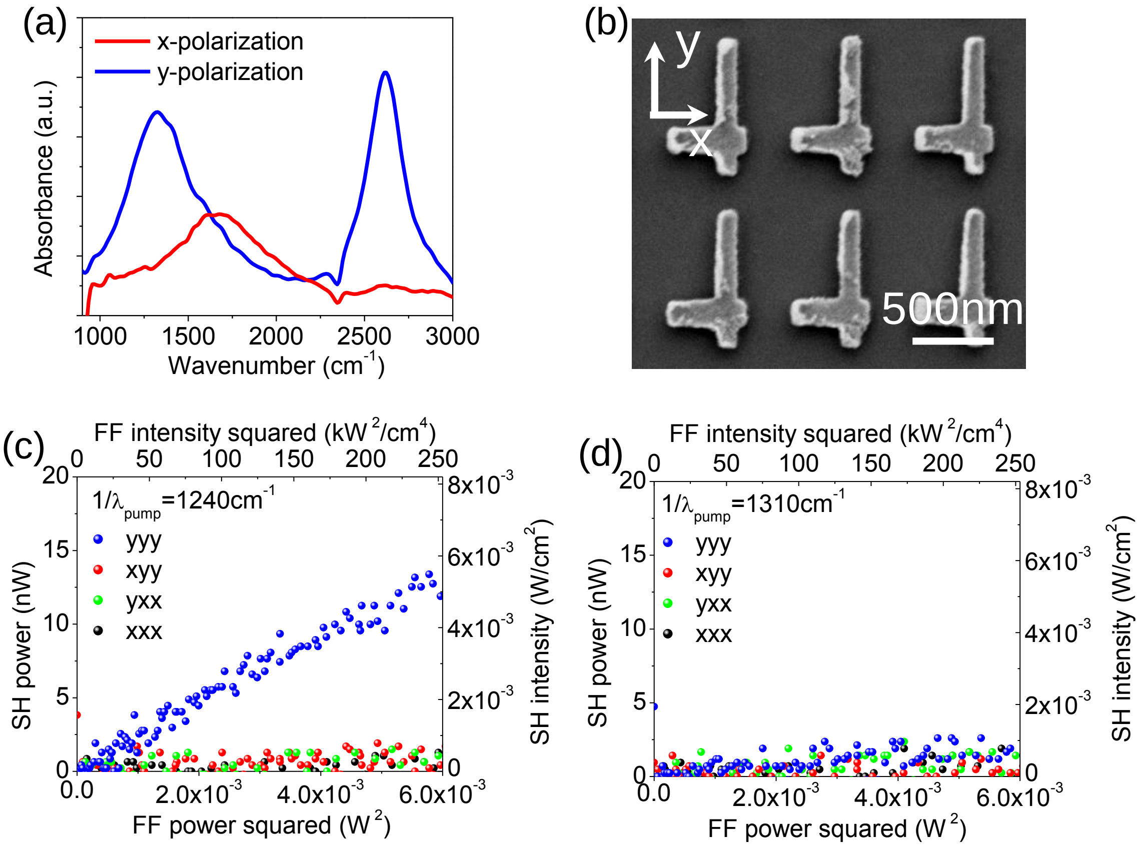

Figure 5.7: Structures with plasmonic resonances detuned from intersubband transition frequencies. (a), Linear absorption spectrum of a metasurface in which plasmonic resonances were not well-overlapped spectrally with intersubband transitions of the MQW structure for fundamental and SH frequencies. (b), SEM image of the metasurface. (c), SH peak power output as a function of FF peak power squared (bottom axis) or peak intensity squared (top axis) for different input/output polarization combinations at FF wavenumber of 1310 cm^{-1} and SH wavenumber of 2620 cm^{-1} both in resonance with the plasmonic absorption peaks. SH response was close to the noise limit of our setup. (d), SH peak power output as a function of FF peak power squared (bottom axis) or peak intensity squared (top axis) for different input/output polarization combinations at FF wavenumber of 1240 cm^{-1} and SHG wavenumber of 2480 cm^{-1}, both away from plasmonic resonances of the metasurface but in resonance with intersubband transitions in the MQW structure [117].

From Eq. (5.8) one expects to observe a linear dependence of SH power on the square of FF power in Fig. 5.6 (a). However, as indicated in the figure, the slope of the curve changes, e.g., for *yyy* polarization combination, from 57 μW/W^2 for low FF powers to 23 μW/W^2 for higher FF powers. We attribute this effect to intensity saturation of intersubband transitions[119] in our MQW structures. Saturation intensity for our MQW structure can be estimated with the expression from Ref. [119]

$$I_{sat} = \frac{cn\varepsilon_0\hbar^2}{e^2 z_{12}^2 \tau g\left(\nu\right)}, \tag{5.15}$$

$$g(\nu) = 2\hbar \frac{\gamma_{12}}{(h\nu - E_{21})^2 + \gamma_{21}^2}, \tag{5.16}$$

where n≈3.2 is the refractive index of MQW, τ is the state 2 lifetime computed to be 1.7 ps and g(ν) is the normalized Lorentzian lineshape function. Substituting measured $2\hbar\gamma_{21} \approx 15\ meV$ and computed z_{12}=1.7 nm into Eq. (5.15) we obtain I_{sat}=0.47 MW/cm^2 for resonant excitation of 1-2 transition.

To confirm that the observed saturation of SHG conversion efficiency is not due to thermal effects, SHG measurements were repeated using 60 ns light pulses. Fig. 5.8 (a) compares the results of these measurements with that obtained using 400 ns current pulses as reported in the paper and shows that results are in nearly-perfect agreement, which excludes thermal effects in observed SHG response.

If we detune the pump frequency, moving away from the design frequency at which intersubband absorption and plasmonic metasurface resonance take place, and therefore reducing the field intensity in the multi-quantum well substrate, the saturation is significantly reduced, as shown in Fig. 5.8 (b).

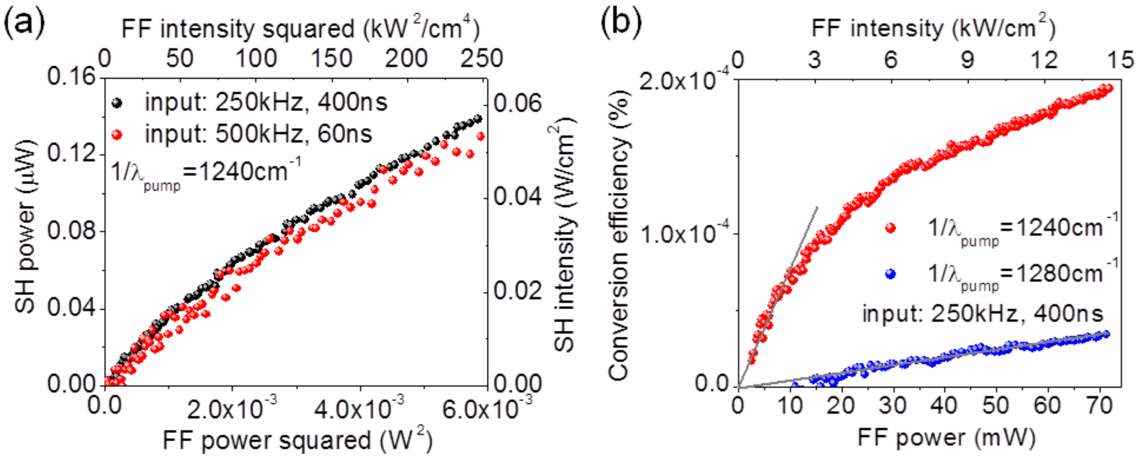

Figure 5.8: Nonlinear response saturation mechanism. (a), SH peak power output as a function of FF peak power squared (bottom axis) or peak intensity squared (top axis) at FF wavenumber of 1240cm^{-1}. Black curve is the data for pump laser operating with 400 ns pulses (same as used in the manuscript), red curve is the data for the pump laser operating with 60 ns pulses. Slight difference in the SHG power for 60 ns and 400 ns FF input is attributed to slight changes in the pulse shape and detector response for 400 ns and 60 ns pulses. (b), SH conversion efficiency vs FF peak power (bottom axis) or peak intensity (top axis) for FF wavenumber of 1240cm^{-1} (red) and 1280cm^{-1} (blue) [117].

Calculations above indicate that saturation intensity[119] for state 1 to state 2 transition in our structures is approximately 0.47 MW/cm^2 and simulation results in Fig. 5.3 indeed indicate local intensities approaching saturation intensity in the hot spots of the MQW structure for input pump intensities above 10 kW/cm^2. We note that our proof-of-concept metasurface design is far from perfect, as one ideally wants to create a more uniform local field enhancement within the MQW structure at both FF and SH frequencies with maximal modal overlap integrals, consistent with Eq. (5.8). This implies that even larger nonlinear response may be found with better optimized nanoresonator designs, exploiting the field localization properties of plasmonic structures. Still, the measured results presented here unveil an enormous potential for the proposed metasurface, achieved by combining plasmonic resonances and intersubband transitions.

To better understand the potential improvement associated with nanoresonator optimization one may consider an ideal metasurface in which the nanoresonators are able to induce a uniform E_z field enhanced 3 times compared to the impinging field across the entire MQW layer at both SH and FF. In this case, Eq. (5.8) predicts $\chi^{(2)eff} = 27\chi^{(2)}_{zzz}$, approximately 50 times larger than the largest $\chi^{(2)eff}$ coefficients computed for the nanocross design used in this work. Since the SHG power scales with $\left|\chi^{(2)eff}\right|^2$, such a metasurface would produce over three orders of magnitude improvement in SHG conversion efficiency compared to our current experiment. Furthermore, since the field enhancement is limited to a factor of 3, no significant intensity saturation is expected for the pump intensities used in our experiment. Improvements may also be achieved by exploring the quantum-engineering design space of our structures. The simple doubly-resonant quantum well heterostructure used here for this initial proof-of-concept demonstration is by no means the most optimal design, and more sophisticated designs may be devised to achieve both higher nonlinearity and much larger saturation intensity, similar to those described in Refs. [24,113].

Our MQW structure and plasmonic nanocrosses were designed to provide maximum SHG efficiency at pump wavenumber $1/\lambda \approx 1240$ cm^{-1}. This is experimentally confirmed in Fig. 5.6 (b) where we record SHG power output as a function of pump frequency while keeping the pump power constant. The *yyy* SHG power conversion efficiency for FF wavenumber of 1240 cm^{-1} is shown in Fig. 5.6 (c). We achieve almost 2×10^{-6} power conversion efficiency using pump intensity of only 15 kW/cm^2. In comparison, previously demonstrated nonlinear optical metasurfaces at infrared or visible frequencies required high-peak-power fs lasers providing over 10^8 W/cm^2 FF intensity to produce 10^{-10}-10^{-11} SHG power conversion efficiency [100-103]. Assuming identical pumping intensity, our metasurfaces achieves over 8 orders of magnitude enhancement in conversion efficiency over the current state-of-the-art.

Experimental values of $\chi_{ijk}^{(2)eff}$ are obtained using the intensity data for SH and FF beams in Fig. 5.6. We obtain $\chi_{yyy}^{(2)eff} \approx$ 55 nm/V (35 nm/V) and $\chi_{xxx}^{(2)eff} \approx$ 36 nm/V (24 nm/V) for low FF intensity (high FF intensity) in Fig. 5.6 (a). The other two coefficients have no significant dependence on pump intensity in the experiment: $\chi_{yxx}^{(2)eff} \approx$ 16 nm/V and $\chi_{xyy}^{(2)eff} =$ 10 nm/V. All these quantities are in good agreement with our theoretical predictions, given uncertainties in material parameters and $\chi_{zzz}^{(2)}$. Finally, Fig. 5.6 (d) shows SHG emission spectra from the metasurface for different FF. The MQW structure without patterned nanostructures does not produce any significant nonlinear response for normal incidence, as shown in the figure inset.

The nonlinear metasurface described above can also operate as SHG mirror at oblique incidence angles. This is because enhanced wave-matter interaction arises at the short scale, supported by the inclusion resonances, rather than based on a collective effect. Fig. 5.9 (a) and (b) show details of SHG power output measurements at 45-degree angle of incidence pumping. Nonlinear response that was comparable to that reported for normal incidence in Fig. 5.6 (a) was observed for SSS, PPP, SPP, and PSS polarization combinations, as shown in Fig. 5.9 (b). In our notation, the first of three letters in the polarization combination refers to the polarization of SHG wave and the last two letters refer to the polarization of the input fundamental frequency with E-field directions for S and P polarizations shown in Fig. 5.9 (a).

For a control experiment, we used a bare MQW structure without plasmonic nanostructures, which produced no detectable SHG response in this configuration for all polarization combinations. We note that in principle one expects to have some nonlinear

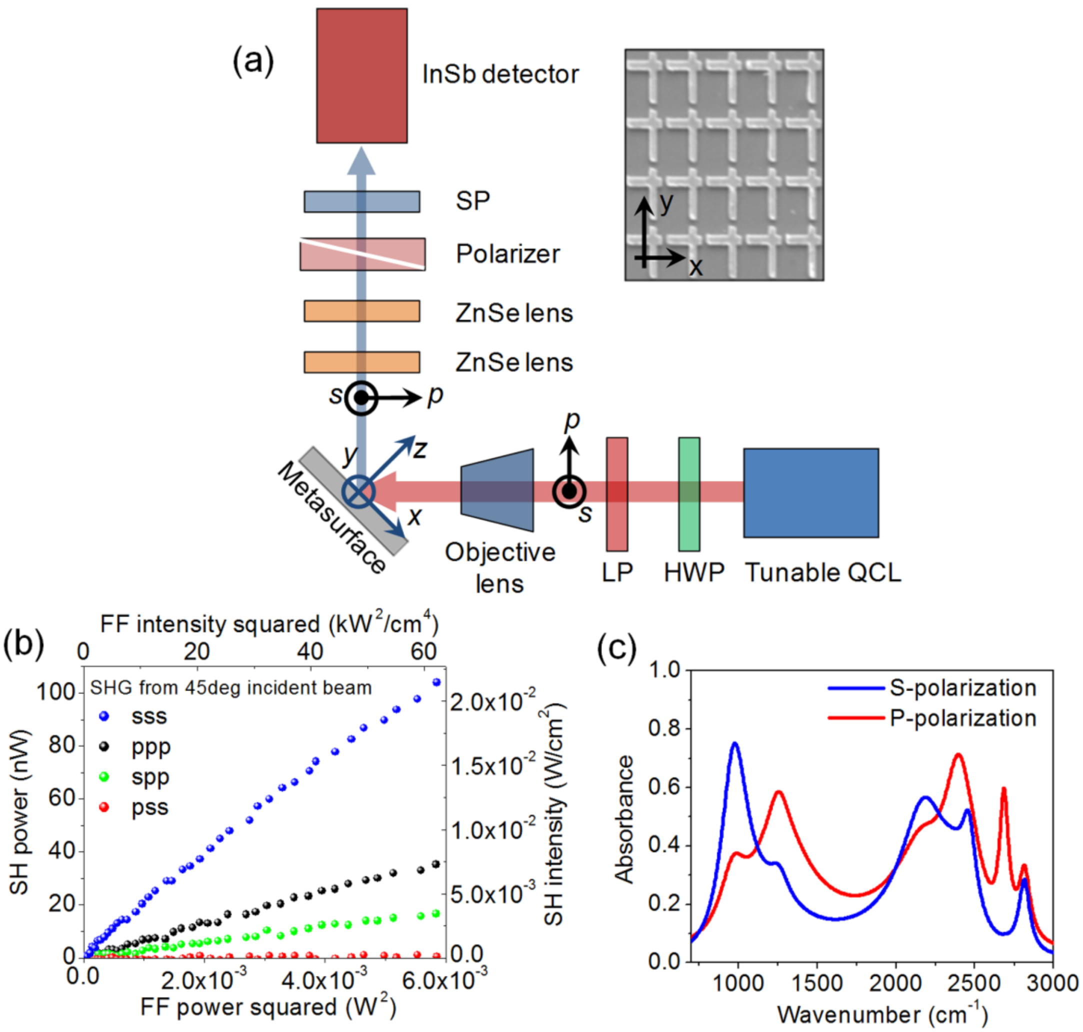

Figure 5.9: SHG measurement at oblique incidence. (a), Optical setup for metasurface characterization at 45-degree incidence angle. LP and SP are long and short-pulse filters, respectively. HWP is a half-wave plate for QCL polarization control. Directions of S and P-polarizations and orientation of the metasurface are indicated. Inset: SEM image of the metasurface with x- and y-axes shown. (b), Measured SH peak power output as a function of FF peak power squared (bottom axis) or peak intensity squared (top axis) at FF wavenumber of 1240 cm^{-1} for different input/output polarization combinations. (c), Simulated absorption spectrum of the metasurface at 45-degree incidence for different input light polarizations [117].

response for PPP polarization combination from bare MQW structures in this experimental configuration due to the presence of intersubband $\chi_{zzz}^{(2)}$. However, due to the insufficient thickness of the sample and small value of E_z field inside the MQW material this ‘intrinsic’ intersubband response was below our detection limit.

Figure 5.9 (c) shows the simulated absorption of our metasurface at 45-degree incidence for S and P light polarizations. We note that the absorption peak positions are not significantly affected by the change in excitation, due to the local response of the metasurface inclusions. This is ideal to use the nonlinear mirror in reflection mode without constraints on the incidence and observation angle.

Our proof-of-concept experiment may be extended to create voltage-tunable [20] and active electrically pumped nonlinear metasurfaces [94-96], and to spectrally and spatially engineer the nonlinear optical response in more arbitrary ways, to name a few possibilities. The metasurfaces with giant nonlinear optical response presented here may serve as the foundation for a flat nonlinear optics paradigm, in which efficient frequency mixing may occur over deeply sub-wavelength films with significantly relaxed phase-matching conditions, compared to bulk nonlinear crystals, that only require matching of wave vector components parallel to the surface. Such ultrathin nonlinear materials may dramatically simplify wave mixing experiments in a variety of setups, finding applications for frequency up- and down-conversion, mixing, phase conjugation, all-optical control and tunability, as well as photon pair generation over a surface for quantum information processing.

5.3 SECOND METASURFACE DESIGN AND EXPERIMENT

5.3.1 MQW Design and Optical Properties

The first MQW design for SHG is based on doubly-resonant electron subbands in which the transition energy between electron subband 1 to 3 is twice for that between electron subbband 1 to 2 and 2 to 3 (see Fig. 5.1 (a)). In this configuration, the absorption loss from intersubband transitions is maximized at which the nonlinear susceptibility is maximized. Since the nonlinear susceptibility is determined by both intersubband transitions between electron subband 1 to 2 and 2 to 3 and also average doping density as given in Eq. (5.6), one may be able to design the MQW having higher nonlinear susceptibility and lower absorption loss at a designed wavelength. Our second approach in MQW design is using higher average doping and off-resonant intersubband transitions to make the nonlinear susceptibility larger and the absorption loss lower at a same time. Also in this design, saturation intensity of the intersubband transitions becomes higher than the first MQW design.

Figure 5.10 (a) shows the band diagram of a $In_{0.53}Ga_{0.47}As/Al_{0.52}In_{0.48}As$ coupled quantum well structure, repeated multiple times to produce the 400-nm-thick MQW layer used in our experiments. Figure 5.10 (b) shows the experimentally-measured intersubband absorption spectrum after background correction. The spectrum is obtained in a multipass geometry using the original InP wafer with the MQW layer on top as described above. The wafer was polished to have facets at 45 degrees to surface normal and its top and bottom surfaces were gold-coated. The two resonant peaks are well matched with designed intersubband transitions shown in Fig. 5.2 (a). From Fig. 5.2 (b), we obtain transition $\hbar\omega_{21} \approx 154 meV$ and $\hbar\omega_{31} \approx 252 meV$ in excellent agreement with calculated values of 154 meV and 254 meV, respectively, as shown in Fig. 5.2 (a). The measured transition linewidths are $2\hbar\gamma_{21} \approx 22 meV$, $2\hbar\gamma_{31} \approx 25 meV$ and the peak

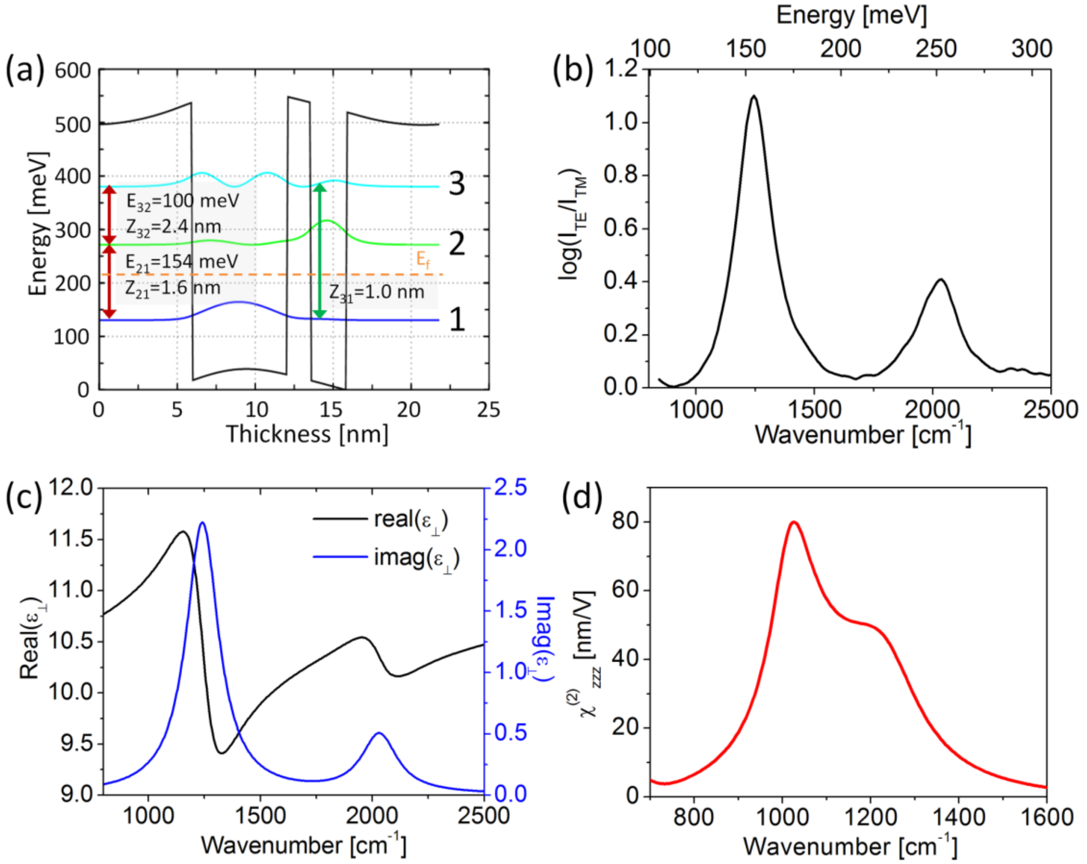

Figure 5.10: 2nd design of multi-quantum well structure and optical parameters. (a) Conduction band diagram of one period of an $In_{0.53}Ga_{0.47}As/Al_{0.52}In_{0.48}As$ coupled quantum well structure designed for giant nonlinear response for SHG. The layer sequence (in nm) is **6.0**/6.1/**1.5**/2.3/**6.0**, where AlInAs barriers are shown in bold, and the first 5nm of the first 6nm barrier and the last 5nm of the last 6nm barrier are n-doped to 1.5×10^{18}cm^{-3}. (b) Intersubband absorption spectrum of the 2nd design MQW wafer used in experiment after background correction. (c) Real and imaginary part of dielectric constant for out-of-plane (ε⊥) electric field. (d) Intersubband nonlinear susceptibility of the structure in (a) as a function of pump frequency for SHG.

absorption α_W =5369 cm^{-1} and 2007 cm^{-1} for 2-1 transition and 3-1 transition, respectively. The values of intersubband absorption α_W then allow us to estimate the actual doping level as $N_e \approx 1.15 \times 10^{18}\ cm^{-3}$. By using these parameters and Eq. (5.4), the dielectric constant for out-of-plane electric field is calculated and plotted in Fig. 5.10 (c). Figure 5.10 (d) plots the absolute value of the SHG nonlinear susceptibility tensor element $\chi_{zzz}^{(2)}$ as a function of pump frequency calculated for this structure. The nonlinear response peaks at approximately 80 nm/V, nearly 2 times larger than that of the first MQW structure. Saturation intensity for the 2nd MQW structure can be estimated with the Eq. (5.15) and (5.16). Substituting the measured $2\hbar\gamma_{21} \approx 22\ meV$ and computed z_{12}=1.6 nm into Eq. (5.15) we obtain I_{sat}=1.25 MW/cm^2 for resonant excitation of 1-2 transition. This saturation intensity is nearly 3 times larger than that of the first MQW design and the effect of output intensity saturation may be more relaxed than the first MQW structure.

5.3.2 Metasurface Design and Simulations

Nanocross array

The second design of MQW layer is then sandwiched between a metal ground plane and a patterned array of metallic nanocrosses, as shown in Fig. 5.11 (a). The new structure is similar to the structure of the first proof-of-concept demonstration metasurface. Figure 5.11 (b)-(e) show the normalized E_z field component induced in the MQW layer for different FF and SH input light polarized along *x*-axis at normal incidence. The computed fields are normalized to the input field amplitude impinging at normal incidence. Significant E_z field is induced in the MQW at both ω and 2ω, up to 3.4 times the amplitude of the transverse impinging field. For now, the FF wavelength of the input beam is 9.7μm and SH wavelength of the output beam is 4.85μm. The nanocross

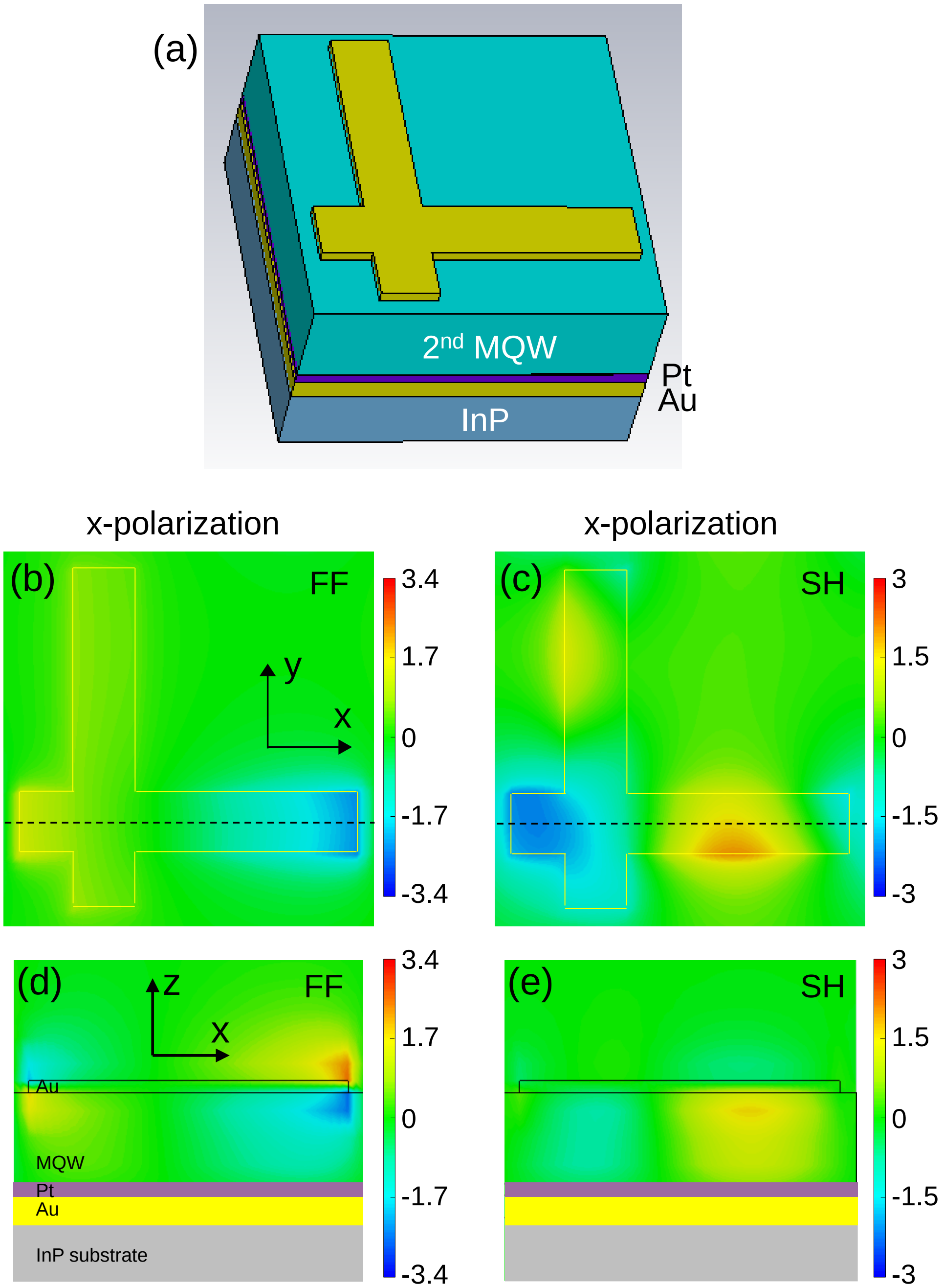

Figure 5.11: Simulations of metasurfaces with nanocross array. (a), Metasurface unit cell structure used for the simulation. (b, c), Top view cross-section of the calculated E_z field enhancement monitored in the MQW layer 100nm below the gold plasmonic resonantors at FF (b) and SH (c) for *x*-polarized impinging field. (d, e), Side view cross-section of the calculated E_z field enhancement monitored along the dashed lines shown in (b) and (c).

dimensions are adjusted to have absorption peaks for the new input (FF) and output (SH) wavelengths. Since the structure is similar to the proof-of-principle device, improvement of the SH output signal mostly comes from the higher nonlinear susceptibility. Using Eq. (5.8), the effective second-order nonlinear susceptibility out of 80nm/V of nonlinear susceptibility of the MQW layer was calculated to be 45nm/V. From the effective nonlinear susceptibility calculation, we can expect the SH output signal will be about 2 times higher than that from the proof-of-concept metasurface.

T-shape nanoresonator array

The asymmetric nanocross array can re-radiate x- and y-polarized SH output singal out of x- or y-polarized input impinging fields. As a result, the metasurface has several components of the effective second-order nonlinear susceptibility tensor elements. One advantage of this property is that one can design virtually any element of nonlinear susceptibility tensor element. However, this asymmetric nanocross array is not suitable for demonstrating the maximum capacity out of such a structure. In this regards, we designed a different shape of nanoresonator. Our second nanoresonator design strategy consists of an array of ‘T’-shaped nano-structures, as shown in Fig. 5-12 (a). The long arm along the x-axis supports strong plasmonic resonance for the input impinging field polarized along the x-axis at FF and the short arm along the y-axis supports strong plasmonic resonance for the input impinging field polarized along the y-axis at SH. As a result, the ‘T’-shaped nanoresonator array will absorb input impinging field polarized along the *x*-axis at FF and will radiate SH output signal polarized along the *y*-axis. Figure 5.12 (b)-(e) show the normalized E_z field component induced in the MQW layer for different FF and SH input light polarized along *x*- and *y*-axis at normal incidence, respectively. The computed fields are normalized to the input field amplitude impinging at normal

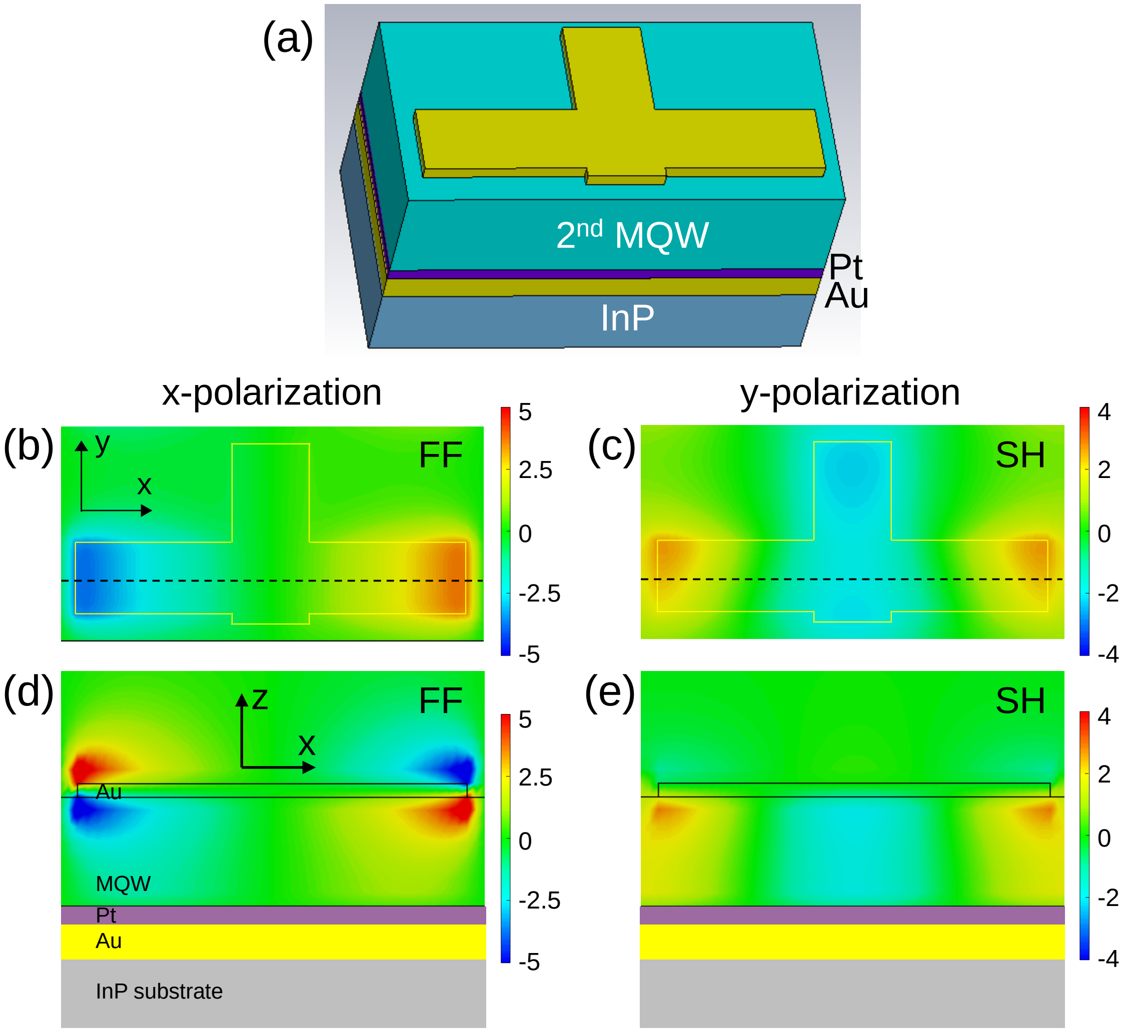

Figure 5.12: Simulations of metasurfaces with ‘T’-shape nanoresonator array**.** (a), Metasurface unit cell structure used for the simulation. (b, c), Top view cross-section of the calculated E_z field enhancement monitored in the MQW layer 100nm below the gold plasmonic resonantors at FF for *x*-polarized impinging field (b) and SH for *y*-polarized impinging field (c). (d, e), Side view cross-section of the calculated E_z field enhancement monitored along the dashed lines shown in (b) and (c).

incidence. Significant E_z field is induced in the MQW at both ω and 2ω, up to 5 times the amplitude of the transverse impinging field. At the two edge portions of the long arm, good field overlap between the induced E_z field for FF and SH is obtained. In this structure, 160nm/V of the effective second-order nonlinear susceptibility is calculated for *yxx* polarization combination.

Etched T-shape nanoresonator array

The ‘T’-shape nanoresonator array shows better efficiency in SHG conversion efficiency and is a possible candidate for the next generation of metasurface design. However, the structure only shows slightly better efficiency than the asymmetric nanocross array. A higher field overlap between E_z^{ω} and $E_z^{2\omega}$ is needed to build more efficient nonlinear metasurface. To get the higher field overlap, higher E_z field enhancement in the entire MQW layer and better field overlaps between fundamental and second-harmonic resonator modes are desired. Z-polarized plasmonic field profiles induced in the MQW layer spread in the x-y plane as away from the top gold nanoresonator and also field enhancement factor drops significantly. As a result, a calculation of the overall field overlap will yield a value of less than 2. The value of the overlap integral is increased significantly, however, when the portion of the MQW layer outside of the nanoresonator is etched away. Figure 5.13 (a) shows example structure using ‘T’-shape nanoresonator with etched MQW layer and Fig. 5.13 (b-e) show the normalized E_z field component induced in the etched MQW layer for different FF and SH input light polarizations at normal incidence. Significant E_z field is induced in the MQW at both ω and 2ω, up to 5 times the amplitude of the transverse impinging field. Using Eq. (5.8), the effective second-order nonlinear susceptibility out of 80nm/V of the MQW nonlinear susceptibility was calculated to be 414nm/V. The giant value of the effective second

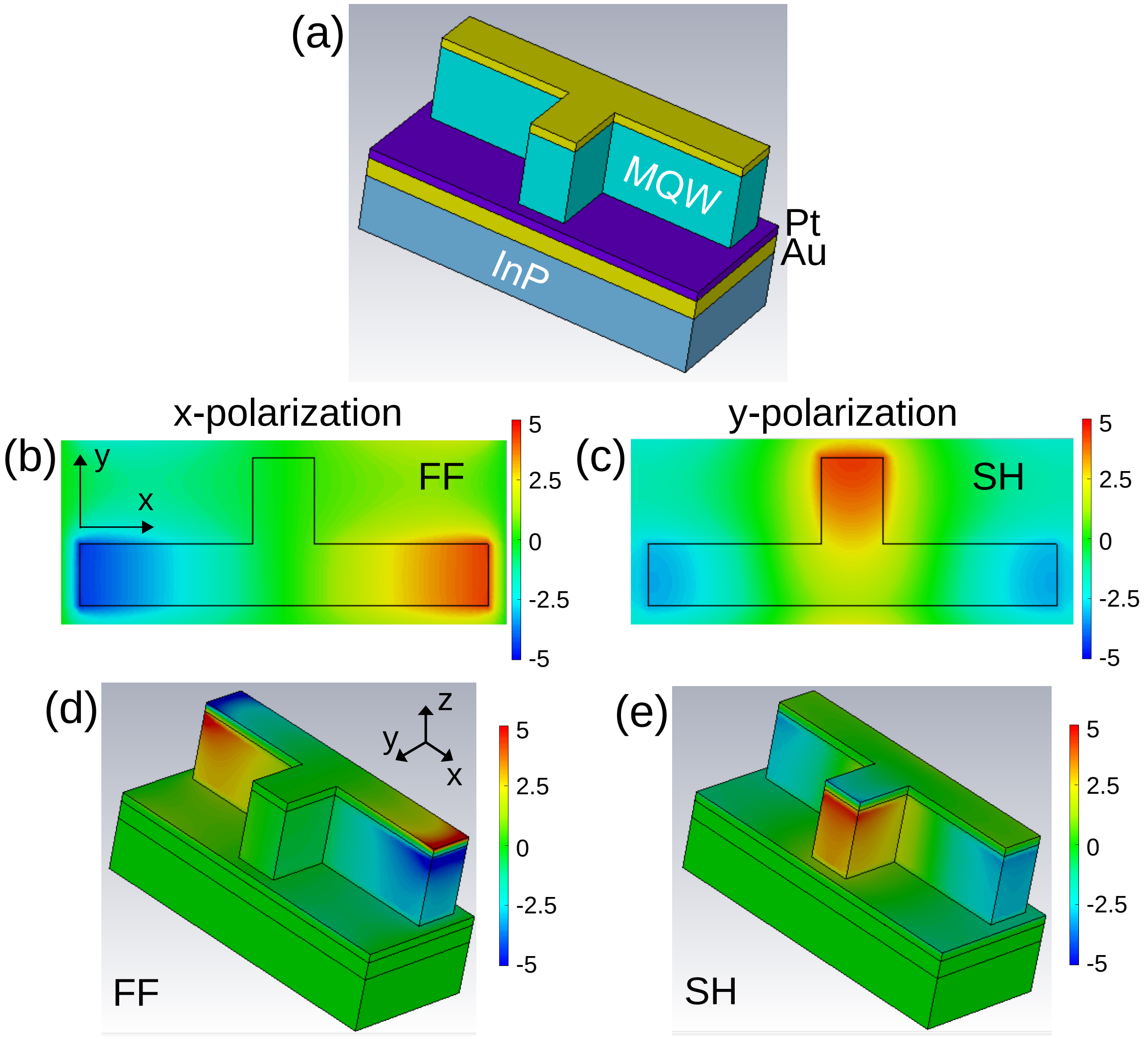

Figure 5.13: Simulations of metasurfaces with etched ‘T’-shape nanoresonator array**.** (a), Metasurface unit cell structure used for the simulation. (b, c), Top view cross-section of the calculated E_z field enhancement monitored in the MQW layer 100nm below the gold plasmonic resonantors at FF for *x*-polarized impinging field (b) and SH for *y*-polarized impinging field (c). (d, e), 3-dimensional view cross-section of the calculated E_z field enhancement for FF and SH frequency.

order nonlinear susceptibility will give a 100 times higher SH output signal from the metasurface than that from the proof-of-concept metasurface.

5.3.3 Device Fabrication and Measurement Setup

For experimental demonstration of the simulated metasurfaces, a 400-nm-thick MQW layer was transferred onto a metal ground plane and a 350 μm by 350 μm two-dimensional arrays of nanoresonators were fabricated on top of the MQW layer. A 400 nm-thick MQW layer composed of 19 repetitions of the structure in Fig. 5.11 (a) was grown by the molecular beam epitaxy on a semi-insulating InP substrate. The layer was then transferred to another gold-coated semi-insulating InP substrate via thermo-compression bonding and thinned down to approximately 400 nm thickness by chemical etching. A 350μm by 350μm two-dimensional array of plasmonic nanoresonators was patterned onto the top of the MQW layer via e-beam lithography, metal evaporation, and lift-off. For the etched ‘T’-shape nanoresonator array, additional 140nm-thick SiO_2 layer as an etch mask layer was evaporated on the top gold layer and lifted-off. To etch the portion of the MQW layer without metal nanoresonator, inductively coupled plasma RIE (Oxford ICP RIE, Cl_2 6sccm, CH4 4sccm, H2 7sccm, Set pressure 4mtorr, Strike pressure 10mtorr, ramp rate 2, RF 75W, ICP 1000W for 4min 30sec) was used. Figure 5.14 shows a top view of SEM image of the asymmetric nanocross array (Fig. 5.14 (a)), ‘T’-shape nanoresonator array (Fig. 5.14 (b)), and etched ‘T’-shape nanoresonator array (Fig. 5.14 (c)). Figure 5.14 (d) shows a 20degree tilted view of the etched ‘T’-shape nanoresonator array. SHG measurements of the metasurfaces were performed using the same setup shown in Fig. 5.5 except different broadly-tunable QCL (Daylight Solution, Inc.; tuning range 900-1190cm^{-1} and 1490-1900cm^{-1}). The laser was operated with 400 ns long pulses at 250 kHz repetition frequency.

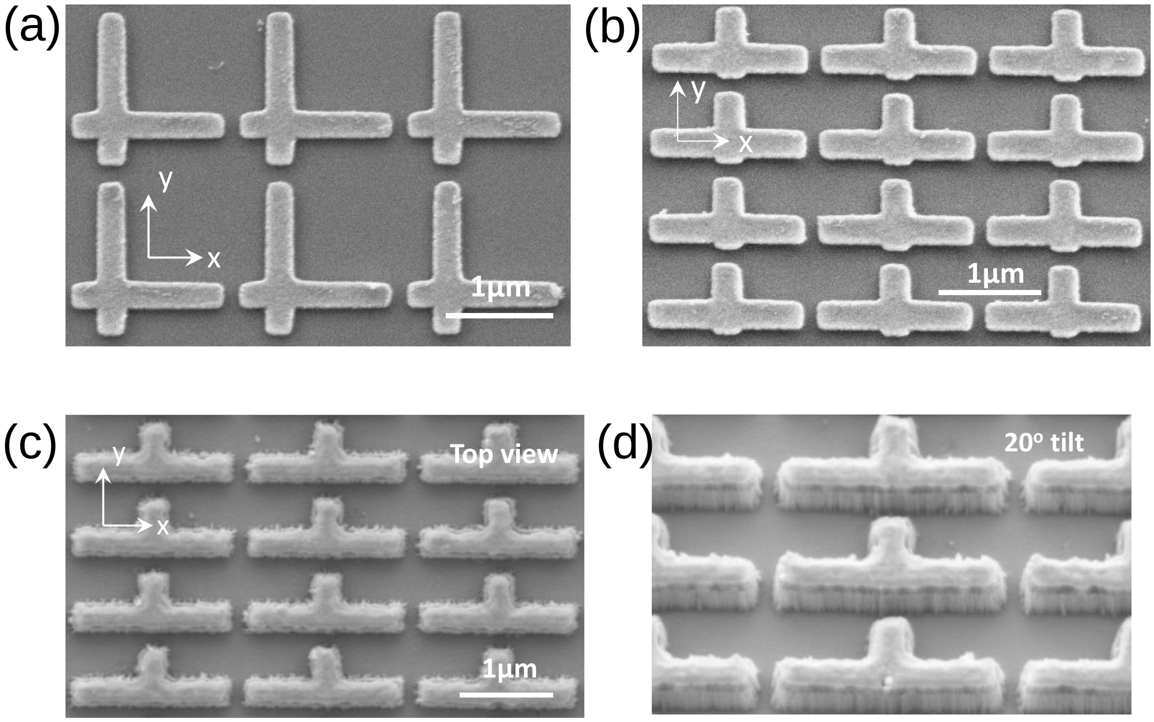

Figure 5.14: Fabricated metasurface structures. (a) Top view of SEM image of the fabricated metasurface with asymmetric nanocross, (b) with 'T'-shape nanoresonator array, (c) etched 'T'-shape nanoresonator array. (d) 20 degree tilted view of the etched 'T'-shape nanoresonator array.

5.3.4 Experimental Results

The proof-of-concept experiment for SHG was successfully done by demonstrating that one can engineer virtually any elements of the effective second order nonlinear susceptibility tensor. 2×10^{-6} of SHG power conversion efficiency with only 15kW/cm^2 was obtained for yyy polarization combinations. Although the metasurface can be operated with low power input beam and the power conversion efficiency is several orders of magnitude higher than the current state-of-the-art technology, the conversion efficiency is still low and far from practical applications. The main strategy of the second round of SHG metasurface experiment is to improve the SH conversion efficiency up to the comparable level of the SHG conversion efficiency based on waveguide geometries. To confirm the simulations and calculations expected from the section 5.3.3., SH powers and power conversion efficiencies for the metasurfaces with different nanoresonators array were measured.

Nanocross array

SHG peak power as a function of the squared FF peak power and peak intensity is plotted in Fig. 5.15 (a) for *x*-polarized input (λ_{FF}=9.66μm)/output (λ_{SH}=4.83μm) light. The highest SHG generation efficiency is achieved for *xxx* polarization combination, in agreement with the theoretical predictions (see section 5.3.2). As indicated in the figure, the slope of the curve changes from 238 μW/W^2 for low FF powers to 172 μW/W^2 for higher FF powers. From the experimental data, we obtain the effective nonlinear susceptibility $\chi_{xxx}^{(2)eff} \approx 112\, nm/V\ (98\, nm/V)$ for low FF intensity (high FF intensity). Compared to the proof-of-concept measurement data, the intensity saturation effect is more relaxed due to the higher saturation intensity of the intersubband transition in the MQW layer. Figure 5.15 (b) shows SH power conversion efficiency data of the metasurfaces with the 1st design of MQW layer and the 2nd design of MQW layer. Nearly an order of magnitude improvement in SH power conversion efficiency was achieved. Since the two nanoresonators are similar in the shape and also in the overlap factor, the SH output improvement mostly comes from the MQW design optimization.

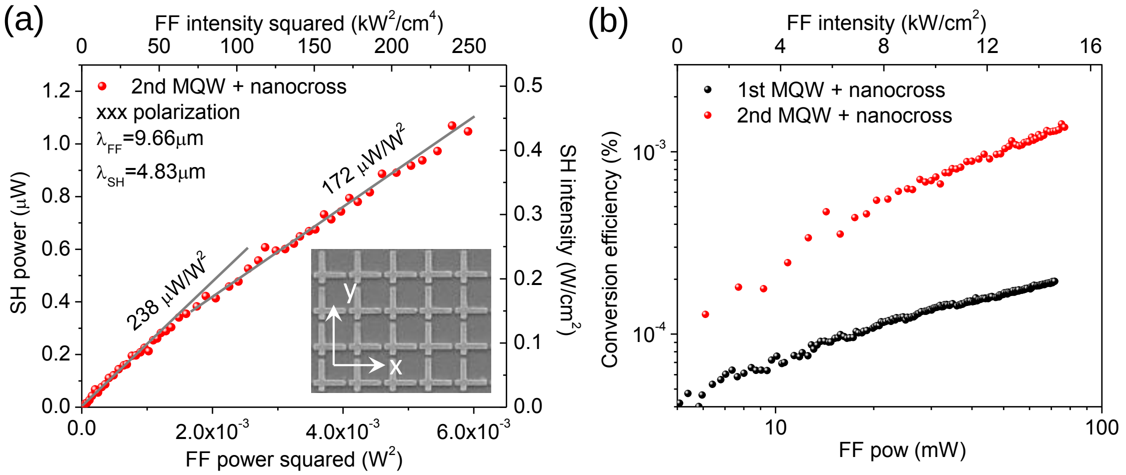

Figure 5.15: Nonlinear response from the metasurface with nanocross resonator array. (a) Measured SH peak power output (left axis) and intensity (right axis) output as a function of FF peak power squared (bottom axis) or peak intensity squared (top axis) at FF wavelength of 9.66μm for *xxx* polarization combinations. Straight lines and labels indicate slopes of SH peak power dependence on FF power squared. (b) SHG power conversion efficiencies as a function of FF peak power (bottom axis) and peak intensity (top axis) at FF wavelength of 9.66μm for *xxx* polarization combinations. The conversion efficiencies from the metasurface with 1st design MQW layer and nanocross array (black dots) and from the metasurface with 2nd design MQW layer and nanocross array (red dots) are shown.

T-shape nanoresonator array

Figure 5.16 (a) shows SHG peak power as a function of the squared FF peak power and peak intensity for *x*-polarized input (λ_{FF}=9.66μm) and *y*-polarized output (λ_{SH}=4.83μm) light. The highest SHG generation efficiency is achieved for *yxx* polarization combination, in agreement with the theoretical predictions (see section 5.3.2). 1.4μW of SH peak power was achieved with 75mW of input pump. As shown in the figure, the slope of the curve changes from 374 μW/W^2 for low FF powers to 195 μW/W^2 for higher FF powers. As seen from simulation, since higher field enhancement than that in the nanocross array is induced at the edge of the long arm, the slope of the curve changes more significantly than the nanocross array. From the experimental data, we obtain the effective nonlinear susceptibility $\chi_{xxx}^{(2)eff} \approx 140nm/V\ (109nm/V)$ for low FF intensity (high FF intensity). Figure 5.16 (b) shows SH power conversion efficiency data of the metasurfaces with the 1st design of MQW layer and the 2nd design of MQW layer. Over an order of magnitude improvement in SH power conversion efficiency was achieved.

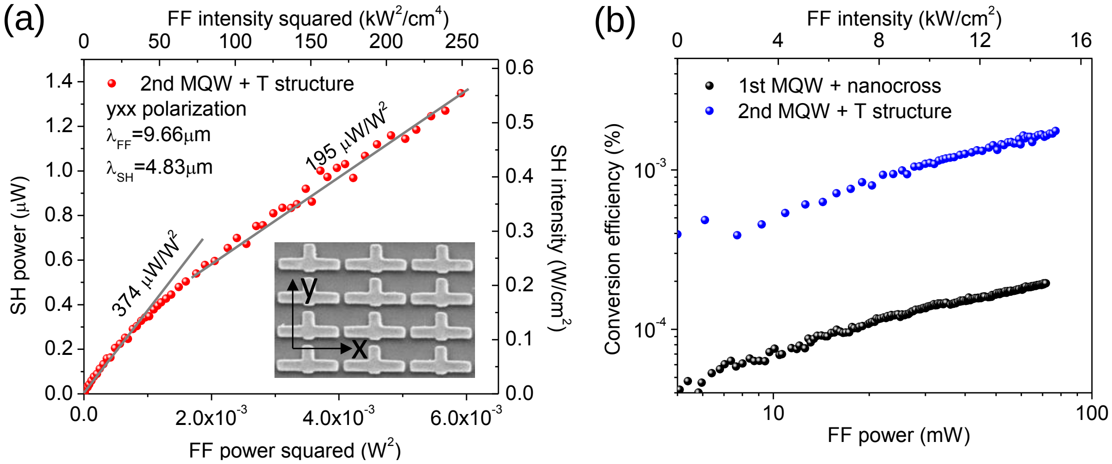

Figure 5.16: Nonlinear response from the metasurface with T-shape resonator array. (a) Measured SH peak power output (left axis) and intensity (right axis) output as a function of FF peak power squared (bottom axis) or peak intensity squared (top axis) at FF wavelength of 9.66μm for *yxx* polarization combinations. Straight lines and labels indicate slopes of SH peak power dependence on FF power squared. (b) SHG power conversion efficiencies as a function of FF peak power (bottom axis) and peak intensity (top axis) at FF wavelength of 9.66μm for *xxx* polarization combinations. The conversion efficiencies from the metasurface with 1st design MQW layer and nanocross array (black dots) and from the metasurface with 2nd design MQW layer and nanocross array (blue dots) are shown.

Etched T-shape nanoresonator array

Linear optical characterization was done to measure the plasmonic resonance spectrum of the metasurface. The plasmonic absorption spectra of the metasurface for *x*- and *y*-polarized input light at normal incidence are shown in Fig. 5.17 (a). For x- and y-polarized input light, a strong absorption peak near FF and SH was obtained respectively. Figure 5.17 (b) shows SHG peak power as a function of the squared FF peak power and peak intensity for *x*-polarized input (λ_{FF}=9.72μm) and *y*-polarized output (λ_{SH}=4.86μm) light. The highest SHG generation efficiency is achieved for *yxx* polarization combination, in agreement with the theoretical predictions (see section 5.3.2). 17μW of SH peak power was achieved with 75mW of input pump. As shown in the figure, the slope of the curve changes from 4.4mW/W^2 for low FF powers to 2.7mW/W^2 for high FF powers. From the experimental data, we obtain the effective nonlinear susceptibility $\chi_{xxx}^{(2)eff} \approx 483nm/V \ (407nm/V)$ for low FF intensity (high FF intensity). These effective second order nonlinear susceptibilities are nearly 5 times larger than the nonlinear susceptibility of MQW layer. Figure 5.17 (b) shows all SH power conversion efficiency data of the metasurfaces with the 1st design of MQW layer and the 2nd design of MQW layer. The etched T-shape structure shows even higher conversion efficiency than previous T-shape nanoresonator or nanocross array. The conversion efficiency from the etched T-shape nanoresonator array was improved over 100 times than that of the proof-of-concept demonstration. Although we achieved already 100 times of improvement in power conversion efficiency from the proof-of-concept experiment, the full potential of the proposed metasurface is not yet been revealed. By introducing different semiconductor heterostructures, one may be able to obtain much larger nonlinear susceptibility and if the quantum-engineered semiconductor layer is coupled to an optimized plasmonic nanoresonator array, over 1% of power conversion efficiency may be possible.

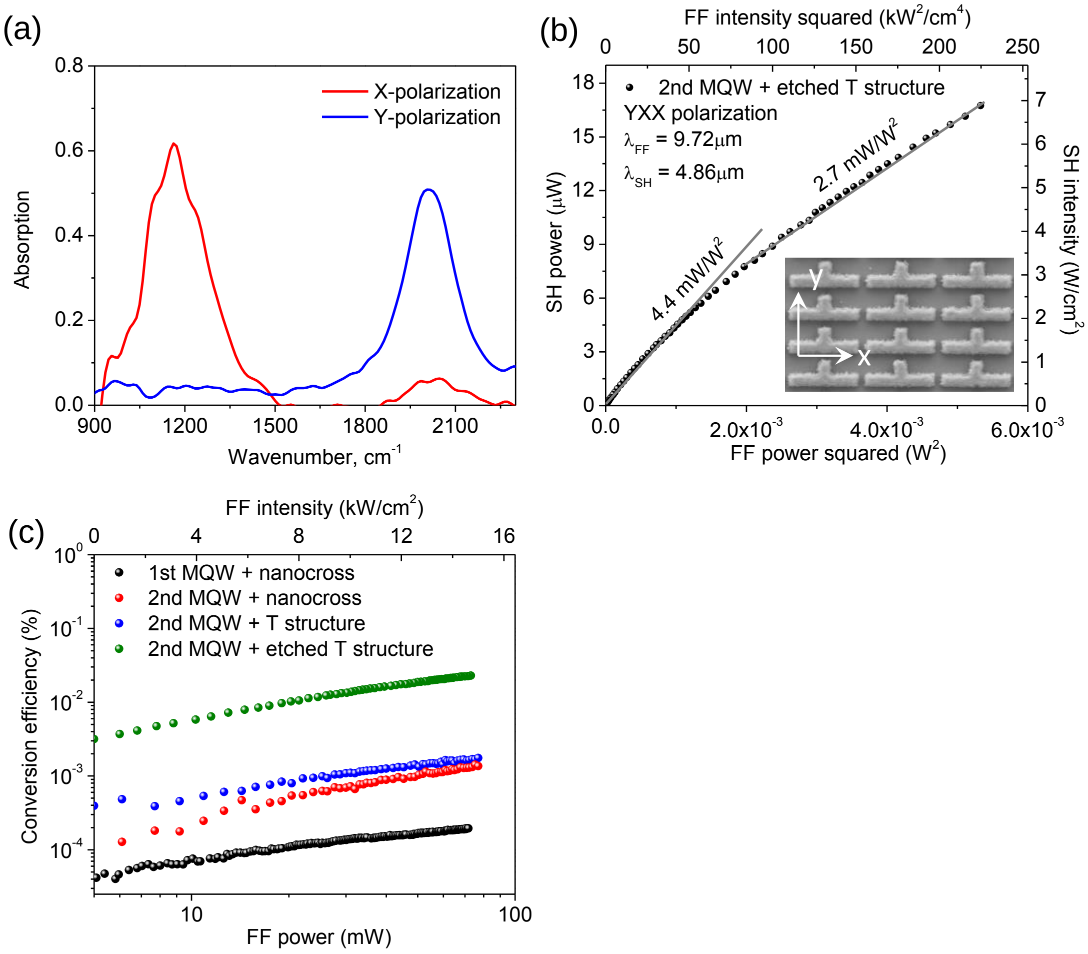

Figure 5.17: Nonlinear response from the metasurface with etched T-shape resonator array. (a) Absorption spectrum of the fabricated metasurface for normally incident light polarized along *x*- and *y*-axis. (b) Measured SH peak power output (left axis) and intensity (right axis) output as a function of FF peak power squared (bottom axis) or peak intensity squared (top axis) at FF wavelength of 9.66μm for *yxx* polarization combinations. Straight lines and labels indicate slopes of SH peak power dependence on FF power squared. (c) SHG power conversion efficiencies as a function of FF peak power (bottom axis) and peak intensity (top axis) at FF wavelength of 9.66μm for *xxx* polarization combinations. The conversion efficiencies from the metasurface with 1st design MQW layer and nanocross array (black dots) and from the metasurface with 2nd design MQW layer and nanocross array (red dots), T-shape nanoresonator array (blue dots), etched T-shape nanoresonator array (green dots) are shown.

5.4 CONCLUSION

Our experiments may be extended to create voltage-tunable [20] and active electrically pumped nonlinear metasurfaces [94-96], and to spectrally and spatially engineer the nonlinear optical response in more arbitrary ways, to name a few possibilities. The metasurfaces with giant nonlinear optical response presented here may serve as the foundation for a flat nonlinear optics paradigm, in which efficient frequency mixing may occur over deeply sub-wavelength films with significantly relaxed phase-matching conditions, compared to bulk nonlinear crystals that only require matching of wave vector components parallel to the surface. Such ultrathin nonlinear materials may dramatically simplify wave mixing experiments in a variety of setups, finding applications for frequency up- and down-conversion, mixing, phase conjugation, all-optical control and tunability, as well as photon pair generation over a surface for quantum information processing.

Chapter 6

Conclusion

6.1 SUMMARY

In this dissertation we discussed widely wavelength tunable and nonlinear plasmonic devices and metasurfaces. Widely wavelength tunable optical filters based on a planar plasmonic waveguide structure using unique properties of LR SPP have been successfully demonstrated as shown in Chapter 3. Index tunable layers for experimental demonstration were implemented by using a set of index-matching fluids and a thermo-optic polymer. As an alternative approach to produce ultrafast widely-tunable spectral response, we discussed a novel implementation of plasmonic metamaterials hybridized with quantum-electronic engineering of intersubband transitions inducing a giant electro-optic effect in Chapter 4. The hybridization of plasmonics with quantum-electronic engineering can be extended to produce nonlinear plasmonic response by designing the artificial semiconductor layer as a highly nonlinear medium. In Chapter 5, we discussed a highly nonlinear metasurfaces producing double-frequency reflection of an input beam by integrating electromagnetic engineering of plasmonic nanocircuits with quantum engineering of intersubband nonlinearities.

For future works, the plasmonic nanostructures can be designed to control electromagnetic resonances at nearly any combination of infrared and THz frequencies. The MQW structure can be designed for another $\chi^{(2)}$ or $\chi^{(3)}$ process of difference frequency generation (DFG) or optical phase conjugation (PC). This approach allows creating DFG metasurfaces generating difference frequency response of two distinct input pumps ($\omega_1 - \omega_2 \rightarrow \omega_{DFG}$) and PC metasurfaces generating optical phase conjugation for the optical reflected signal from the metasurface.

References

[1] W. L. Barnes *et al.* Surface plasmon subwavelength optics. *Nature* **424**, 824-830, (2003).

[2] D. K. Gramotnev *et al.* Plasmonics beyond the diffraction limit. *Nat. Photonics* **4**, 83-91, (2010).

[3] S. Kawata. *Near-field optics and surface plasmon polaritons.* (Springer, 2001).

[4] S. Kawata *et al.* Plasmonics for near-field nano-imaging and superlensing. *Nat. Photonics* **3**, 388-394, (2009).

[5] S. Lal *et al.* Nano-optics from sensing to waveguiding. *Nat. Photonics* **1**, 641-648, (2007).

[6] J. B. Pendry *et al.* Magnetism from conductors and enhanced nonlinear phenomena. *IEEE T. Microw. Theory.* **47**, 2075-2084, (1999).

[7] V. M. Shalaev. Optical negative-index metamaterials. *Nat. Photonics* **1**, 41-48, (2007).

[8] D. R. Smith *et al.* Metamaterials and negative refractive index. *Science* **305**, 788-792, (2004).

[9] R. A. Shelby *et al.* Experimental verification of a negative index of refraction. *Science* **292**, 77-79, (2001).

[10] S. Linden *et al.* Magnetic response of metamaterials at 100 terahertz. *Science* **306**, 1351-1353, (2004).

[11] D. Schurig *et al.* Metamaterial electromagnetic cloak at microwave frequencies. *Science* **314**, 977-980, (2006).

[12] S. A. Maier. *Plasmonics: Fundamentals and Applications.* (Springer, 2007).

[13] D. Sarid. Long-Range Surface-Plasma Waves on Very Thin Metal-Films. *Phys. Rev. Lett.* **47**, 1927-1930, (1981).

[14] R. Charbonneau *et al.* Experimental observation of plasmon-polariton waves supported by a thin metal film of finite width. *Opt. Lett.* **25**, 844-846, (2000).

[15] M. Fukui *et al.* Lifetimes of Surface-Plasmons in Thin Silver Films. *Phys. Status Solidi. B.* **91**, K61-K64, (1979).

[16] P. Berini. Long-range surface plasmon polaritons. *Adv. Opt. Photonics* **1**, 484-588, (2009).

[17] H.C. Liu *et al. Intersubband Transitions in Quantum Wells: Physics and Device Applications II.* Vol. 66 (Academic, 2000).

[18] H.C. Liu *et al. Intersubband Transitions in Quantum Wells: Physics and Device Applications I.* Vol. 62 (Academic, 2000).

[19] R. W. Boyd. *Nonlinear Optics.* 3rd edn (Academic Press, 2008).

[20] F. Capasso *et al.* Coupled-Quantum-Well Semiconductors with Giant Electric-Field Tunable Nonlinear-Optical Properties in the Infrared. *IEEE J. Quantum Elect.* **30**, 1313-1326, (1994).

[21] E. Rosencher *et al.* Second harmonic generation by intersub-band transitions in compositionally asymmetrical MQWs. *Electron. Lett.* **25**, 1063, (1989).

[22] C. Sirtori *et al.* Observation of Large 2nd-Order Susceptibility Via Intersubband Transitions at Lambda-Approximately-10-Mu-M in Asymmetric Coupled Alinas/Gainas Quantum-Wells. *Appl. Phys. Lett.* **59**, 2302-2304, (1991).

[23] S. J. B. Yoo *et al.* 2nd-Order Susceptibility in Asymmetric Quantum-Wells and Its Control by Proton-Bombardment. *Appl. Phys. Lett.* **58**, 1724-1726, (1991).

[24] K. L. Vodopyanov *et al.* Phase-matched second harmonic generation in asymmetric double quantum wells. *Appl. Phys. Lett.* **72**, 2654-2656, (1998).

[25] E. Rosencher *et al.* Giant Nonlinear Optical Rectification at 8-12 Mu-M in Asymmetric Coupled Quantum-Wells. *Appl. Phys. Lett.* **56**, 1822-1824, (1990).

[26] H. C. Liu *et al.* Sum-Frequency Generation by Intersubband Transition in Step Quantum-Wells. *IEEE J. Quantum Elect.* **31**, 1659-1662, (1995).

[27] E. Dupont *et al.* Terahertz emission in asymmetric quantum wells by frequency mixing of midinfrared waves. *IEEE J. Quantum Elect.* **42**, 1157-1174, (2006).

[28] H. C. Liu *et al.* Intersubband Raman laser. *Appl. Phys. Lett.* **78**, 3580-3582, (2001).

[29] M. Scheinert *et al.* Intersubband Raman laser from GaInAs/AlInAs double quantum wells. *Appl. Phys. Lett.* **91**, (2007).

[30] I. Grave *et al.* Observation of Phase Conjugation at 10.6 Mu-M Via Intersubband 3rd-Order Nonlinearities in a Gaas/Algaas Multi-Quantum-Well Structure. *Appl. Phys. Lett.* **60**, 2717-2719, (1992).

[31] E. Dupont *et al.* 2-Photon Intersubband Transitions in Quantum-Well Infrared Photoconductors. *Appl. Phys. Lett.* **65**, 1560-1562, (1994).

[32] D. Walrod *et al.* Observation of 3rd Order Optical Nonlinearity Due to Intersubband Transitions in Algaas/Gaas Superlattices. *Appl. Phys. Lett.* **59**, 2932-2934, (1991).

[33] J. W. Ma *et al.* Large chi((3)) determined by the degenerate four-wave mixing in a GaAs/AlGaAs step multiple quantum well. *Opt. Commun.* **124**, 457-461, (1996).

[34] A. Saar *et al.* Observation of 3rd-Order Intersubband Dc Kerr Effect at the Midinfrared Wavelengths in Gaas Quantum-Wells. *Appl. Phys. Lett.* **61**, 1263-1265, (1992).

[35] G. P. Agrawal. *Lightwave Technology: Components and Devices.* (John Wiley & Sons, 2004).

[36] O. Solgaard. *Photonic Microsystems.* (Springer, 2009).

[37] C. Ye. *Tunable External Cavity Diode Lasers.* (World Scientific Publishing, 2004).

[38] L. Bei *et al.* Acousto-optic tunable filters: fundamentals and applications as applied to chemical analysis techniques. *Prog. Quant. Electron.* **28**, 67-87, (2004).

[39] J. W. Evans. The Birefringent Filter. *J. Opt. Soc. Am.* **39**, 229-242, (1949).

[40] I. Solc. Birefringent Chain Filters. *J. Opt. Soc. Am.* **55**, 621-&, (1965).

[41] W. T. Tsang *et al.* High-Speed Direct Single-Frequency Modulation with Large Tuning Rate and Frequency Excursion in Cleaved-Coupled-Cavity Semiconductor-Lasers. *Appl. Phys. Lett.* **42**, 650-652, (1983).

[42] H. Dohi *et al.* Long-Range Surface-Plasmon Polaritons in Metal-Films Bounded by Similar-Refractive-Index Materials. *J. Phys. Soc. Jpn.* **53**, 2828-2832, (1984).

[43] A. Boltasseva *et al.* Integrated optical components utilizing long-range surface plasmon polaritons. *J. Lightwave Technol.* **23**, 413-422, (2005).

[44] F. Z. Yang *et al.* Long-Range Surface-Modes Supported by Thin-Films. *Phys. Rev. B* **44**, 5855-5872, (1991).

[45] J. J. Ju *et al.* 40 Gbit/s light signal transmission in long-range surface plasmon waveguides. *Appl. Phys. Lett.* **91**, (2007).

[46] L. Wendler *et al.* Long-Range Surface Plasmon-Polaritons in Asymmetric Layer Structures. *J. Appl. Phys.* **59**, 3289-3291, (1986).

[47] J. J. Burke *et al.* Surface-Polariton-Like Waves Guided by Thin, Lossy Metal-Films. *Phys. Rev. B* **33**, 5186-5201, (1986).

[48] P. Berini. Plasmon-polariton waves guided by thin lossy metal films of finite width: Bound modes of asymmetric structures. *Phys. Rev. B* **63**, (2001).

[49] J. Lee *et al.* Broadly wavelength tunable bandpass filters based on long-range surface plasmon polaritons. *Opt. Lett.* **36**, 3744-3746, (2011).

[50] E. D. Palik. *Handbook of Optical Constant of Solids.* (Academic Press, 1998).

[51] I. Breukelaar *et al.* Long-range surface plasmon polariton mode cutoff and radiation in slab waveguides. *J. Opt. Soc. Am. A.* **23**, 1971-1977, (2006).

[52] J. Lee *et al.* Widely tunable thermo-optic plasmonic bandpass filter. *Appl. Phys. Lett.* **103**, (2013).

[53] P. Berini *et al.* Long-range surface plasmon-polariton waveguides and devices in lithium niobate. *J. Appl. Phys.* **101**, (2007).

[54] X. L. Liu *et al.* Infrared Spatial and Frequency Selective Metamaterial with Near-Unity Absorbance. *Phys. Rev. Lett.* **104**, (2010).

[55] B. A. Munk. *Frequency Selective Surface: Theory and Design.* (Wiley, 2000).

[56] T. K. Wu. *Frequency Selective Surface and Grid Array.* (Wiley, 1995).

[57] N. F. Yu *et al.* Light propagation with phase discontinuities: generalized laws of reflection and refraction. *Science* **334**, 333-337, (2011).

[58] X. J. Ni *et al.* Broadband light bending with plasmonic nanoantennas. *Science* **335**, 427-427, (2012).

[59] A. V. Kildishev *et al.* Planar Photonics with Metasurfaces. *Science* **339**, 12320091, (2013).

[60] N. F. Yu *et al.* Flat optics with designer metasurfaces. *Nat. Mater.* **13**, 139-150, (2014).

[61] C. Pfeiffer *et al.* Metamaterial Huygens' Surfaces: Tailoring Wave Fronts with Reflectionless Sheets. *Phys. Rev. Lett.* **110**, 197401, (2013).

[62] F. Monticone *et al.* Full control of nanoscale optical transmission with a composite metascreen. *Phys. Rev. Lett.* **110**, 203903, (2013).

[63] N. I. Zheludev *et al.* From metamaterials to metadevices. *Nat. Mater.* **11**, 917-924, (2012).

[64] T. Driscoll *et al.* Memory Metamaterials. *Science* **325**, 1518-1521, (2009).

[65] Z. L. Samson *et al.* Metamaterial electro-optic switch of nanoscale thickness. *Appl. Phys. Lett.* **96**, 143105, (2010).

[66] H. T. Chen *et al.* Tuning the Resonance in High-Temperature Superconducting Terahertz Metamaterials. *Phys. Rev. Lett.* **105**, 247402, (2010).

[67] Q. Zhao *et al.* Electrically tunable negative permeability metamaterials based on nematic liquid crystals. *Appl. Phys. Lett.* **90**, 011112, (2007).

[68] O. Buchnev *et al.* Electro-optical control in a plasmonic metamaterial hybridised with a liquid-crystal cell. *Opt. Express* **21**, 1633-1638, (2013).

[69] H. T. Chen *et al.* Active terahertz metamaterial devices. *Nature* **444**, 597-600, (2006).

[70] W. L. Chan *et al.* A spatial light modulator for terahertz beams. *Appl. Phys. Lett.* **94**, 213511, (2009).

[71] L. Ju *et al.* Graphene plasmonics for tunable terahertz metamaterials. *Nat. Nanotechnol.* **6**, 630-634, (2011).

[72] S. H. Lee *et al.* Switching terahertz waves with gate-controlled active graphene metamaterials. *Nat. Mater.* **11**, 936-941, (2012).

[73] Z. Y. Fang *et al.* Gated Tunability and Hybridization of Localized Plasmons in Nanostructured Graphene. *Acs Nano* **7**, 2388-2395, (2013).

[74] Y. Yao *et al.* Broad Electrical Tuning of Graphene-Loaded Plasmonic Antennas. *Nano Lett.* **13**, 1257-1264, (2013).

[75] Y. Yao *et al.* Wide Wavelength Tuning of Optical Antennas on Graphene with Nanosecond Response Time. *Nano Lett.* **14**, 214-219, (2014).

[76] M. A. Belkin. in Proceedings of the Tri-Service Metamaterials Program Review, Virginia, U.S.A., May 22-25, (2012).

[77] J. Lee *et al.* in Proceedings of the 7th International Congress on Advanced Electromagnetic Materials in Microwaves and Optics - Metamaterials, Bordeaux, France, September 16-21, (2013).

[78] A. Gabbay *et al.* Theory and modeling of electrically tunable metamaterial devices using inter-subband transitions in semiconductor quantum wells. *Opt. Express* **20**, 6584-6597, (2012).

[79] I. Brener. in Proceedings of the 7th International Congress on Advanced Electromagnetic Materials in Microwaves and Optics - Metamaterials 2013, Bordeaux, France, September 16-21, (2013).

[80] A. Benz *et al.* Tunable metamaterials based on voltage controlled strong coupling. *Appl. Phys. Lett.* **103**, 263116, (2013).

[81] D. Dini *et al.* Microcavity polariton splitting of intersubband transitions. *Phys. Rev. Lett.* **90**, 116401, (2003).

[82] Y. Todorov *et al.* Strong Light-Matter Coupling in Subwavelength Metal-Dielectric Microcavities at Terahertz Frequencies. *Phys. Rev. Lett.* **102**, 186402, (2009).

[83] Y. Todorov *et al.* Ultrastrong Light-Matter Coupling Regime with Polariton Dots. *Phys. Rev. Lett.* **105**, 196402, (2010).

[84] P. Jouy *et al.* Transition from strong to ultrastrong coupling regime in mid-infrared metal-dielectric-metal cavities. *Appl. Phys. Lett.* **98**, 231114, (2011).

[85] A. Harwit *et al.* Observation of Stark Shifts in Quantum-Well Intersubband Transitions. *Appl. Phys. Lett.* **50**, 685-687, (1987).

[86] D. A. Holm *et al.* Infrared Phase Modulators with Multiple Quantum Wells. *IEEE J. Quantum Elect.* **25**, 2266-2271, (1989).

[87] Y. J. Mii *et al.* Large Stark Shifts of the Local to Global State Intersubband Transitions in Step Quantum-Wells. *Appl. Phys. Lett.* **56**, 1986-1988, (1990).

[88] A. Melikyan *et al.* High-speed plasmonic phase modulators. *Nat. Photonics* **8**, 229-233, (2014).

[89] H. C. Liu *et al.* *Intersubband Transitions in Quantum Wells: Physics and Device Applications II.* (Academic Press, 2000).

[90] J. Lee *et al.* Ultrafast Electrically Tunable Polaritonic Metasurfaces. *Adv. Opt. Matt.*, DOI:10.1002/adom.201400185, (2014).

[91] S. Adachi. *Handbook on Physical Properties of Semiconductors: III-V Compound Semiconductors.* Vol. 2 (Springer, 2004).

[92] N. K. Emani *et al.* Electrical Modulation of Fano Resonance in Plasmonic Nanostructures Using Graphene. *Nano Lett.* **14**, 78-82, (2014).

[93] M. M. Fejer *et al.* Observation of extremely large quadratic susceptibility at 9.6-10.8 μm in electric-field-biased AlGaAs quantum wells. *Phys. Rev. Lett.* **62**, 1041-1044, (1989).

[94] C. Gmachl *et al.* Optimized second-harmonic generation in quantum cascade lasers. *IEEE J. Quantum Elect.* **39**, 1345-1355, (2003).

[95] M. A. Belkin *et al.* Terahertz quantum-cascade-laser source based on intracavity difference-frequency generation. *Nat. Photonics* **1**, 288-292, (2007).

[96] K. Vijayraghavan *et al.* Broadly tunable terahertz generation in mid-infrared quantum cascade lasers. *Nat. Commun.* **4**, 2021, (2013).

[97] E. Rosencher *et al.* Second harmonic generation by intersubband transitions in compositionally asymmetrical MQWs. *Electron. Lett.* **25**, 1063-1065, (1989).

[98] E. Rosencher *et al.* Quantum engineering of optical nonlinearities. *Science* **271**, 168-173, (1996).

[99] X. L. Liu *et al.* Taming the blackbody with infrared metamaterials as selective thermal emitters. *Phys. Rev. Lett.* **107**, 045901, (2011).

[100] M. W. Klein *et al.* Second-harmonic generation from magnetic metamaterials. *Science* **313**, 502-504, (2006).

[101] N. Feth *et al.* Second-harmonic generation from complementary split-ring resonators. *Opt. Lett.* **33**, 1975-1977, (2008).

[102] W. J. Fan *et al.* Second harmonic generation from patterned GaAs inside a subwavelength metallic hole array. *Opt. Express* **14**, 9570-9575, (2006).

[103] F. B. P. Niesler *et al.* Second-harmonic generation from split-ring resonators on a GaAs substrate. *Opt. Lett.* **34**, 1997-1999, (2009).

[104] J. B. Pendry. Negative refraction makes a perfect lens. *Phys. Rev. Lett.* **85**, 3966-3969, (2000).

[105] N. Fang *et al.* Sub-diffraction-limited optical imaging with a silver superlens. *Science* **308**, 534-537, (2005).

[106] U. Leonhardt. Optical conformal mapping. *Science* **312**, 1777-1780, (2006).

[107] J. B. Pendry *et al.* Controlling electromagnetic fields. *Science* **312**, 1780-1782, (2006).

[108] P. Y. Chen *et al.* Invisibility and cloaking based on scattering cancellation. *Adv. Mater.* **24**, Op281-Op304, (2012).

[109] J. B. Pendry. Time reversal and negative refraction. *Science* **322**, 71-73, (2008).

[110] A. Rose *et al.* Overcoming phase mismatch in nonlinear metamaterials. *Opt. Mater. Express* **1**, 1232-1243, (2011).

[111] C. Argyropoulos *et al.* Nonlinear plasmonic cloaks to realize giant all-optical scattering switching. *Phys. Rev. Lett.* **108**, 263905, (2012).

[112] A. Hugi *et al.* Mid-infrared frequency comb based on a quantum cascade laser. *Nature* **492**, 229-233, (2012).

[113] I. Vurgaftman *et al.* Optimized second-harmonic generation in asymmetric double quantum wells. *IEEE J. Quantum Elect.* **32**, 1334-1346, (1996).

[114] A. Benz *et al.* Strong coupling in the sub-wavelength limit using metamaterial nanocavities. *Nat. Commun.* **4**, 2882, (2013).

[115] T. Ellenbogen *et al.* Chromatic plasmonic polarizers for active visible color filtering and polarimetry. *Nano Lett.* **12**, 1026-1031, (2012).

[116] Y. Zhao *et al.* Tailoring the dispersion of plasmonic nanorods to realize broadband optical meta-waveplates. *Nano Lett.* **13**, 1086-1091, (2013).

[117] J. Lee *et al.* Giant nonlinear response from plasmonic metasurfaces coupled to intersubband transitions. *Nature* **511**, 65-U389, (2014).

[118] C. A. Balanis. *Advanced Engineering Electromagnetics.* (Wiley, 1989).

[119] K. L. Vodopyanov *et al.* Intersubband absorption saturation study of narrow III-V multiple quantum wells in the λ=2.8-9 μm spectral range. *Semicond. Sci. Tech.* **12**, 708-714, (1997).